Design strategies and technology of Elettra 2.0 for a versatile offer to the user community

E. Karantzoulis [a], S. Di Mitri [a,b,*], F. Barbo [a], W. Barletta [c], S. Bassanese [a], R. Bracco [a], G. Brajnik [a], A. Buonanno [a], D. Caiazza [a], A. Carniel [a], D. Castronovo [a], M. Cautero [a], S. Cleva [a], M. Comisso [d], I. Cudin [a], S. Dastan [a], R. De Monte [a], B. Diviacco [a], A. Fabris [a], R. Fabris [a], G. Gaio [a], S. Grulja [a], L. Gregoratti [a], A. Gubertini [a], S. Krecic [a], S. Lizzit [a], G. Loda [a], M. Lonza [a], K. Manukyan [a], B. Mazzucco [a], M. Milani [a], D. Millo [a], M. Modica [a], L. Novinec [a], G. Pangon [a], C. Pasotti [a], A. Passarelli [e], L. Rumiz [a], S. Sbarra [a], G. Scrimali [a], N. Shafqat [a], G. Simonetti [a], M. Svandrlik [a], F. Tripaldi [a], M. Veronese [a], R. Visintini [a], E. Yousefi [a], M. Zaccaria [a]

[a] Elettra – Sincrotrone Trieste S.C.p.A., I - 34149, Basovizza, Trieste, Italy
[b] University of Trieste, Department of Physics, I - 34100, Trieste, Italy
[c] Department of Physics, Massachusetts Institute of Technology, Cambridge, MA, United States
[d] University of Trieste, Department of Engineering and Architecture, I - 34100, Trieste, Italy
[e] INFN - Sezione di Napoli, Napoli, Italy

ABSTRACT

Elettra 2.0 will be a fourth generation storage ring light source replacing the existing Elettra synchrotron. This article illustrates design strategies, physical investigations and technical choices to meet multiple and sometimes conflicting requirements. These include to make Elettra 2.0 a fully transversely coherent source up to 0.5 keV-photon energy, diversify the type of experiments through a very broad range of photon energies, from infrared to hard x-rays, maximize the number of photon beamlines in excess of 2-times the machine periodicity, and be able to produce picosecond-long light pulses at MHz repetition rate without interference to the standard multi-bunch operation. Most recent advancements in beam physics, technical systems and installation plan are reported with some detail.

1. Introduction

Located on the outskirts of Trieste, Italy, Elettra has been operated for users since 1994, being the first third-generation light source for soft x-rays in Europe. During those 30 years, many improvements were made to keep the machine updated and therefore competitive with other more recent light sources. Following the initial successful operation of the full energy injector in 2008, after 14 years of energy ramping, Elettra established top-up operation in spring 2010 [1,2], although the ring was not originally designed for it.

The Elettra 2.0 project [3–6] was approved by the Italian Government in 2017. According to the current schedule, the new machine will start serving users in 2027. The design phase has met several and sometimes conflicting requirements, such as.

- make Elettra 2.0 a fully transversely coherent source up to 0.5 keV-photon energy;

- double the total average current at the maximum energy of 2.4 GeV, to further increase beam brilliance and coherent flux;
- diversify the type of experiments by providing a very broad range of photon energies, from few tens of eV to several tens of keV;
- maximize the number of photon beamlines, in excess of 2-times the machine periodicity;
- produce picosecond-long light pulses at MHz repetition rates, at several beamlines simultaneously, without interfering with standard multi-bunch operation;
- minimize the transition time and ensure smooth commissioning phase and a robust operation of the light source.

To achieve those goals, several systems of the accelerator complex will be either upgraded or replaced, such as the injection scheme, the high-performance magnetic lattice, ultra-vacuum mechanical components, and insertion devices. The installation of the RF transverse deflecting cavities for the production of picosecond-long light pulses has

implied detailed modelling of transient beam loading in the presence of 4 different frequencies of radiofrequency (RF) cavities (main RF at 500 MHz plus a super-conducting 3rd harmonic cavity for bunch lengthening and Landau damping, and 6 and 6.5 RF harmonics for production of short pulses). The upgrade also addresses the request from the established user community to minimize the duration of beam-time interruption, imposing the need of a careful organization and planning of all the phases of the project, from the removal of the old machine to the installation and successful commissioning of the new one.

This article offers an overview of the Elettra 2.0 project, but it mainly aims at presenting advances on the most important systems of the accelerator that cannot be found in the already published conceptual [3] and technical design report [6]. Some emphasis is put on those original solutions which constitute in-house developments and studies carried out to face the challenges posed by the aforementioned ambitious goals.

The article is organized as follows. Section 2 recalls the scientific motivations leading to Elettra 2.0. Section 3 illustrates the design strategies of the magnetic lattice. Doing so, it highlights the unique features of the light source. Technical solutions for the definition of magnets, insertion devices, power converters, vacuum components and RF systems are reported in Sections 4–10. Section 11 and 12 describe the development and use of semi-analytical and numerical models to predict the multi-bunch longitudinal and transverse dynamics, including impedance calculations, codes and benchmarking measurements. The concept of short pulse production and a summary of the expected performance is recalled in Section 13. Section 14 illustrates the upgrade of the injection chain required by the reduced dynamic aperture of Elettra 2.0 and by the short pulse scheme. The installation plan and considerations on the logistics are given in Section 15. Conclusions are reached in Section 16.

2. Motivations

Elettra delivers synchrotron light from infrared to hard X-rays to 28 photon beamlines. Ten are served by bending magnets. Two beamlines use light from a 3.5 T-superconducting wiggler. Planar and elliptically polarizing out-of-vacuum undulators, including canted insertion devices (IDs) of the APPLE-II type, occupy all the eleven available long straights (one is left for injection). Recently, two adjustable phase undulators have been installed in one short dispersive section.

The present facility consists of a 100 MeV linac, a 2.5 GeV booster synchrotron, and a 2.0/2.4 GeV storage ring with horizontal geometric emittance of 7/10 nm-rad. Elettra is the only facility operating at two energies, both in top-up mode. The circumference is long 259.2 m and acceleration by the main RF is exploited by means of 4 single-cell room-temperature RF cavities at 499.654 MHz MHz. The harmonic number is therefore 432. A passive superconducting third harmonic cavity (3HC), hosted in a long straight section and close to a superconducting wiggler, lenghtens the bunch by a factor of three, for improved stability and increased lifetime [7]. The main operating modes are multi-bunch with a dark gap of 42 ns and hybrid, i.e., multi-bunch with one (for time resolved experiments) or two single bunches (40 ns apart in a dark gap of 120 ns for pump-probe experiments). The operating intensities are 310 mA at 2 GeV and 160 mA at 2.4 GeV, with 3–5 mA single bunch in hybrid mode.

The Elettra user facility attracts more than 1000 experimental proposals per year from more than 50 countries. As does any other 3rd generation storage ring light source, it results complementary to free-electron lasers (FELs) and high harmonic generation sources [8] as for repetition rate, pulse intensity, spectral tuning of the emitted radiation and polarization control. Not to mention the ability to serve an order of magnitude more beamlines simultaneously with respect to single-pass machines, higher intrinsic pulse-to-pulse stability in intensity, wavelength and bandwidth. The high average flux distributed over many electron bunches is highly beneficial for photon- and coherence-hungry techniques, allowing a better handling of undesired effects in

experiments due to a high ionization rate, for example, space-charge problems in electron detection and radiation-induced sample damage [9].

The advances in accelerator technology on the one side and the development of more and more sophisticated experimental techniques – such as in diffraction imaging – on the other side, has recently led to the emergence of 4th generation of storage ring light sources. Transverse coherence in the wavelength range ~0.5–2 nm (~0.6–2.5 keV) is promised in both transverse planes at storage rings upgraded with multi-bend lattices [10,11]; for this reason, they are called diffraction-limited storage rings (DLSRs). To keep Trieste's light source competitive for synchrotron radiation research and to enable new science, a DLSR Elettra 2.0 will replace Elettra. To keep Trieste's light source competitive for synchrotron radiation research and to enable new science, a DLSR Elettra 2.0 will replace Elettra. The addition of 3 new micro-spot beamlines to profit from the larger coherent flux of the new source, and over-subscription factors of scientific proposals at Elettra systematically larger than 3–6, both led to the decision of an Elettra 2.0 design aimed to maximize the number of radiation source points. A symmetric enhanced six-bend achromat lattice (S6BA-E i.e a six-bend combined with anti-bends) was designed to also allow the installation of short IDs in up to 12 low-dispersion (<60 mm) straight sections in the middle of the arcs, in addition to the 12 dispersion-free long straight sections inherited by the Elettra lattice. Sources of radiation will be added or upgraded, including 3 undulators and 2 short wigglers in 5 short straight sections, 3 superconducting dipole magnets ("super-bends") replacing 3 room-temperature dipoles, and 3 in-vacuum undulators. The number of total experimental stations is augmented from the present 28 to 32.

Newly defined scientific needs in the tender X-ray range drove the decision of the nominal operating energy to 2.4 GeV. The possibility of operating for a limited percentage of user time also at 2 GeV is left open, to allow some beamlines to gradually upgrade to the expanded scientific case [3].

The project concept comes with the constraints of keeping the same machine circumference, the same source point position in the long straights relative to the previous machine, the present linac and booster ring for injection, and limiting the dark time for installation and commissioning to 18 months.

A symmetric six-bend achromat was produced by using longitudinal and transverse gradient-dipoles, and quadrupole magnets off-set with respect to the reference orbit to act as "reverse bends" [12]. Consequently, the electron optics is not purely of the multi-bend type, but also uses dispersion minimizers to further reduce the horizontal emittance by a total factor of 47 compared to the present machine, at the energy of 2.4 GeV. Reduction of emittance, flat-beam configuration (transverse emittance ratio <5 %) and refurbishment of the entire vacuum system compatible with up to 400 mA total average current, will produce up to three orders of magnitude brilliance increase and 60-fold higher coherence at 1 keV. These increases will have a strong impact on pushing the transverse resolution down to the few nanometer scale, since in all experiments the use of focusing optics translates directly into an increase in focused flux density. This improvement opens, in turn, the possibility of performing all types of spectroscopies with nano-sized photon beams (e.g., nano-PES, nano-ARPES) approaching the X-ray imaging spatial resolution of a few nm. Complemented with nano-scale IR and VUV microscopy, the large coherent fraction of the light pulse will allow unprecedented investigations of structure and dynamics in three and four dimensions with variable probing depths. The large degree of transverse coherence of the source will open unique opportunities for coherence-hungry methods. Coherent diffraction imaging with chemical specificity, such as scanning mode ptychography and closely related X-ray photon correlation spectroscopy (XPCS), will approach the wavelength-limited spatial resolution with chemical specificity and improved temporal resolution.

Increasing brightness and coherence will also have a direct impact on the achievable temporal resolution for exploiting processes in real time

of material fabrication and functioning. All spectroscopic, 'classical' diffraction and scattering methods will gain from the high brightness as well. In the case of e.g. XPCS, the major gain will derive from the increased coherence, since the time resolution – proportional to the square of the coherent flux – will be limited only by the electron bunch length of ~50 ps FWHM at 400 mA average current.

Chemical, biological and physical processes are dynamic; therefore, researchers must monitor their activity at multiple time scales. Picosecond dynamics is of paramount importance in biological, organic and inorganic processes and condensed matter systems. They provide a compelling argument to develop synchrotron sources complementary to FELs, producing (sub-)picosecond electron bunches that will have advantages such as wide and continuous tuneability, polarization control, MHz repetition rate and higher photon flux compared to laser slicing [13,14]. In fact, a second phase of Elettra 2.0 will open the possibility of producing X-ray pulses as short as ~1 ps FWHM at most of the beamlines, for time resolved experiments using RF vertically deflecting (crab) cavities [15]. These are planned to be installed in one long straight section of the ring, shared with a 2.3 m-long ID.

The strong points and state-of-the-art level of the Elettra 2.0 design in the panorama of coming soon-DLSR, are highlighted in Table 1. Since the equilibrium horizontal emittance in an electron synchrotron scales like $\varepsilon_x \propto \gamma^2/R$, with γ the Lorentz factor for the beam enegry and R the curvature radius, the table reports the geometric factor $Q = \varepsilon_x C / (\gamma^2 F_{BL})$, with C the accelerator circumference and F_{BL} the ratio of the number of source points from undulators or wigglers, and the machine periodicity (number of identical cells or sectors). Compactness, small emittance and large fan-out of beamlines, all require Q to be as small as possible. Elettra 2.0 is compared to two other approved state-of-the-art projects in the same electron energy range, and to another at very high energy, as example. In summary, Elettra 2.0 will provide substantial coherent flux in the soft X-rays *and* maximize the number of IDs per meter.

3. Accelerator overview

A list of parameters of the Elettra 2.0 storage ring is in Table 2. The "enhanced, symmetric six-bend achromat" (S6BA-E) lattice has a total length of 259.2 m, equal to that of the present Elettra. Worth to notice, the lattice was defined such that the transverse position of the Elettra 2.0 source points in the long straight sections (symmetry point in the middle of the section) coincide with those of Elettra.

The lattice is made of 24 symmetric arcs grouped in 12 center-symmetric achromatic cells, 12 long straights and 12 short dispersive straights sections (12-fold symmetry). A 3-D rendering of the arc is shown in Fig. 1. Each arc consists of 3-unit cells of the "theoretical minimum emittance" type, i.e. .

- 3 dipoles, one (0.8 T field) with vertical field gradient, and two (1.0 T and 1.46 T) with combined transverse (<22 T/m) and longitudinal gradient;
- 7 quadrupoles (<50 T/m), four of which are horizontally shifted by 5.16 mm to give the required reverse-bend angle of −0.4 deg each;
- 10 sextupoles (<4500 T/m²), 6 with embedded correctors' coils, 2 with additional general purpose coils, e.g., for beam-based alignment (BBA), and 2 with skew quadrupole coils;

Table 1
Figures of merit of DLSRs (see text).

	ELETTRA 2.0	SLS 2.0	ALS-U	APS-U
ε_x [pm rad]	220	158	108	42
E [GeV]	2.4	2.7	2	6
C [m]	259	288	197	1104
F_{BL}	17/12	11/12	14/12	32/40
Q [10^{-15} m²]	1.8	1.8	1.2	0.4

Table 2
Main parameters of Elettra 2.0 storage ring.

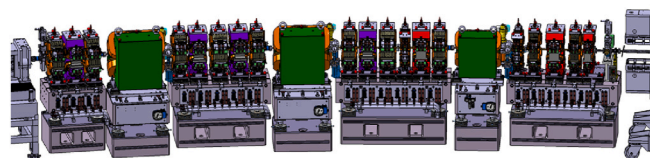| Parameter	Value	Units
Energy	2.4	GeV
Circumference	259.2	m
Harmonic number	432	
Average current	400	mA
Horizontal emittance (bare)	212	pm rad
Coupling factor	3	%
Energy loss/turn	<670	keV
RF peak voltage	2	MV
Main radiofrequency	499.654	MHz
Bunch duration, RMS	15–20	ps
Rel. energy spread, RMS	0.09	%

Fig. 1. Elettra 2.0 arc view from inner side.

- 1 octupole combined with corrector coils;
- 1 octupole combined with quadrupole coils;
- 1 pure corrector (both planes).

The total number of dipole and multipole magnets is 552 [16]. Dipole and quadrupole magnets are specially designed so that the coils do not protrude. This design allows the installation of a dense, tight magnetic lattice (the inter-magnet distance varies between 50 and 130 mm) as required by the strong focusing typical in DLSRs. The orbit correction scheme is implemented through 168 correction coils per plane and 24 pure correctors, totaling to 192 elements and 168 Beam Position Montiors. For the fast orbit feedback, 72 additional small correctors (6 per achromat) will be used. All magnets will be powered independently (primarily to guarantee maximum flexibility in controlling the linear and nonlinear optics), most are water-cooled, and they will be measured on site [17]. Each arc will have 8 girders consisting of granite slabs of lengths from 1.2 to 1.5 m, 0.6 m wide and 0.3 m thick. A mock up of a multipole section has been constructed and the eigen-frequencies analysed both experimentally and using simulations, finding the frequency of 44 Hz as being the closest to 50 Hz, the European AC power frequency [18].

The vacuum chamber will be rhomboidal with 17 mm × 27 mm internal dimensions, mainly made of copper, with some parts in aluminum (long straights) and stainless steel (dipole chambers and short straights). Most parts of the chamber will be covered with 500 nm-thick NEG [19].

The four 500 MHz, single-cell RF cavities presently in operation in Elettra will be re-used in the first phase of Elettra 2.0 [20]. Each cavity will be installed in a short straight section, each powered by a 130 kW solid state amplifier (SSA) and controlled through by a low-level RF digital system. A plan for future replacement of the cavities with more advanced ones equipped with Higher Order Mode (HOM) dumpers is under evaluation.

The nominal betatron tunes are $\nu_x = 32.24$, $\nu_y = 9.15$, and the natural normalized chromaticity (−71, −68) is corrected to +2 in both planes. The two arcs of the achromatic cell are separated in the middle by a short straight section of 1.26 m free space. This space is available for installing RF cavities, diagnostics, short undulators or wigglers. The useful free space of the long straights connecting the cells is approximately 5 m long; that is sufficient for installing IDs and, in some free space, feedback kickers and other instrumentation. Fig. 2 shows the linear optics functions along one achromatic cell.
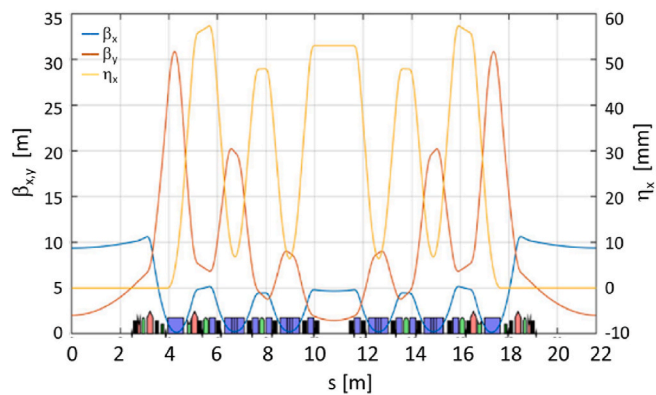
Fig. 2. Elettra 2.0 S6BA-E achromatic cell lattice and linear optics functions.

The equilibrium horizontal emittance of the bare lattice at the zero-current limit is 212 p.m.-rad (149 p.m.-rad at 2 GeV). That value is about a factor of 50 reduction from the present machine, at the same energy. It will increase the brilliance up to 2-3 orders of magnitude in the photon energy range 1–10 keV (e.g., about 36 times or $\sim 1.5 \times 10^{21}$ in standard units at 1 keV, approximately 300 times or $\sim 2.5 \times 10^{21}$ in standard units at 10 keV). The coherence fraction of the light pulse will be increased by a factor of 60 at 1 keV (~ 30 % of the total flux) and 400 at 10 keV (~ 4 % of the total flux).

The passive superconducting third harmonic cavity (3HC) lengthens the bunch for stability and lifetime [7], but also makes the inverse-rate of emittance growth from intrabeam scattering much longer than the transverse damping time. A 2.5-fold bunch lengthening will increase the Touschek lifetime by approximately the same factor, i.e. up to 15 h, while keeping the horizontal emittance equal to 235 p.m.-rad for 1 mA single-bunch current and 1 % coupling (11 % increase due to intrabeam scattering, 30 % emittance growth without 3HC).

Hence, unlike few other DLSRs, no specific need from emittance and lifetime control emerges for operation at full coupling (equal transverse eigen-emittances and comparable beam sizes at IDs). Moreover, most of the existing beamline optics, which will be reused in the first phase of operation of Elettra 2.0, better matched to a flat-beam configuration, and will take advantage of a 4-D spectral brightness and coherent flux almost doubled w.r.t. emission from a round beam.

The dynamic aperture including machine errors (alignment, field quality) and physical restrictions from the vacuum chamber and IDs is about ± 6 mm horizontally and ± 2 mm vertically at the injection point, as shown in Fig. 3; it therefore permits horizontal off-axis injection. Simulations have shown that efficient orbit correction is achieved with less than 1 mrad kick from the correction coils during the commissioning phase. The effects of IDs on the beam dynamics has been studied using kick maps [21]. The analysis shows that the dynamic aperture can be
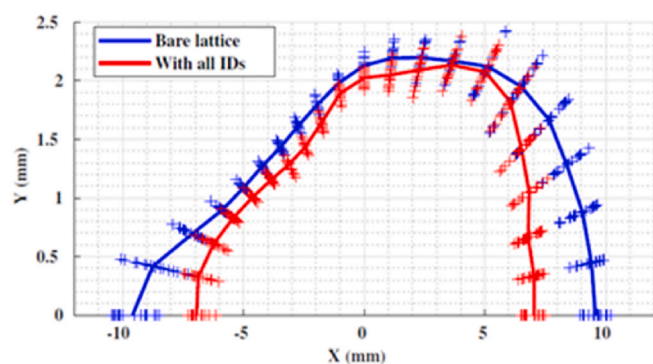
recovered by means of a small adjustment of the horizontal tune.

A semi-analytical estimate of the broadband impedance of Elettra 2.0 yields results comparable to that of the present machine, namely, about 0.85 Ω longitudinal (about 0.24 Ω effective) and 564 kΩ/m transverse impedance. These values give a betatron tune shift of about -0.8 kHz/mA, vs. -0.6 kHz/mA at Elettra. The total longitudinal loss factor is 20.2 V/pC, corresponding to a parasitic power loss of ~ 7 kW with 400 mA total current, when the effect of 3HC is included.

The single bunch microwave instability threshold was predicted using the *mbtrack2* code [22] to be approximately 3.5 mA [23]. This result, shown in Fig. 4, is in correspondence of the change of slope of the relative energy spread with bunch current. The multi-bunch effect of the resisitive wall impedance on the transverse dynamics has also been studied [24]; it predicts thresholds of about 1 mA that are easily handled by the multibuch feebback system. The Transverse Mode Coupling Instability (TMCI) threshold was analytically estimated to be 5.5 mA.

The average Touschek lifetime including machine errors was calculated through particle tracking in elegant [25]. Its is 5 h with 1 mA/bunch, 2 MV total RF voltage and 3 % coupling but no 3HC in action. It becomes 12 h assuming 2.5-fold bunch lenghtening by 3HC. For the study of transient beam loading effects, a code was developed [26] and calibrated with experimental sessions at Elettra. The results confirm that a bunch lengthening factor in the range 2.5–3 along the bunch train can be obtained at 400 mA.

The nominal fill pattern foresees a single dark gap of 64 ns. This guarantees: i) a maximum bunch average current of 1 mA for RF buckets regularly filled every 2 ns, and 2 mA per bunch of alternated filled buckets in configuration of short pulse production (see more later), ii) an acceptable maximum ± 15 deg at 500 MHz synchronous phase shift along the bunch train, iii) suppression of ion trapping instability, in the assumption of similar or improved vacuum pressure w.r.t. Elettra, and similar residual gas components.

The electron-gas scattering lifetime was simulated with th educated guess that the relative proportions of residual gas will be similar to those measured in the Elettra vacuum chamber: the two largest contributions are 85 % of H_2 and 7 % of CO. Based on this assumption, the predicted lifetime for elastic and inelastic scattering is dominated by interactions with CO molecules, resulting in 20 (60) hours for 3 (1) nTorr of CO dynamic pressure. When this value is summed with the Toushek lifetime in the presence of 3HC, the resulting total beam lifetime is approximately 8 h.

The same injection chain of Elettra will be used for Elettra 2.0, but with substantial upgrades. The present chain consists of a 100 MeV-linac, a 2.5 GeV-booster synchrotron, and a booster-to-storage ring transfer line. Due to the relatively large transverse sizes of the beam extracted from the booster (~ 150 nm rad geometric horizontal emittance at 2.4 GeV), a pulsed multipole cannot be employed. The same off-axis injection scheme already in use for Elettra will be implemented instead, but with two modifications [27,28]. First, a 1 mm-thin septum
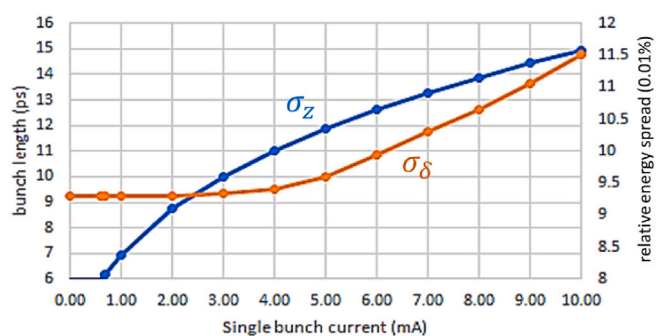

Fig. 3. Dynamic aperture at the injection point for the bare lattice, with machine errors and orbit correction, with (red) and without IDs (blue).

Fig. 4. *mbtrack2* simulation results of bunch length (blue) and relative energy spread (orange) versus single bunch average current in Elettra 2.0, in the presence of broadband impedance but no 3HC in action.

will follow other two septa magnets to allow a separation of 4 mm in the horizontal plane between the stored and the injected beam. Second, a swap of horizontal and vertical emittance of the injected beam will be implemented at the moment of extraction from the booster, by crossing the 2nd order difference resonance during the very last turns of the energy ramp. Doing so, the horizontal beam size at the injection point will be reduced by approximately 50 % or more w.r.t. the present injection, thus ensuring an injection efficiency higher than 95 % in Elettra 2.0 according to simulations.

Elettra evolved during 30 years to 28 beamlines; 19 beamlines are nowadays served from a large variety of IDs including planar and APPLE-II type (variable gap and fixed gap-variable phase), implementing room-temperature electromagnetic and superconducting technology. To satisfy the new science case, 3 in-vacuum undulators (IVU) of 5 mm full gap will be installed in Elettra 2.0. The brilliance at the source of such devices is $\sim 10^{21}$ ph/s/mm^2/mrad^2/0.1%BW at 10 keV, as shown by Fig. 5. Still, some of the existing IDs, including the superconducting wiggler operated at reduced field (2.5 T), will be re-used. Moreover, 2 short wigglers (3 periods) and 3 out-of-vacuum undulators will be installed in the dispersive short straight sections [29].

Elettra 2.0 will serve in total 32 beamlines, many of them being an upgrade of existing ones. The beamline upgrade plan foresees that.

- 9 beamlines will keep their present position,
- 6 beamlines will be moved but will stay in the same sector,
- 4 beamlines will be moved to a different sector,
- 7 beamlines will be removed,
- 12 beamlines will be new. Among these, one will be devoted to coherent diffraction imaging, three will provide a micro-spot at the sample, which the present machine cannot support because of poor coherence in the horizontal plane.

A relatively high photon flux of 10^{13} ph/s is required at several tens of keV by the hard X-ray imaging beamlines Life and Material Science (50 keV) and by the X-ray absorption beamline (35 keV). This flux will be guaranteed by synchrotron radiation emission from three super-bends of 6 T-magnetic field [30]. When all IDs and super-bends are in use, and assuming all of them are operating with minimum gap, the emittance at 2.4 GeV reads 219 p.m. rad; the single particle energy loss per turn due to radiation amounts to approximately 620 keV. This value translates into a 248 kW average power loss, well within the main RF capabilities.
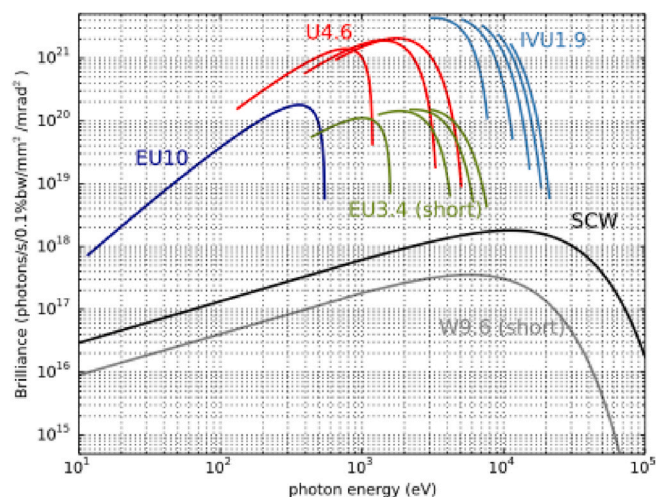

Fig. 5. Peak brilliance of selected IDs in Elettra 2.0. The electron beam energy is 2.4 GeV.

4. Dipole and multipole magnets

Table 3 lists the dipole and multi-pole magnets of Elettra 2.0. The dipole magnets will be independently supplied. The challenge related to the very short drift space between the magnets has been solved by employing a novel kind of longitudinally extended pole tip on quadrupoles and dipoles. They shall be made of solid iron, without letting the coils protrude. Instead, sextupole and octupole yokes will be made of laminated iron to minimize the effect of eddy currents induced by the operation of the embedded correctors (coils), see also Table 4.

4.1. Dipoles

Each arc of Elettra 2.0 includes one dipole B64 (closer to the long straight section) and two dipoles B80, see Fig. 6. The dipole B80 is made of three sectors to implement an effective step-wise longitudinal field gradient. The central sector has a pure dipolar vertical field. The other two (BQ) show in addition a transverse quadrupole gradient of 21 T/m, obtained through a suitable shaping of the profile of the magnetic pole. Since the realisation of the longitudinally extended pole tips implies the use of one coil only for the three sectors, the aperture radius R of the hyperbolic profile of the BQ sectors results related to the quadrupole strength and to beam rigidity according to Eq. (1), where α_1, L_m and d are, respectively, angle, magnetic length and gap of the central pole, k is the strength of the sector BQ, and η is the efficiency due to iron non-linearity and field dispersion:

$$R = \sqrt{\frac{\alpha_1 * d}{\eta * L_m * k}} \tag{1}$$

To tune the BQ quadrupole strength without modifying the reference orbit for on-energy particles, the central sector is provided with additional trim coils. Dipole B64 has a single BQ sector the vertical aperture of which was determined according to the minimum requirement set by the vacuum chamber.

Table 4 lists the main parameters of the Elettra 2.0 dipole magnets. Fig. 7 shows the longitudinal field distribution for different values of the main current.

4.2. Quadrupoles

Quadrupole magnets of Elettra 2.0 are grouped into three families, Q13, Q24, and Q24$_{RB}$. They are all water-cooled. They have their magnetic yoke split into two parts by non-magnetic spacers, shaped in some case, to resolve interference with the light exits. The novel type of longitudinal extensions, introduced to solve the issue of insufficient space between the magnets for installation and maintenance, has the additional advantage of removing the magnetic field saturation in the pole tips.

Quadrupoles Q24$_{RB}$ behave also as reverse bends. The dipolar component is obtained by a transverse offset of about 5 mm of the magnetic axis with respect to the reference orbit. Their bore diameter is bigger than in the other quadrupoles (30 mm vs. 26 mm) to accommodate the displaced vacuum chamber. Table 5 lists the main parameters of the quadrupole magnets of Elettra 2.0. Fig. 8 shows the pre-engineered models.

Table 3
Elettra 2.0 magnets list.

Type	Family name	Total
Dipole	B64, B80	24, 48
Quadrupole	Q13, Q24, Q24RB	24, 48, 96
Sextupole	Sx12, Sx16, Sx20	60, 132, 48
Octupole	Oc14	48
Corrector	CHV	24
Fast Corrector	FCHV	72
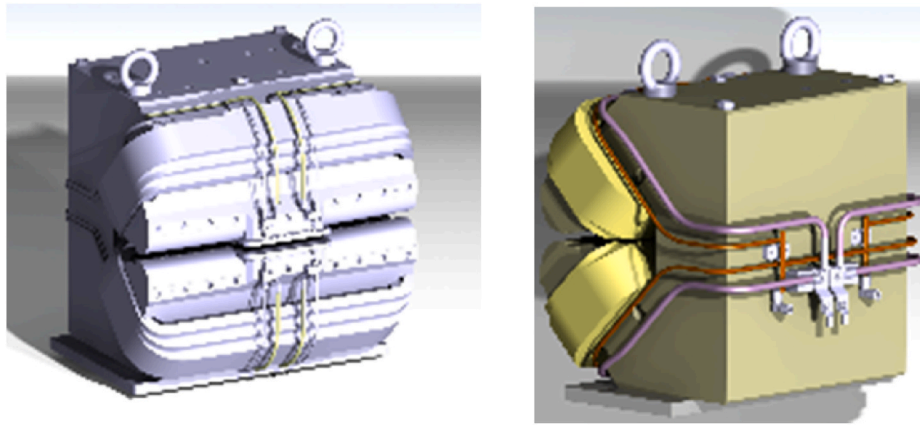
Fig. 6. B80 (left) and B64 model.

Table 4
Dipoles main parameters for operation at 2.4 GeV.

Parameter	B80	B64	Units
Iron	solid	solid	
Overall length	770	630	mm
Pole length	750	600	mm
Magnetic length	799	642	mm
Nominal current	246	241	A
Nominal power	1.9	0.87	kW
Coolant total flow	3.4	3.1	l/min
Nom. temp. rise	8.1	4.0	°C

4.3. Sextupoles

Sextupole magnets are grouped into 5 families, Sx12, Sx16, Sx16s, Sx20 and Sx20s. Similar to the quadrupoles, interference with the light exit chambers was resolved through shaping the poles. The sextupoles have been designed with laminated iron to integrate correction coils. The Sx16s and Sx20s families, equipped with 12 additional coils (2 for each pole), can provide either horizontal and vertical orbit correction (SxCH, SxCV), or skew quadrupole field (SxQs). Table 6 lists the main

parameters of the Elettra 2.0 sextupole magnets. Table 7 lists the sextupoles' additional function parameters. Fig. 9 shows the pre-engineered models.

4.4. Octupoles

The octupole magnets of Elettra 2.0 belong to one family, Oc14. Each arc hosts one octupole (hence, two per achromat). They have a laminated iron core, surrounded by 8 additional coils (one for each pole), to provide horizontal and vertical orbit correction. The relatively large bore diameter of 48 mm is due to the housing of the vacuum chamber, whose cooling system requires a minimum gap between the poles of at least 8 mm. To minimize the number of elements in each arc, the main coils of only one octupole in the achromat will be used to produce a quadrupole gradient; the secondary coils will generate the octupole field. Table 8 lists the octupole main parameters, while Table 9 lists the octupoles' additional functional parameters. Fig. 10 shows the pre-engineered models.
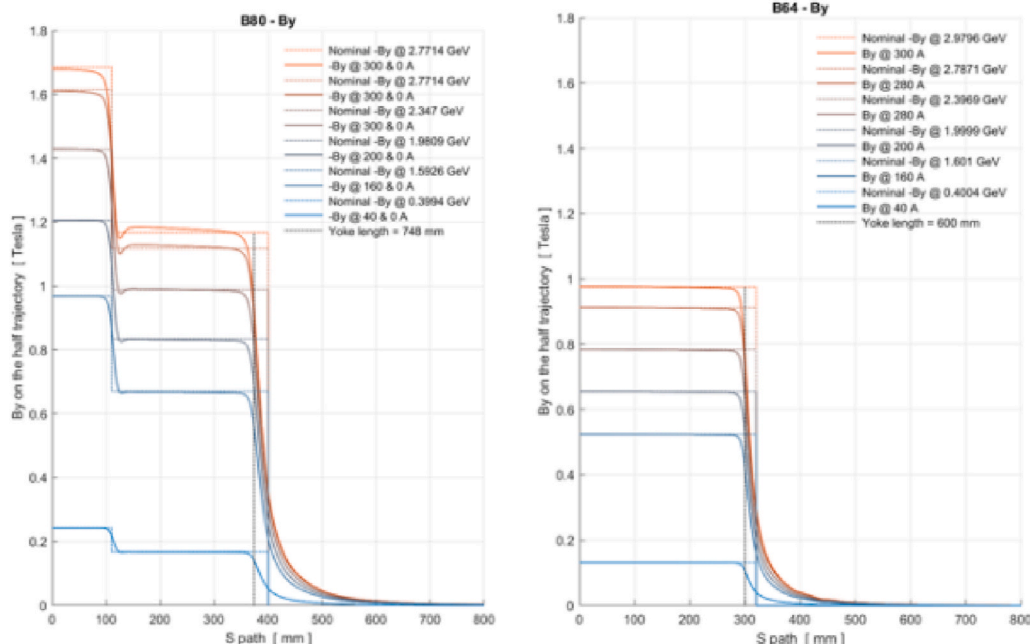

Fig. 7. B80 (left) and B64 vertical dipolar magnetic field along half length, starting from the middle of the magnet.

Table 5

Main parameters of quadrupole magnets.

Parameter	Q13	Q24	Q24$_{RB}$	Units
Iron	solid	solid	solid	
Overall length	130	240	240	mm
Pole length	90	222	222	mm
Bore diameter	26	26	30	mm
Mag. length	105.5	240.9	241.4	mm
Max. current	100	100	100	A
Max. B2	38.5	62.3	49.3	T/m
Max. power	303	934	934	W
H_2O total flow	0.76	1.53	1.53	l/min
Maximum ΔT	5.7	8.8	8.8	°C
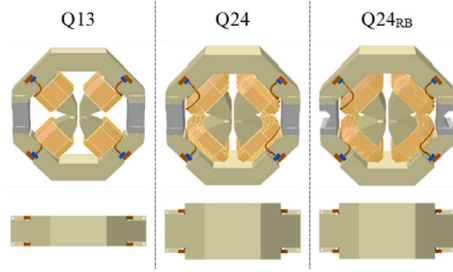
Fig. 8. Model of quadrupoles Q13, Q24 and Q24$_{RB}$.

Table 6

Sextupole main parameters.

Parameter	Sx12	Sx16/s	Sx20/s	Units
Iron	Laminated			
Overall length	170	210	230	mm
Pole length	110	150	190	mm
Aperture Diam.	30	30	30	mm
Magn. Length	120.5	160.0	200.0	mm
Max. current	100	100	100	A
Max. B3	5583	5626	5707	T/m^2
Max. power	528	588	600	W
H_2O total flow	0.79	0.73	0.73	l/min
Maximum ΔT	9.2	11.7	12.0	°C

Table 7

Sextupole additional function parameters.

	Sx16/s		Sx20/s		
	CH	CV	CH	CV	
Parameter	sQ		sQ		unit
Mag. length	158	156	197	196	mm
Max. integr. B1	62	36	79	45	Gm
Mag. length	128		168		mm
Max. integr. B2	0.54		0.70		T

4.5. Correctors

Pure corrector magnet (steerers) are grouped into two families, CHV and fast-CHV. The former is iron-dominated, the latter is made of coils installed around the input flanges of the dipole magnets' chamber. The effect of the 316L flanges on the distribution of the fast-CHV field lines has been simulated. The resulting cut-off frequency is ~5 kHz. The corresponding power converter is expected to have a bandwidth of up to 10 kHz at 2 A current amplitude. The maximum integrated field of the two families for the maximum PC current of 24 A, in the horizontal and vertical plane (vertical and horizontal correction, respectively), is: 80 Gm and 120 Gm for the CHV, i.e., 1.0 mrad and 1.5 mrad at 2.4 GeV; 1.3 Gm and 2.0 Gm for the fast-CHV, i.e., 16 μrad and 25 μrad at 2.4 GeV.
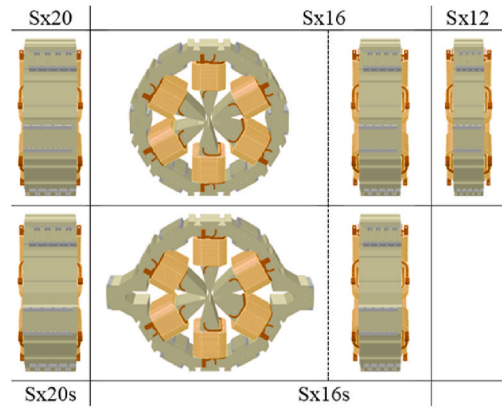

Fig. 9. Model of sextupoles Sx12, Sx16, Sx16s, Sx20 and Sx20s.

Table 8

Main parameters of octupole magnets.

Parameter	Oc14	Units
Iron	Laminated	
Overall length	140	mm
Pole length	80	mm
Bore diameter	48	mm
Magnetic length	160.0	mm
Max. current	100	A
Maximum B4	174783	T/m^3
Maximum power	480	W
H_2O total flow	0.83	l/min
Maximum ΔT	8.0	°C

Table 9

Octupole additional function parameters.

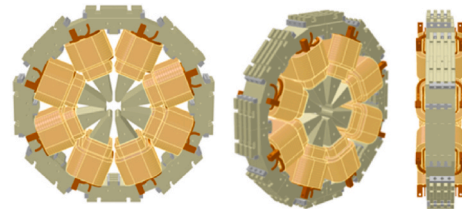| Parameter	Q$_{100A}$/Oc$_{20A}$	Units
Magnetic length	140	mm
Maximum integr. B1	40	Gm
Magnetic length	110	mm
Maximum B2	10.73	T/m
Magnetic length	141	mm
Maximum B4	49938	T/m^3

Fig. 10. Model of Oc14 octupole magnet.

4.6. Super-bends

Super-bends are dipole magnets supplied with superconducting coils to reach dipolar field intensities much larger than possible with ordinary room-temperature coils [31,32]. An innovative compact design, including superconducting, side quadrupole magnets, will be developed for Elettra 2.0. The novel cryogenic solution will combine the benefits of a liquid-He cooled inner magnet with a liquid-He-free upper cooling stage [33]. This stage contains 2 cryocoolers which sub-cool a liquid He tank. A C-shape design of the dipole magnetic pole will allow the magnet to slip over the vacuum chamber for, e.g., installation, alignment,

maintenance.

The three super-bends will be installed symmetrically around the Elettra 2.0 ring, by replacing three B64 dipole magnets in achromats number 4, 8 and 12, see Fig. 11. The super-bend total bending angle of $6.5°$ will be provided by three center-symmetric longitudinal sections. The pure dipole field in the edge sections amounts to 0.594 T over 0.36 m, for a bending angle of $1.53°$ each. The central region shows 6 T magnetic field over 0.72 m, for a bending angle of $3.44°$. The edge sections also provide a quadrupolar field gradient of 16.2 T/m, tuneable by ±20 %. A left-right unbalance of 4 windings supplying currents produces a transverse gradient. The windings are inserted in a ferromagnetic yoke. Table 10 lists the main parameters of the central and lateral section of the super-bend.

The pumping system shall guarantee an inner pressure of the vacuum chamber in the super-bend lower than 10^{-8} mbar, with a leak rate of 10^{-8} mbar l/sec. Two cold heads will be installed to keep the thermal shield and the current leads below 60 K, as well as to reduce the vapor pressure of the liquid-He bath. A dedicated system of heat exchanger will cool the yoke below 4.2 K.

The cold mass is conduction-cooled by virtue of a thermal contact between the lower side of the liquid-He tank and the heat exchanger, in direct contact with the cold heads. The role of the liquid-He tank is to speed up the cool-down time, to reduce the recovery time after a quench, and to keep the system as cold as possible in case of out of service of the cryo-heads. The vapor pressure of He in the tank will be 470 mbar at 3.5 K. The magnet could be cooled even without liquid-He, thanks to the connection with the second stage of the cold heads. The heat exchanger will be mechanically connected with screws, and an epoxy resign will be used and at the two interfaces. The thermal load of the two stages of the cryogenic system are, respectively, 72 W and 1241 W.

5. Power converters

The Elettra 2.0 electron optics require a significant number of magnets and additional coils to be energized individually. More than 1200 DC power converters (PCs) are foreseen. A synergic design of the magnets and the associated PCs led to standardization: three current ranges (300 A, 100 A, 25 A) and, consequently, only three different types of PCs. While the 20 V/300 A PCs (72 units) have been ordered on the market via a call-for-tender procedure, the 15 V/100 A and the 20 V/25 A units (together account to about 1000 units) are an in-house design and their procurement will follow a "built-to-print" procedure.

To avoid water cooling of the PCs, leaks of which – though rare – can fatally damage the cooled circuits, air-cooling was chosen for Elettra 2.0. This choice requires a stable air temperature and a constant air flow, to guarantee the stability of the output current of the PCs.

The one-to-one correspondence of power converter to magnet implies a large number of power cables to the storage ring. Their length will be minimized by placing the converters in the same positions of the present cabinets, thereby using the existing cable trays. Shorter cables
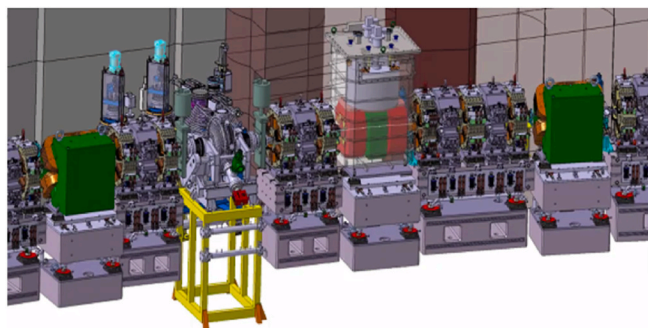

Fig. 11. Super-bend in Elettra2.0. The cryostat with cold mass and liquid-He tank is shown in the arc, in between two standard dipoles.

Table 10
Main parameters of the super-bend central section.

Item	Center	+X side	-X side	Units
SC material	NbTi	NbTi	NbTi	
Current at 6.0 T	126	208	94	A
Wire diameter	0.85	0.7	0.7	mm
Max. field on the conductor	7.3	3.2	1.5	T
Current density	161			A/mm^2
Cu/SC	1.3			
Load line perc.	82	54	25	%

will limit electromagnetic interferences, in turn avoiding in most cases the need for shielded cables.

The PCs grid connection shall be split in two, normal AC mains for power, and UPS (Uninterruptable Power Supply) for control. If a power outage occurs during a thunderstorm event and some devices power off, the control section, fed by the UPS line, will still allow the control system to perform some post-mortem analysis. To minimize the number of AC cables, custom made PDUs (Power Distribution Units for 3 and 1-phase) with required plugs will be adopted.

In summary, the following optimized design has been reached after close interaction with working teams in charge of magnets and controls.

- 1 PC model for 2 types of dipoles;
- 1 PC model for 3 types of quadrupoles and 3 types of sextupoles, 1 octupole and the dipole trim coils;
- 1 PC model for embedded correctors, fast correctors and skew quadrupoles.

Table 11 summarizes the specification for the power converters.

5.1. Dipole and multipole power converters

The main distinction among the different types of power converters is the type of load to supply. The output current and voltage of the dipole power supplies are compatible with high-performance products available on the market.

Multipoles PCs will be an in-house development, based on well-established internal know-how [34–36]. They comprise about 75 % of all power supplies. The power section is formed by hard-paralleling two power boards capable of sourcing/sinking 60 A each. The power mosfet is a OptiMOS™-5 Power-Transistor from Infineon, showing GaN-like specifications. The power lines have been carefully designed to minimize stray inductance and perform minimal routing. The boards are driven with a symmetrical power feedline; output lines with symmetrical connections ensure the perfect matching of the output current in each board. This 4-Quadrant power converter is shown in Fig. 12. If unipolar operation is required, the remaining quadrants can be disabled by means of firmware. Current sensors are mounted on the input stage, to shut down the machine in case of unbalance of the input current.

5.2. Correctors, skew quadrupoles and fast correctors

Similar to the multipole magnets, skew quadrupoles, correctors and fast correctors will also be powered by an in-house-built PC. An effort was made to share as many components as possible with the multipoles PC. Due to the lower power requirements, only a single power board is needed, as shown in Fig. 13.

A board prototype has been built and tested to maintain. stability of the output current over 8 h, as shown in Fig. 14. The 20 ppmpp/FS limit requirement is fully met, showing an outstanding moving average (16 points) of 6 ppmpp/FS stability over the observation time, in an uncontrolled temperature environment. The output current ripple measurement shows a residual noise with a 200 kHz bandwidth of 300uApp = 12 ppm/FS, well within the specification.

Table 11
Power converters specifications.

Magnet	Dipole	Sext	Quad	S-Quad	Corr	Oct	TrimC	Fast-CHV	Unit
PS Mode	Unipolar			Bipolar		Unipolar	Bipolar	Bipolar	
PS Type	PSB	PSQS		PSC		PSOC	PSB_T	PSFC	
Max I$_{out}$	**300**	**100**		**25**		**100**	**100**	**25**	A
Max V$_{out}$	20	15	15	10	10	10	5	*TBD*	V
Max P$_{out}$	6	1.5	1.5	0.2	0.2	1.0	0.5	25*Vout	kW
Range	5–95	5–95	5–95	Full	Full	5–95	Full	Full	% Iout
8h-stability	30	100	25	50	20	100	100	20	ppm$_{pp}$/FS
Ripple	30	100	100	100	500	100	100	500	ppm$_{pp}$/FS
Total PS	72	432		432		48	48	192	1224
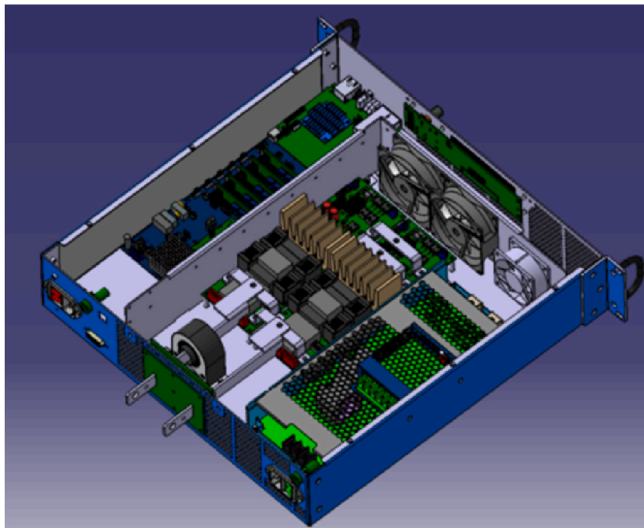
Fig. 12. A38100, 4-Quadrant multipole power converter.
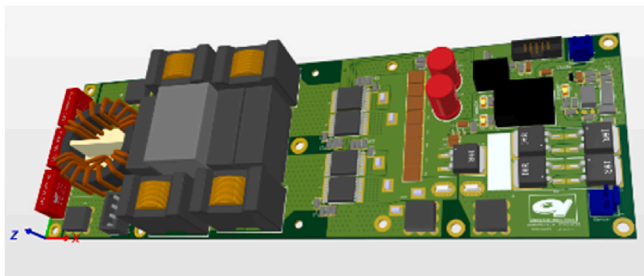
Fig. 13. 60 A, 4-Quadrant power converter.

6. Girders

The storage ring design requires a stiff support system to reduce the impact of vibrations on the electron beam orbit and to maintain a high thermal stability, as well as low static deformations. The magnet support system must be easy to transport, to align, but also must be cost-effective [37–39].

Girders are used to sustain magnets, vacuum chambers, BPMs and other instrumentations. Given the 12-fold periodicity of the Elettra 2.0 magnetic lattice, each sector will have 8 multipole girders and 6 dipole girders, see e.g. Fig. 15. The storage ring magnets and the vacuum chambers rely, in total, on 168 girders.

A standard design but with different lengths of the girders has been chosen as the most cost-effective solution. The Elettra 2.0 girders consist of granite slabs 0.8 to 1.57 m-long, 0.6 m wide and 0.3 m thick. Granite was chosen because of its low coefficient of thermal expansion, high stiffness and extremely good flatness at its top face.

Table 12 shows the storage ring magnets' alignment and the long-term stability specifications. Accordingly, the relative positioning accuracy of the magnets on each girder should be less than 20 μm, better than 50 μm from dipole to dipole, and the alignment accuracy between girders should be less than 50 μm.

The girder's positioning relies on three manual alignment systems, with a spherical washer at its bottom to provide a perfect isostatic constraint. The adjustment range of the feet is ±15 mm in all directions. Adjustment screws set transversal, longitudinal and yaw regulation. In the vertical plane, pitch and roll adjustment is done through M52 screws. The size of the screws takes care of both the static and the dynamic behaviour of the system in terms of vibrations. All the adjustments are independent and free of parasitic movements. Two further feet with spherical washers to prevent tipping can be tightened after the alignment to increase the natural frequencies of roll and pitch angles, and to minimize static deflection of the magnet–girder system while avoiding rollover during the girder placement. Since the Elettra 2.0 beam height was fixed to 1.3 m, a concrete pedestal will reduce the
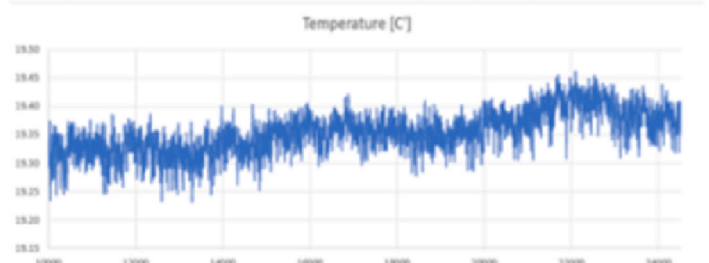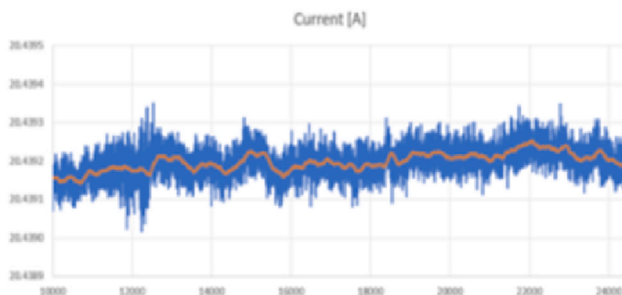
Fig. 14. 8-h stability test of single power board PC.
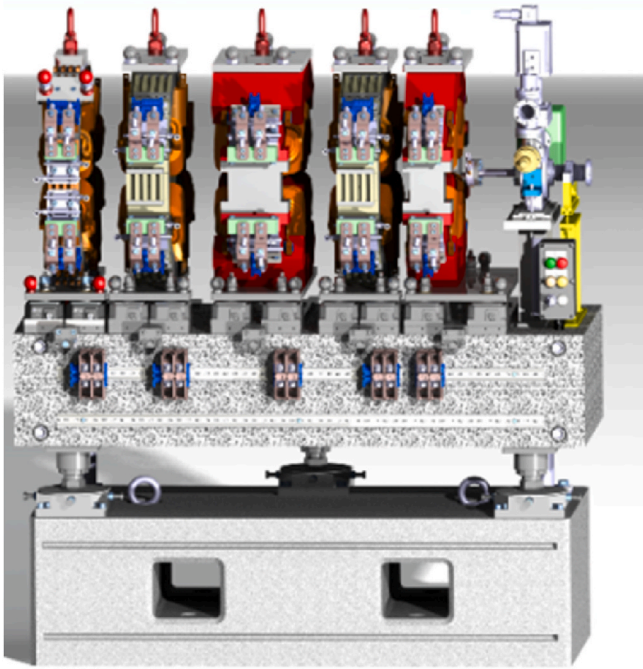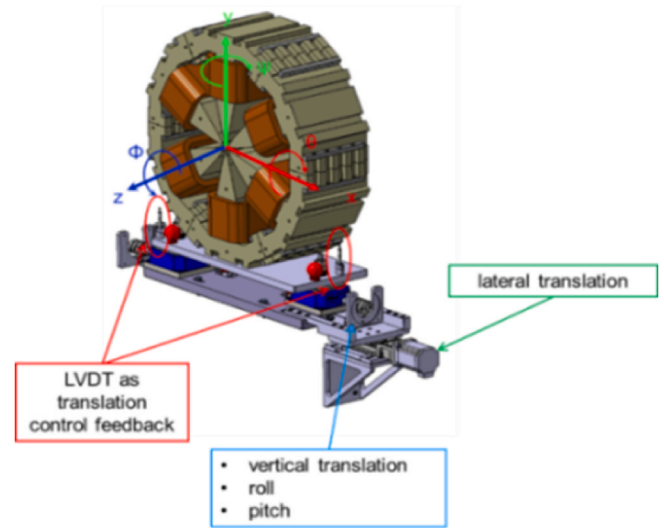
Fig. 15. Elettra 2.0 girder design.

Fig. 16. motorized system using Airloc 505-KSKC wedge-mount levelling feet.

theory and a finite element method has been carried out [41,42], from which the lowest mode at 64.9 Hz emerges. This frequency is far from all main vibration sources, such as the flow of the cooling water, air conditioning, and power supplies. Nevertheless, a provisional design of an auxiliary damping system will be produced.

7. Insertion devices

As the layout of Elettra 2.0 allows hosting the same IDs already in use at Elettra, they could in principle be retained in the upgrade. However, for the new high-performance beamlines that are planned to take advantage of the lower electron beam emittance, new undulators are being designed and constructed. Space is also available in some of the short, small-dispersion straight sections. Compact undulators and few-pole wigglers are therefore being developed to make optimal use that space.

The brilliance plot in Fig. 17 (see also Fig. 5) shows the tuning ranges for a selection of the new IDs, whose emission spans from EUV to hard X-rays. They are all based on NdFeB permanent magnets, in pure or hybrid configuration. Their main parameters are listed in Table 13, where the number of periods (N), the magnetic length (L), the maximum horizontal and vertical deflection parameters (K_X, K_Y) and the minimum magnetic

Table 12

Elettra 2.0 alignment and stability requirements. X = horizontal, Y = vertical, Z = longitudinal coordinate.

Magnets	Alignment [µm]			Stability [nm]	
	ΔX	ΔY	ΔZ	ΔX	ΔY
Quadrupoles Sextupoles	20	20	300	150	25
Dipoles	50	50	300	200	30
Girders	50	50	300	600	70

girder vertical dimensions, making the whole system stiffer.

Each girder carries about 1500 kg of magnets, bringing the payload, including the adjusting system, to a maximum of 2500 kg. To reduce the on-site installation time, assembly and alignment of magnets on the girder will be performed before the girder installation, in a dedicated, early assembly area. By means of a motorized actuator, a base plate can be precisely aligned along the x-axis, sliding on the granite top face; two pivots rigidly fixed to the girder avoid cross-talk. The positioning of the pivots will be done using a laser tracker. After reaching its final position, the base plate will be locked by T-nuts to the girder.

Three modified Airloc 505-KSKC wedge-mount levelling feet will be motorized, and will be used to align each multipole magnet along y, θ and φ (vertical, roll, azimuthal coordinate, respectively). At the end of the alignment, the system will be locked by threaded rods screwed to the base plate. LVDT sensors (Linear Variable Differential Transformer) will guarantee a feedback for the motorized system, see Fig. 16.

A static FEM analysis through ANSYS code was performed to optimize the position of the supports, and to minimize the deformation under girder's and magnets' own weight. The maximum vertical misalignment between the magnets, due to their weights, is ~5 µm. This value is far smaller than the design tolerance, and the alignment system will easily compensate the static deflection of the girder.

The system must allow a high-precision alignment of the magnets, but at the same time it must be stiff and unresponsive to vibrations [40]. Since the slim geometry of the magnets leads to low frequency pitch modes, a cardan joint shaft with adjustable length fixed between magnets will define a further constraint that improves the stiffness. To validate the girder design, a modal analysis based on linear vibration
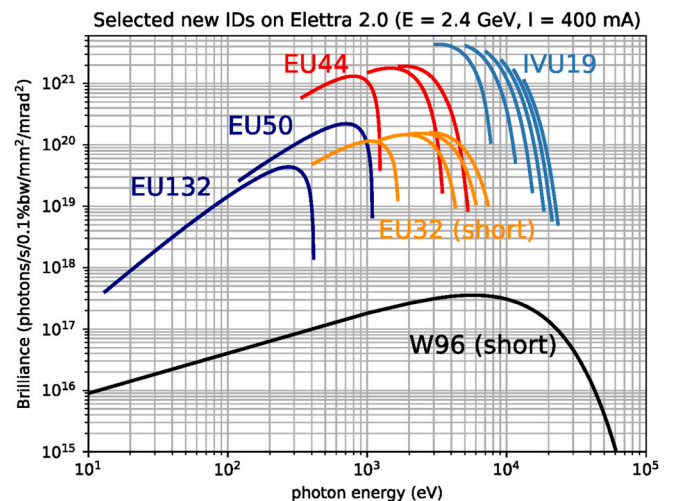

Fig. 17. Tuning curves for some representative new IDs. The calculated brilliance is for an ideal electron beam with zero emittance and zero energy spread.

Table 13
Main parameters of new IDs.

Device	N	L [m]	K_X	K_Y	g_{MIN} [mm]
EU132	18	2.6	7.8	4.9	18 (fixed)
EU50	28	1.5	2.9	4.0	12
EU44	2 x 45	2 x 2.0	2.3	2.3	12
IVU19	105	2.0	–	1.9	5.2
IVU22	90	2.0	–	2.6	5.2
EU32		0.8	1.9	2.5	9 (fixed)
W96	7.5	0.8	–	16	12 (fixed)

gap (g_{MIN}) are reported.

7.1. Elliptical undulators

EU44 and EU50 are conventional APPLE-II type, adjustable gap undulators, covering the soft x-ray region. The former undulator, composed of two separate 2 m-long sections is shown in Fig. 18-left. Gap and phase motion control is realized with Beckhoff TwinCAT3 components, brushless motors and Fagor absolute linear encoders. For local control, a graphical user interface is implemented on programmable touch panels, while for remote control a TCP/IP server running on the PLC can be accessed through Ethernet.

EU50, shown in Fig. 18-right, is a refurbished FEL undulator prototype, whose original motion control has been completely rebuilt using the new style Beckhoff components and absolute linear encoders.

EU132 is a fixed-gap APPLE undulator, whose geometry (see Fig. 19) was optimized to suppress the on-axis dynamic integrals generated by the field gradients appearing in this type of magnetic structure in certain operation modes [43]. Polarization is selected, as normally done in the APPLE-type undulators, by moving two diagonally opposite arrays ("phase" motion). For any given polarization, the field strength, and therefore the radiation wavelength is adjusted by shifting the upper magnet arrays relative to the lower ones ("jaw-phase" motion).

Fig. 20-left shows a CAD model of this undulator. A mechanism to manually separate the upper and the lower arrays allows installation and removal of the device with the vacuum chamber in place. A close view of one end of the magnet is shown in Fig. 20-right. Given the novelty of its design, the undulator has been recently installed on Elettra to test its operation and characteristics.

7.2. In-vacuum undulators

To serve three new micro-focus beamlines (μXRD, μXRF and HB-SAXS), permanent magnet, in-vacuum undulators (IVUs) will be constructed. A minimum gap of 5.2 mm and a length of 2 m were chosen for these devices to ensure an adequate aperture for the nominal electron beam optics and to leave enough space in the straight sections for other necessary machine equipment, such as the kickers of the multi-bunch feedbacks. A hybrid structure with a period length of 19 mm (IVU19) will allow good coverage of the photon energy range from 3 to 15 keV. In one case (μXRF) the period will be increased to 22 mm (IVU22) to extend the tuning range continuously down to 1.5 keV.

7.3. Short insertion devices

The short straight sections of Elettra 2.0 are characterized by horizontal dispersion as low as 58 mm, see Fig. 2. Consequently, beam dimensions are similar to those in the long straights. Despite a useable length of only 80 cm, short IDs offer a means to increase the number of beamlines available in the new machine. A good example is the 1.8 T wiggler recently designed, assembled and characterized in the Elettra ID laboratory. The gap is fixed and the field can be switched off, when needed, by shifting horizontally the whole device out of the electron beam path. This translation is remotely controlled. The design features a motorized opening system for easy installation and maintenance, giving access to the vacuum chamber for bake-out or similar operation, see Fig. 21.

The measured magnetic field agrees well with the numerical model, see Fig. 22-left. Adjustable end-magnets and "magic fingers" were used to correct the integrated dipole and multipole errors to negligible levels. Despite having only 15 poles, the brilliance of this new source in Elettra 2.0 will be superior to the existing 4.5 m, 1.5 T wiggler presently serving the XRD beamline at Elettra. This advantage is due not only to the higher field and the smaller beam emittance, but also to reduced depth-of-field effects [44] for the shorter device.

Three more short, fixed-gap, adjustable-phase IDs are under development. EU32, shown in Fig. 22-right, is under construction at the ID laboratory. It will provide both linear and elliptical polarization in the tender X-ray regime.

8. Effects of IDs on electron beam optics and dynamics

The effect of IDs on the electron linear and nonlinear dynamics was studied through kick maps [45]. For each ID listed in Table 14, a nonlinear map was generated at the minimum gap (stronger field, hence maximum perturbation is expected) and for different polarization modes.
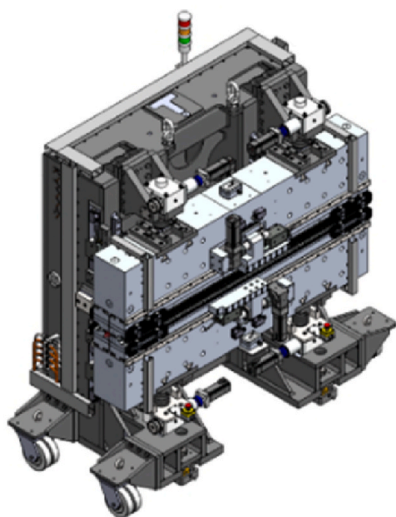

Fig. 18. Left, CAD model of one of the two modules of EU44. Right, the refurbished EU50 in the ID laboratory.
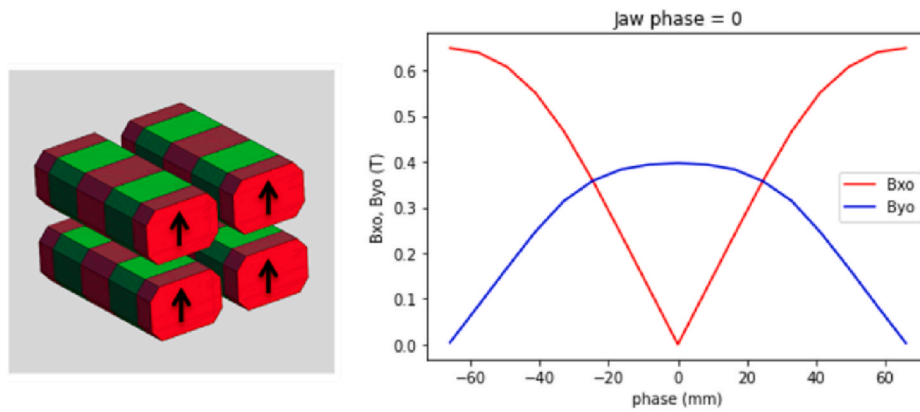
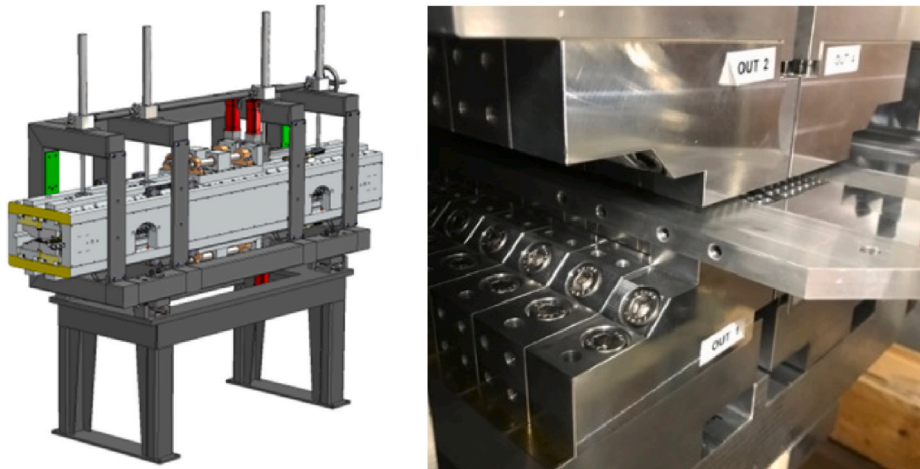**Fig. 19.** Magnetic structure of EU132 (left), and measured peak field vs phase at zero jaw-phase.

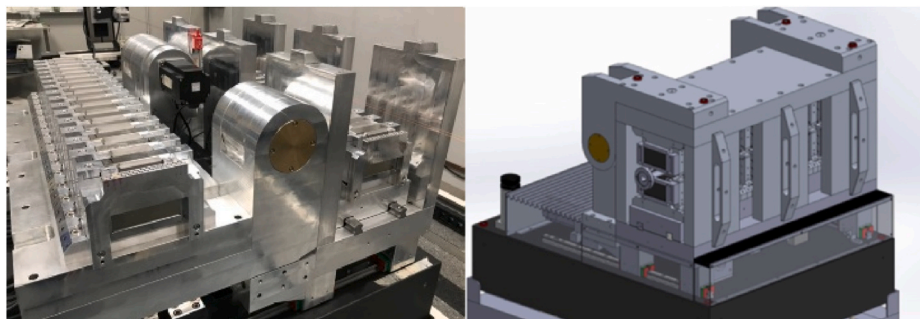**Fig. 20.** Left, CAD model of EU132. Right, EU132 and its vacuum chamber.

Fig. 21. The wiggler in "maintenance mode" (left) and CAD model of the wiggler in "operation mode" (right).

The simulations were carried out with the elegant code, after a successful benchmark with AT [46], in terms of beta-beating and dynamic aperture, for IDs both in the long and in the short straight section. The effects of ideal IDs can be classified as follows.

- Beta-beating and linear tune shift. These effects depend on the ID parameters and on the betatron functions at the ID. EPUs will perturb both transverse planes.
- Amplitude-dependent tune-shift and fourth order resonances generated by higher order magnetic field components. For an ideal undulator and by virtue of the symmetry of the magnetic poles, only odd multipoles will be excited. Reduction of the dynamic aperture and of the energy acceptance is expected eventually.

- IDs modify the radiation damping, resulting in a change of the equilibrium emittance, energy spread, and damping times. Depending on the dispersion function at the ID location (only short sections in Elettra 2.0), the horizontal emittance could be reduced or increased.

In addition, the following perturbations to the particles motion are expected from realistic IDs.

- Non-zero first and second field integral. Principal components of these integrals are dipole-like. They can be easily corrected by means of steering magnets installed at the edges of the straight section.
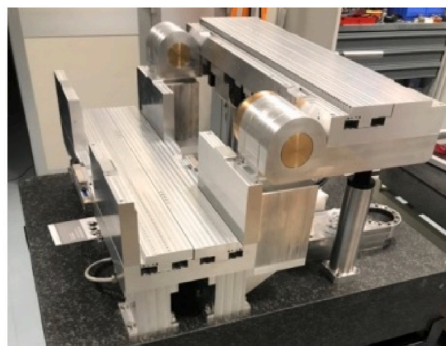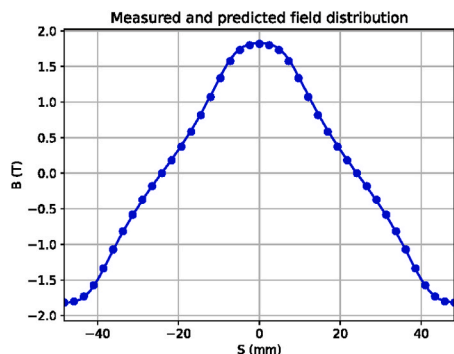- Non-systematic higher order field components.

Fig. 22. Left, measured (dots) and predicted (line) field distribution along the central wiggler period. Right: mechanics of EU32.

Table 14

Main parameters of Elettra 2.0 IDs. The two values of B_0 are for linear horizontal and vertical polarization. EPU = elliptically loarizing undulator, APU = adjustable phase undulator, W = wiggler, IVU = in-vacuum undulator.

ID	L [m]	B_0 [T]	λ [cm]
Figure-8	2×2.2	0.75/0.14	14.0
EPU13.2	2.6	0.39/0.63	13.2
EPU12.5	2.1	0.77/0.60	12.5
EPU10.0	2×2.0	1.02/0.78	10.0
EPU7.7	2.1	0.92/0.64	7.7
EPU6.0	2.2	0.78/0.51	6.0
EPU5.0	1.5	0.85/0.62	5.0
EPU4.8	2.0	0.58/0.34	4.8
EPU4.4	2×2.0	0.59/0.56	4.4
EPU3.2	0.8	0.83/0.49	3.2
APU3.6	0.8	0.67	3.6
W9.6	0.7	1.82	9.6
IVU	3×2.0	1.17	2.0

8.1. Impact of short IDs

Simulations showed that the linear optics distortion from IDs in the short dispersive straight sections is less than 2 %. No local correction is foreseen since it is easily tolerable. The most significant effect on the equilibrium emittance is due to two mini-wigglers (W9.6) in cells 5 and 11. The maximum field of those devices was specified on the basis of the tolerable emittance growth, i.e. 5 %. Tracking studies revealed no significant reduction of the dynamic or the momentum aperture.

One of the mini-wiggler is a fixed gap device. It will be translated horizontally by 80 mm with respect to the vacuum chamber to zero the magnetic field on the beam path. The effect of the movement of the wiggler on the dynamics of the stored beam was simulated by fitting the field integral piecewise, in 10 mm-steps. The fit coefficients complemented the kick map from RADIA [47]. Orbit, tunes, momentum acceptance and lifetime were calculated at each step. The most relevant effect of the movement is a 40 % transitory reduction of the lifetime. Given the relatively fast process (seconds), no beam injection will be required when the device will be "switched off" or "on".

8.2. Impact of long IDs

Only one of the 11 long straight sections will be connected to two beamlines, each receiving light from a different undulator segment. A chicane separates the cone of emission of the two undulators by 2 mrad. Simulations indicate that a correction scheme of the linear optics, taking into account both undulators, is not necessary, since the beta-beating produced by the high energy undulator EPU6.0 is less than 3 %. Quadrupole triplets at the edges of the straight section will compensate the effect of the low energy undulator only, EPU12.5.

For all other long IDs, the edge quadrupole triplets will compensate

betatron phase advance and betatron function across the undulator. Tunes will be corrected globally, whenever necessary. Fig. 23 shows, as an example, the beta-beating for the perturbed and the corrected machine, when EPU10.0 is set to minimum gap. Despite the corrected optics, particle tracking revealed a significant reduction of the on-energy dynamic aperture when several IDs were set in vertical polarization mode.

Frequency map analysis highlighted the excitation of a 4th order resonance line ($4\nu_x$), in turn traced back to the octupole component of the field. The issue was then solved by changing the horizontal tune from 32.270 to 32.240, and minimizing the resonance driving terms. Figs. 24 and 25 show the computation of the dynamic aperture and frequency map after linear optics correction only, at the original tune of 32.270, and after tune change.

8.3. Impact of all IDs

The largest perturbation is expected with all IDs closed to their minimum gap and, whenever accessible, the EPUs in vertical polarization mode. This situation was simulated, with local, linear optics correction when the individual ID effect on the beta-beating was larger than 5 %. The resultant beta-beating is 3 % in the horizontal plane and 6 % in the vertical. The horizontal emittance was reduced from 226 p.m. rad to 218 p.m. rad while the energy spread remained substantially unaltered at 0.09 %. The momentum acceptance, simulated including physical restrictions and evaluated at the sextupole magnets, was reduced from 4-5%–3 %, see Fig. 26, where the RF momentum acceptance is 4.5 % with 3HC at work. The dynamic aperture is the one shown
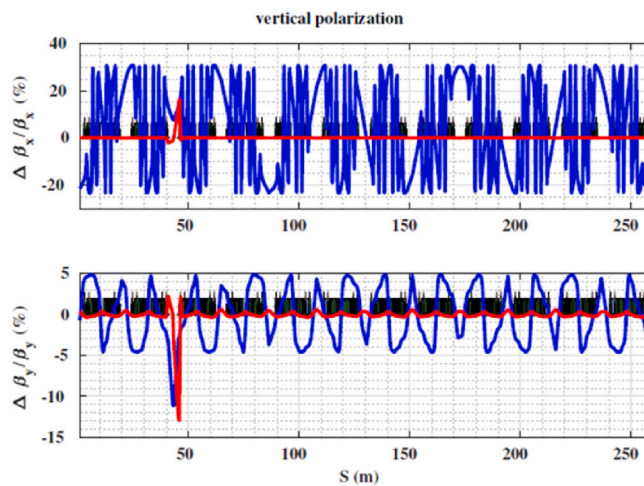

Fig. 23. Horizontal (top) and vertical (bottom) beta-beating with EPU10.0 in vertical polarization mode. Blue: uncorrected optics. Red: with local optics correction.
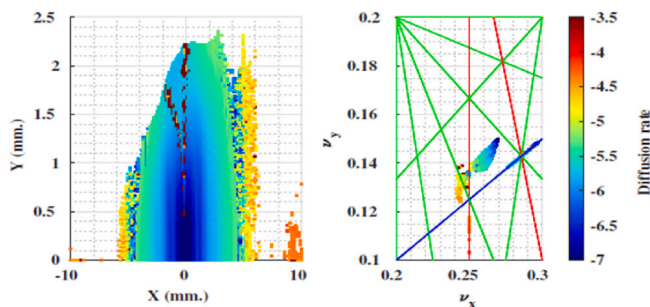
Fig. 24. Dynamic aperture (left) and frequency map (right) with EPU10.0 in vertical polarization mode, after local optics correction, for $\nu_x = 32.270$ (top).
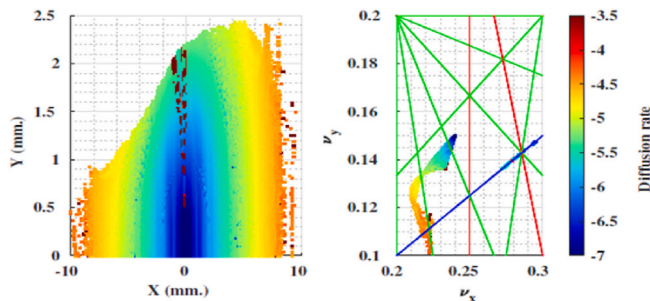

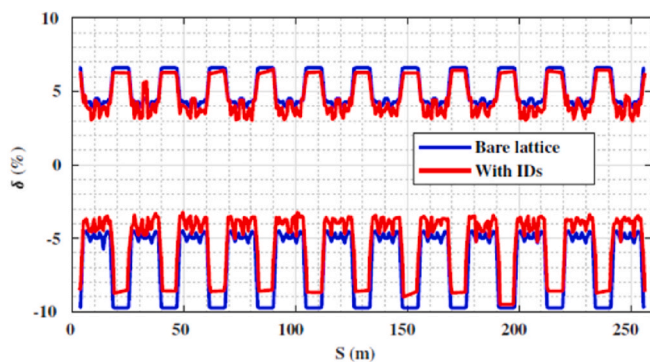**Fig. 25.** Same as in Fig.24, now with the new tune $\nu_x = 32.240$.

Fig. 26. Momentum acceptance with and without IDs.

in Fig. 3, calculated in the presence of 20 seeds of machine errors. In spite of its reduction, especially in the horizontal plane, the dynamic aperture is still wide enough to guarantee an injection efficiency larger than 95 %, since the beam will be injected at -4 mm from the reference orbit.

The perturbations to the linear and nonlinear electron optics due to the field of the three super-bends are small. The horizontal emittance is increased by less than 5 % from the insertion of the super-bends in 3 symmetric locations of the lattice (Section 4, 8 and 12 of Elettra 2.0), and its maximum variation with asymmetric placements of the super-bends is less than 10 %. In all scenarios simulated, a local correction of the Twiss functions was implemented by using a few quadrupoles in proximity of the super-bends, with less than 2 % changes in the quadrupoles' strength from their nominal value. The linear dispersion function is corrected as well, as shown in Fig. 27 for the nominal symmetric configuration. The reduction of the dynamic aperture after correction of the linear optics is negligible (not shown).

The individual effect of IDs, moved from zero to maximum field (i.e., gap closure), on the horizontal emittance is shown in Fig. 28 (the beam size variation is approximately half of that). Moreover, the combined

effect of randomly changing the field of the insertion devices from 50 % (pre-set during operations) to full field (excluding the superconducting wiggler) has been studied for 50 machines. The result, shown in Fig. 29, indicates that the total effect on the changing the beam size is less than 1 %. This change is well within the tolerance of 5 % as specified by the beamlines to guarantee optimal acceptance of radiation.

9. Vacuum system

The dense magnetic lattice with reduced magnet apertures of modern DLSRs implies a high heat load from synchrotron radiation (dipoles, IDs), large dynamic pressure in the vacuum chamber and tight specifications for the resistive wall impedance. A novel design of the Elettra 2.0 vacuum chamber and distributed pumping system has been conceived, to overcome greatly reduced conductance compared to that in Elettra. Large sputter ion pumps (SIP), largely used in Elettra, will be replaced by distributed non-evaporable getter (NEG) coatings and small NEG cartridges. Due to the tight space constraints imposed by the magnetic lattice, photon absorbers will be developed with discrete and distributed solutions, carefully designed for combining compactness despite high power-density loads. Most critical sections of the vacuum chamber will be water-cooled. Throughout the whole development phase, MonteCarlo simulation codes such as SynRad and MolFlow + have been used.

9.1. Vacuum chamber

The vacuum chamber of Elettra 2.0 will be made of different materials: stainless steel ($\sim$30 %), aluminium ($\sim$20 %) and copper ($\sim$50 %), with more than 90 % of the chamber coated with NEG film. A rhomboidal cross section of external (internal) dimensions 30 (28) mm x 20 (18) mm is installed inside multipole magnets. The outer height in dipole magnets is 35 mm.

The majority of Cu components, i.e., all rhomboidal chambers between the dipole magnets, will be made of silver-bearing oxygen-free Cu (Cu-OFS). This material is characterized by a higher temperature of recrystallization than the more widely used oxygen-free, high temperature conductivity copper (Cu-OFHC), at the expense of only 1 % smaller electrical conductivity.

Aluminum will be adopted for the long and narrow vacuum chambers of the IDs, because of its ease of manufacture and extrusion, and its being non-magnetic. The Al chambers will be internally coated with NEG to reduce the photon-stimulated desorption (PSD) and gas bremsstrahlung.

Copper Chrome Zirconium (CuCrZr) alloy will be used to fabricate photon absorbers and CF flanges. These components will be machined from one body, without welding or brazing [48,49]. Stainless steel (AISI 316L), generally cheaper than the aforementioned materials, will be used for the chambers inside the dipole magnets and the light exits, whenever properly integrated with photon absorbers.

9.2. Pumping system

NEG coating is nowadays widely used in particle accelerators when very low conductance chambers are needed [50,51]. This constraint applies to Elettra 2.0 as well. Ti–V–Zr sputtering on metal surfaces allows the significant reduction of the inner pressure during machine operation, hence, a longer beam lifetime related to residual gas scattering. The long and short rhomboidal straight sections, on which IDs will be installed, will be coated with NEG. This coating acts as a distributed pumping system and as a vacuum barrier for gas desorption generated in the upstream and downstream vacuum chambers made of different materials.

EG pumps and coatings are activated in situ, as final part of the bakeout procedure of all vacuum chambers. Activation of the NEG pumps is carried-out by means of their power controllers. Due to spatial limitations between the vacuum vessel and the surrounding magnets, thin
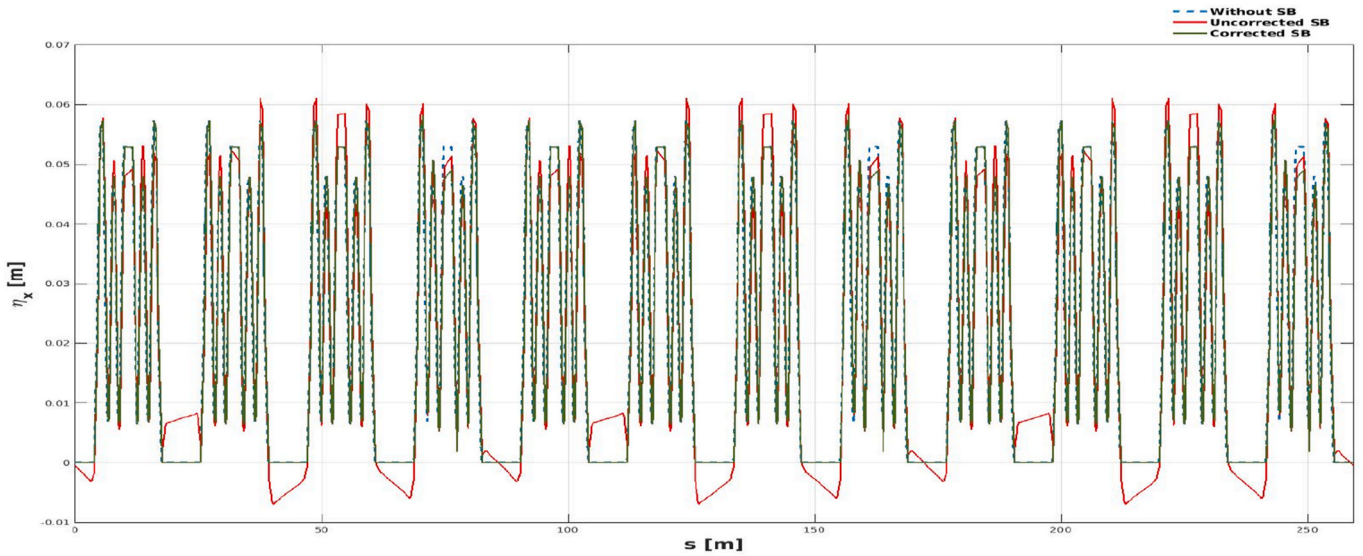
Fig. 27. Horizontal dispersion along Elettra 2.0 in the presence of 3 super-bends and linear optics corrections.
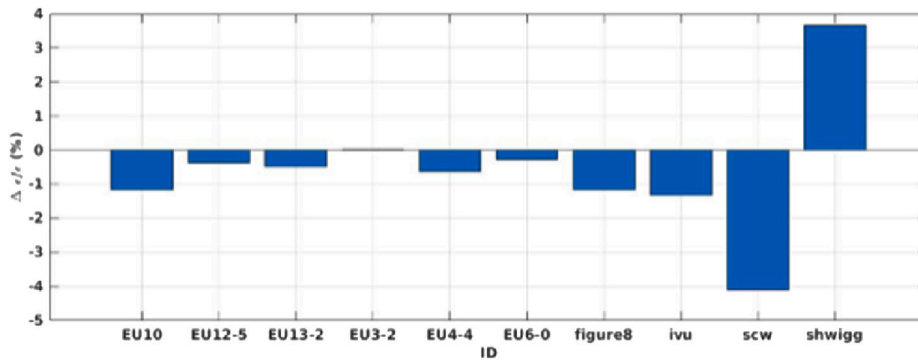

Fig. 28. Relative emittance variation from the individual setup of IDs, from zero to maximum field.
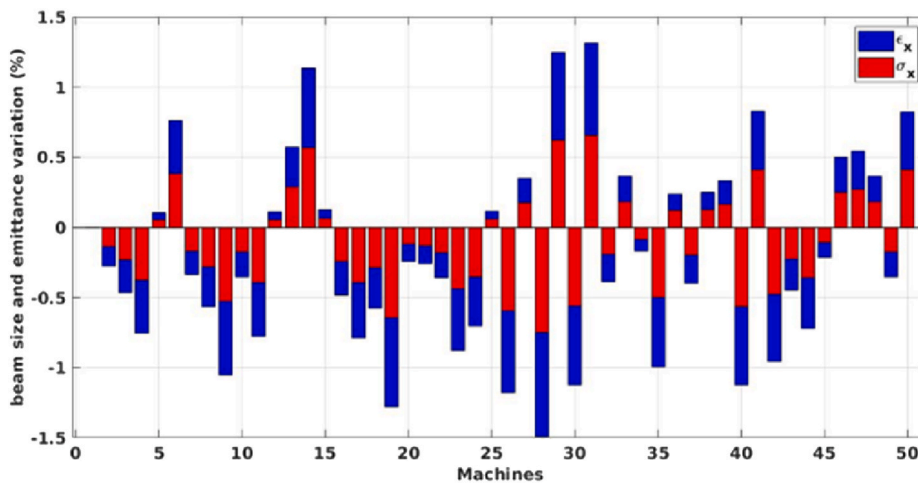

Fig. 29. Horizontal emittance and beam size change for 50 error seeds, by randomly changing all undulator fields from 50 % to 100 %.

heaters (0.6 mm thick), based on customized polyimide films, are permanently applied to rhomboidal, copper vacuum chamber. Stainless steel bending magnet vacuum chambers, where dipole magnets can be slid back, are heated using commercial heater tapes. The entire vacuum vessel must be heated to the recommended temperature (>180 C, 24 h) to have a complete activation of the NEG.

NEG coating is also expected to reduce significantly the conditioning time of the vacuum system. The extensive use of NEG coating, however, increases the machine impedance. To minimize that impact, the average coating thickness in Elettra 2.0 is set to 0.5 mm along the beam path, and to 1.5 mm elsewhere.

Conventional pumps are installed where either space permits or their

use is essential. A 55 l/s SIP and a 400 l/s NEG pump are installed in proximity of the dipole chambers to support the local pumping system of photon absorbers. A combined 500 l/s NEG pump plus 20 l/s SIP pump will be installed near the RF cavities.

Fig. 30 shows the partial pressure in the presence of PSD for Carbon monoxide (CO) and hydrogen (H_2) gases after 5Ah (Ampère-hour), 50 Ah, and 100 Ah of conditioning time. The simulations were first carried out with SynRad + to calculate the flux and the power distribution of radiation onto the inner surfaces of the vacuum chambers [51,52]. The results were then transferred to Molflow to calculate the PSD without and with stored beam in Elettra 2.0. The study provided also most important information for the evaluation of heat load on vacuum chambers and photon absorbers, and to calculate the equilibrium temperature of numerous components in the presence of suitable water cooling. Fig. 31 illustrates the vacuum components of one arc of Elettra 2.0. The long straight section (a) is made of Al chamber including RF section valves, SIP20 and a Penning gauge (b) on each side. It is followed by a photon absorber (c) and dipole magnet vacuum chamber, hosting a SIP55 with Penning gauge and pumping port. A photon mask with SIP75 (d) is installed upstream of beam shutter and topper (e), and SIP500 pumps close by. The achromat vacuum system is symmetric with respect to the middle of the short straight section (f), where a short ID or an RF cavity could be installed.

9.3. Sectioning valve mask

A sectioning valve is installed in each short straight section in the middle of the achromat, where short IDs or RF cavities will be installed, to possibly manage the vacuum level independently in the two sections. The valves are custom-made devices with RF shielding and numerous internal components, which alltogether contribute to out-gassing and therefore to the increase of the local pressure. SynRad + simulations reveal that, in spite of NEG-coating of upstream and downstream chambers, the low conductance of the short straight chamber limits the effective pumping speed across the valve area. To mitigate this problem, a short mask will be installed in front of the valve, to introduce a gradual transition from the rhomboidal shape of the upstream chamber, see Fig. 32. The mask shields the valve components from reflected radiation. Doing so, it avoids the production of hotspots, and it eventually reduces the pressure level. Preliminary estimations confirm that the mask does not contribute significantly to the overall machine impedance.

9.4. Dipole magnet photon absorber

Photon absorbers have to deal with a high thermal load from synchrotron radiation. The way the radiation is absorbed and/or reflected by the absorber greatly affects the vacuum conditions in the surrounding chambers. A saw-tooth absorbing edge at a grazing angle was found to perform well in terms of thermal load, but it also produces relatively important reflections and hot spots on internal walls, where the higher photon-induced desoprtion yeld tends to locally increase the pressure. Thus, the original design by ESRF-EBS [48] was modified with shield walls to significantly reduce the amount of reflected radiation.

The one-jawed, toothed profile of the dipole magnet (B80) absorber was conceived to reduce high power densities collected at short distance from the upstream dipole magnet, which is only 0.4 m in Elettra 2.0. The spatial power density (SPD) maximum is 620 W/mm^2 at normal incidence, depositing 2 kW on the absorber (in Elettra, the same power is deposited with ~10 times smaller SPD). The triangular teeth shape of the absorber surface, sketched in Fig. 33, is intended to cope with the high SPD. This is reduced by a factor $\sin(\beta)\sin(\alpha)$ with respect to a flat surface, where 2β is the angle at the top of the teeth, and α is the teeth pitch relative to the bending plane. The angle α is the main contributor to the SPD reduction. Low values of β create acuminate teeth, which is less efficient in transporting heat from the tip to the bottom of the surface, hence is more subject to hot spots.

Thermo-mechanical and fluid dynamic simulations were done with the ANSYS code to validate the preliminary design, and were supported by comprehensive Monte Carlo ray-tracing simulations to evaluate photon reflections. The angle β, radius r and tooth height h, all shown in Fig. 33, were selected using a NSGA-II [53] optimization algorithm, the objective of which was to minimize the thermal and mechanical stresses, using a robust approach, which took into account extreme, but still realistic misalignments (± 1 mm, ± 2 deg) and beam mishandling. The angle $\alpha = 8$ deg was thus chosen, together with the other geometric parameters in Table 15.

The final dipole magnet absorber design for Elettra 2.0 is illustrated in Fig. 34. It is designed in such a way it can be inserted into the vacuum chamber from the inner side of the storage ring. This design allows for better sighting of the alignment fiduciaries, offering larger angles of vision to the laser tracker. The absorber features a cut-out in the shape of the vacuum chamber to avoid any interference with the electron beam, and to maintain continuity of the inner wall along the beam path.

To tackle the reflections due to the relatively small α angle, a secondary, screw-on, bent copper sheet is used. This add-on retains ease of manufacturing of the absorber main body via electrical discharge machining (W-EDM [54]). The copper sheet is angled by 45° to deflect eventual further reflections towards the absorber body. Even though the surface contact between the absorber body and the add-on is small, it is sufficient to dissipate the small reflected power.

The absorber dissipates heat through two cylindric, blind cooling channels situated below the absorber jaw. The cooling channel adopts many of the geometric considerations in Ref. [48]: two 8 mm-diameter blind holes, each one containing a concentric 6 mm-diameter tube. Blind
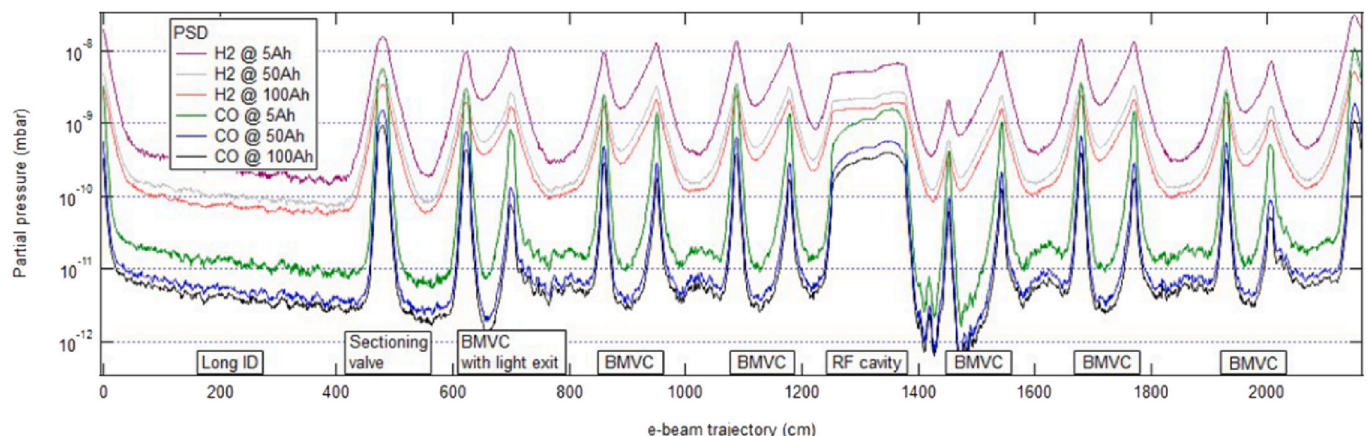

Fig. 30. PSD contribution of CO and H_2 to the total pressure after 5Ah, 50 Ah and 100 Ah of conditioning time.
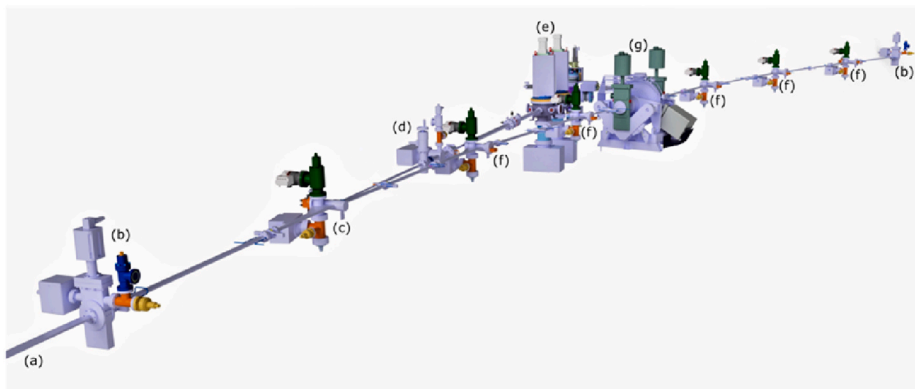
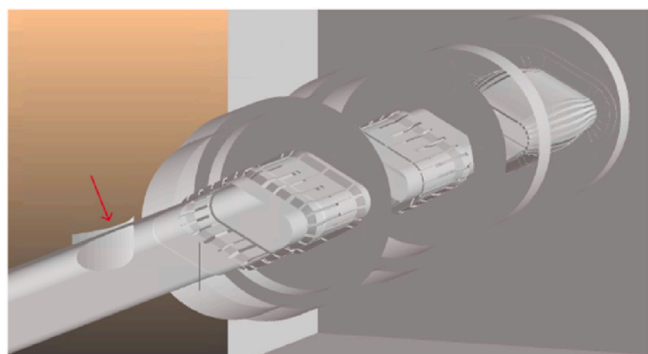**Fig. 31.** Vacuum components of one arc of Elettra 2.0.

Fig. 32. SynRad+ 3-D model of the radiation mask (red arrow) to protect RF bellows and section valve, in the short straight section.
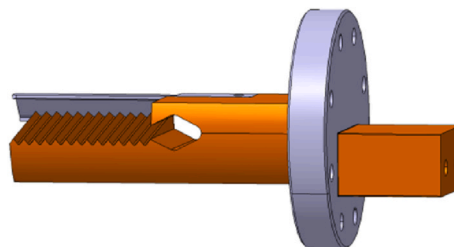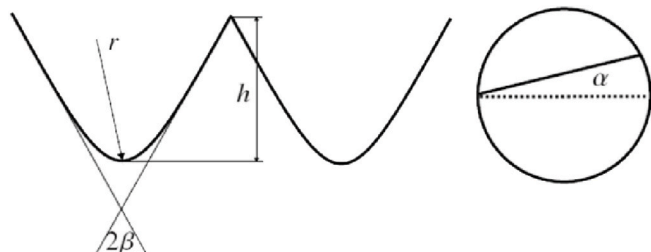

Fig. 33. Geometric parameters of the dipole magnet B80 photon absorber.

Table 15
Absorber optimized parameters.

Parameter [Units]	Symbol	Value	Units
Teeth top angle	2β	72	deg
Foot radius	R	0.92	mm
Teeth height	H	2.84	mm
Main surface pitch	α	8	deg

holes avoid brazing in contact with the vacuum chambers, and so avoid the risk of a failure and consequent vacuum contamination with the coolant. The coolant inflow is through the outside annulus; the outflow is through the inner cannula. A volumetric flow of 0.044 l/s has been chosen. The smaller area of the inner tube increases the speed of the coolant return but, given the choice of steel walls, no velocity-induced erosion is foreseen.

The inner tube is kept centred by means of an outer helix that acts both as a support and a turbulence promoter. The 20 mm-helix pitch has been chosen to maximize the heat transfer coefficient in comparison

Fig. 34. Elettra 2.0 dipole magnet absorber.

with the bare annulus, while keeping the pressure drop below 0.7 bar (see Fig. 35). The cooling channels will be fed in parallel by tubing coming from the girder distributor, with dedicated return valves and flow meters to regulate and monitor the coolant flow.

Ray-tracing in SynRad+ was used to determine the SPD and therefore the temperature distribution. The maximum thermal load on the absorber's teeth amounts to 78 W/mm^2, for a total heat load of 2 kW. The thermal and mechanical simulations were done with ANSYS Mechanical [56]. A prudent constant heat transfer coefficient of 20 kW m^{-2} K^{-1} was assumed, giving a maximum temperature of 231 °C and 238 °C for ideal beam orbit and in the presence of angular and spatial misalignment, respectively (see Fig. 36-top). The worst value of the first principal stress parameter, evaluated across the tested configurations, is $\sigma_1 = 160$ MPa. The maximum value of the third principal stress parameter is $\sigma_3 = 260$ MPa. Both satisfy the stress criterion: $|\sigma_{max}| < 280$ MPa. The maximum value of the shear is $\tau = 130$ MPa, where the specification is < 140 MPa. Fig. 36-bottom illustrates the stress analysis.

SynRad simulations predict that less than 3 % of the incident radiation is reflected back into the electron channel, mainly due to the grazing incidence of light on the vertical half-tooth face. Assuming a thermal gap conductance of 10^{-3} kW m^{-2} K^{-1}, the reflection shield reaches the maximum temperature of 141 °C, while absorbing 56 W.

10. Main RF system

With the maximum single particle energy loss of 670 keV per turn via synchrotron radiation, and 400 mA stored average current, the average beam power amounts to 268 kW. The momentum acceptance of Elettra 2.0, in excess of 3 %, specifies a total peak voltage of 2 MV at 2.4 GeV. Four independent and identical RF plants fulfil the Elettra 2.0 specifications. In the first phase of operation, the four RF cavities presently in use in Elettra will be adopted for use in Elettra 2.0 as well.

The design of the RF system for the Elettra 2.0 [57] relies on solid state transistors as RF power sources. Present sources easily provide more than 100 kW of output power at 500 MHz. Each RF plant can be represented as in Fig. 37. All the blocks in the diagram will be upgraded
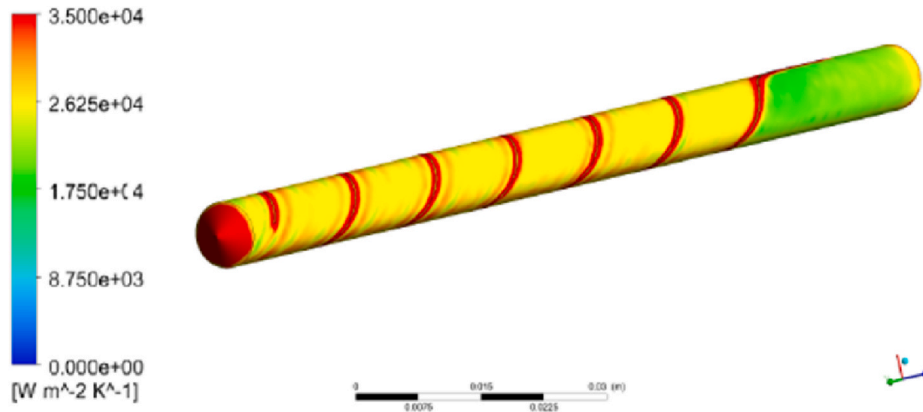
Fig. 35. Cooling channel of the dipole magnet absorber. ANSYS FLUENT [55] was used to calculate the heat transfer coefficient, whose average value results 28 kW m^{-2} K^{-1}.
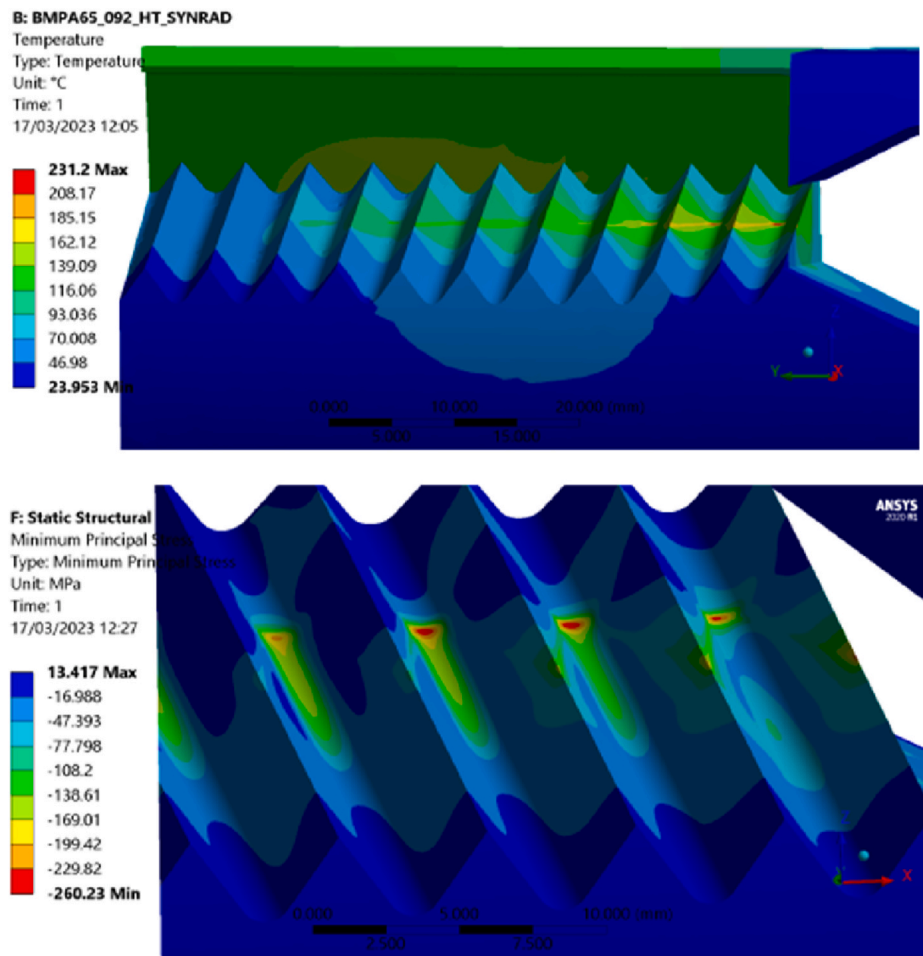

Fig. 36. Top, temperature distribution along the absorber. Bottom, third principal stress analysis results.

with the exception of the accelerating cavity.

The existing "*Elettra type*" cavity will be re-used, achieving a good compromise between cost saving and attainable performance. The amplifier and the RF power run and passive high RF power components must be brand new due to the RF power increase. The Digital Low Level RF and the dedicated local fast interlock will be designed according to the state of the art of the digital electronics. The master oscillator and the low power RF signal distribution will also be recycled. The "Elettra type" cavity has operated more than 28 years; its performance and

reliability are well known. Table 16 shows the requested and attainable parameters for the Elettra 2. 0 storage ring.

The Elettra cavity is not equipped with any dedicated High Order Modes (HOMs) dampers. Transverse and longitudinal instabilities and beam losses can occur when the beam spectrum overlaps the HOMs frequency spectrum. Currently, the Elettra storage ring beam quality and stability is achieved by shifting the cavity's HOMs spectrum by changing the cavity volume by means of a movable plunger and temperature control. This shift avoids any dangerous interaction between the beam
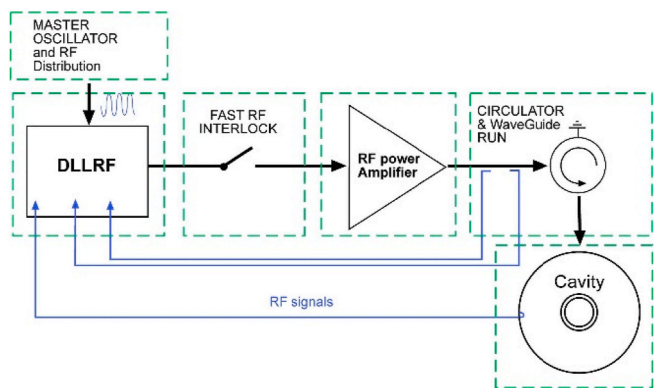
Fig. 37. Schematic blocks of the RF plant.

Fig. 38. 130 kW 500 MHz solid state amplifier.

Table 16
RF cavity parameters.

Parameter for one cavity	Specified	Reachable
Accelerating Voltage (keV)	500	575
Losses (kW)	38	50
Power to the Beam (kW)	67	67
Total power (kW)	105	117
Coupling Factor	2.77	2.34
Overvoltage Factor	2.99	3.43
RF Acceptance (%)	3.5	4
Synchrotron Freq. (kHz)	2.94	3.18
Robinson limit current (mA)	460	490

and HOMs spectrum. The same strategy has been considered for Elettra 2.0, taking in to account the 60 % increase of the average current at the 2.4 GeV operating energy. Results are promising and the frequency shift required for Elettra 2.0 lies in the same range of that needed for Elettra. Still, the 3HC and the bunch-by-bunch longitudinal feedback system, in operation today in Elettra, are mandatory tools to suppress any residual coupled-bunch instability in Elettra 2.0.

Following the Italian public procurement tender procedure, a contract was awarded to Cryoelectra for the procurement of four identical transmitters based on Solid State Amplifier technology (SSA) running 130 kW in continuous wave (CW) mode at 500 MHz. The contract was signed in June 2019, and the SAT and the installation of the first SSA in Elettra occurred in October 2021. Each RF pallet board, composed of a single transistor and its insulating circulator, sits directly on the $\lambda/4$ coaxial combiner, thereby reducing the need for flexible cables and improving the efficiency of recombination. Sixteen RF pallets are combined in a high power-module unit. The module was tested up to more than 10 kW with a measured efficiency greater than 60 %. The SSA achieves 130 kW by combining fifteen high RF power modules. One of the four SSA installed in the Elettra service area is shown in Fig. 38.

The SSA were commissioned and set into operation with the accelerating cavities. The installation was fully transparent to the Elettra's users. By now, the first SSA installed has accumulated more than 3700 h of operation at 50 kW CW with no failure. The SSA has overcome a 66-h non-stop duration test at 130 kW CW with no troubles, the measured wall-plug efficiency at nominal power is 52 % but it drops at lower RF power level if the transistor drain voltage is kept constant. Gain stability is in the same range measurement uncertainty of the R&S NRP-Z81 power sensor. The redundancy test has been carried out with some power supplies and RF pallet boards in "off" state lasting 4 h with no trouble at 130 kW thanks to the very good headroom incorporated into the design.

11. Transient beam loading

One of the concerns about beam stability in Elettra 2.0 is the effect of 3HC on the stored beam due to the presence of a dark gap in the beam filling pattern (hybrid). This gap will be adopted to avoid an ion trapping instability.

A simulator based on an analytical frequency-domain model was developed to evaluate the variation of the synchronous phase and synchrotron frequency along the bunch train, as well as the distortion of the bunch profile. Experiments have been carried out in Elettra to characterize the harmonic cavity and to measure the effect of transient beam loading by using the longitudinal multi-bunch feedback system.

Generally speaking, the beam loading is the voltage induced by the beam in a cavity at the frequency of the bunch. In a gap where RF buckets are not filled, the voltage in the cavity freely oscillates at its own resonant frequency. This transient generates a periodic modulation of the cavity voltage, with a period equal to the revolution time, resulting in a different total voltage seen by the bunches, depending on their position along the bunch train. As a result, the synchronous phase, synchrotron frequency, charge profile and lifetime of each bunch change along the train. This effect can be generally tolerated by finding proper conditions (gap duration and 3HC detuning) to provide the nominal bunch lengthening while minimizing the disruptive effects.

An additional aspect must be considered for Elettra 2.0, which is different from Elettra. A new longitudinal bunch-by-bunch feedback kicker will be working at the fourth harmonic of the main RF, instead of the present third harmonic. This choice makes the feedback more effective but, presumably, also more sensitive to non-uniform bunch synchronous phase along the train.

11.1. Frequency-domain simulator

Comprehensive accelerator simulators based on tracking of particles – such as elegant or *mbtrack2* – can be used to study the transient beam loading, as well as simpler tracking codes based on analytic time-domain models [58,59]. More recently, analytical methods to obtain the equilibrium longitudinal bunch density distribution through self-consistent equations have been adopted [60,61]. At Elettra, a simple Matlab simulator has been developed based on an analytical frequency-domain model of the beam, main RF and 3HC, which arrives at a stable, self-consistent solution by means of a rapidly converging iterative process.

The beam can be modelled by the "complex beam current" $\bar{I}$, i.e., an array of complex values, each value representing one of the bunches in a train. The module of each value is the bunch current and the phase is the bunch synchronous phase. The complex current can be expressed as $\bar{I}(i) = I_b(i)\,\bar{F}(i)$, where I_b is the bunch current, $\bar{F}$ is the complex form

factor and i is the bunch index. $\overline{F}$ is given by the following equations:

$$\overline{F}(i) = \frac{\mathscr{F}(\Psi_i)(3\omega_{RF})}{\mathscr{F}(\Psi_i)(0)} = \frac{\displaystyle\int_{-\pi}^{\pi} \Psi_i(\varphi)\, e^{-j3\varphi}\,\mathrm{d}\varphi}{\displaystyle\int_{-\pi}^{\pi} \Psi_i(\varphi)\,\mathrm{d}\varphi} \qquad (2)$$

where φ is the longitudinal coordinate (phase at RF frequency) and $\mathscr{F}$ is the Fourier Transform of the bunch charge density Ψ, which is evaluated at the third harmonic of the main RF. The Fourier Transform of the 3HC voltage induced by the beam can be calculated as the product of the Fourier Transform of the complex current times the harmonic cavity transfer function: $V_{3HC}(\omega) = \mathscr{F}(\bar{I})(\omega)\,H_{3HC}(\omega)$. Module and phase of $H_{3HC}(\omega)$ can be calculated with the following expressions [62]:

$$|H_{3HC}| = \frac{R_s}{Q}\,\frac{\omega_{3HC}}{\omega_{3HC}-\omega}\,\mathrm{sin\,atan}\left(\frac{2Q(\omega_{3HC}-\omega)}{\omega_{3HC}}\right) \qquad (3)$$

$$arg(H_{3HC}) = \mathrm{atan}\left(\frac{2Q(\omega_{3HC}-\omega)}{\omega_{3HC}}\right)$$

where R_s, Q and ω_{3HC} are, respectively, the shunt impedance, the quality factor and the frequency of the harmonic cavity.

After the 3HC voltage seen by each bunch is calculated through the Inverse Fourier Transform of $V_{3HC}(\omega)$, the total voltage seen by the beam can be evaluated, as well as the potential:

$$V_{tot}(\varphi) = V_{RF}\sin(\varphi+\varphi_s) + V_{3HC}\sin(3\varphi+\varphi_{3HC})$$

$$U(\varphi) = -\frac{c\,\alpha_c}{EC\omega_{RF}}\int_0^{\varphi}(eV_{tot}(\varphi') - U_0)\mathrm{d}\varphi' \qquad (4)$$

with V_{RF} the peak RF voltage, φ_s the synchronous phase, α_c the (linear) momentum compaction factor, c the light speed in vacuum, E the beam energy, C the reference orbit length, e the electron charge and U_0 the single particle's energy loss per turn.

$U(\varphi)$ is eventually used to determine the charge distribution:

$$\Psi(\varphi) = \frac{e^{-\frac{U(\varphi)}{\alpha_c^2\sigma_E^2}}}{\displaystyle\int_{-\pi}^{\pi} e^{-\frac{U(\varphi)}{\alpha_c^2\sigma_E^2}}d\varphi} \qquad (5)$$

where σ_E is the absolute energy spread. By means of Ψ, the new values of the bunch form factor are calculated and a new iteration can start.

The equilibrium bunch charge distribution is obtained by iterating the computation until a consistent stable solution is found, i.e., the difference between two consecutive iterations is negligible. To assure convergence of the iterations, only a fraction of the difference form factor is applied at each step; the complete convergence is normally obtained in 50–100 iterations, namely, in a few seconds. Finally, the equilibrium bunch charge distribution gives access to all other relevant parameters, such as stable synchronous phase, bunch length and Touschek lifetime. The synchrotron frequency is determined analytically from the longitudinal gradient of the total voltage seen by each bunch.

It is worth noticing that the main RF accelerating cavities are modelled, altogether, as an additional passive cavity with its own specific shunt impedance and quality factor, and whose peak voltage is fixed to the total nominal value of the real active elements.

11.2. Comparison of codes and experimental results

To validate the simulator's predictions, they have been compared with measurements carried out at Elettra and with results from the well-established code *mbtrack2*. Fig. 39 shows the transient beam loading
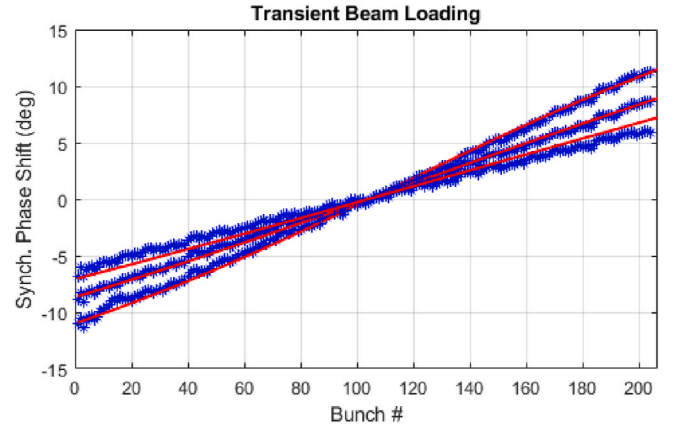

Fig. 39. Synchronous phase shift along the bunch train in Elettra; simulation (red) and experimental data (blue), with E = 2.0 GeV, I_b = ~200 mA, 50 % filling pattern and three different detuning values 45, 60 and 70 kHz.

measured in Elettra by means of the longitudinal multi-bunch feedback system, and compared to the semi-analytical predictions. The inclusion of the main RF cavities in the model was essential to reach the agreement, since they appear to contribute substantially to the overall transient beam loading.

Fig. 40 shows an example of comparison of the Matlab simulator with *mbtrack2*, applied to the model of Elettra 2.0, i.e., 2.4 GeV beam energy, 400 mA total average current in 93 % filling pattern, and 70 kHz detuning of 3HC.

One of the possible scenarios for Elettra 2.0 is the operation with RF transverse deflecting cavities (also "crab cavities" in the literature) to produce short photon pulses by transversally tilting one single bunch and downstream selecting a short portion of the emitted light pulse. This technique will require a specific hybrid filling pattern with a bunch train filled one every two buckets and one bunch per dark gap. The bunch average current, both in the train and in the gap, shall be 2 mA to guarantee a total nominal current of 400 mA.

Since the simulator is able to model any arbitrary filling pattern, the impact of transient beam loading was predicted also for the specific configuration using crab cavities. For example, Fig. 41 shows the results of the simulator for a dark gap of 80 ns and a total current of 394 mA; four values of detuning of 3HC, from 80 to 95 kHz, have been considered. Special attention has to be paid to the distortion of the tilted bunch current profile, in order not to compromise the quality of the short photon pulses. It becomes evident that, due to the combination of the phase variation of 3HC and the high value of its voltage along the gap, the effect of bunch lengthening could be higher in the middle of the gap than in the bunch train. The current profile gets distorted, with the creation of two separated bunches (overstretching), while all bunches in the train remain substantially Gaussian.

A trade-off between benefits of 3HC in terms of lifetime increase and negative effects from transient beam loading shall be adopted for this particular operating mode, such as the one corresponding to the yellow curves in the figure.

12. Impedance model and instabilities

Primarily due to the reduced diameters of the vacuum chambers and of the other equipment, the performance of the next-generation light sources can be greatly degraded by the insurgence of beam instabilities, resulting in a reduction of the intensity in both single and multi-bunch operation. The effect of the resistive wall and geometric broadband impedance on the single-bunch microwave instability and the multi-bunch transverse mode coupling instability has been investigated in Elettra 2.0, using both analytical methods and particle tracking. In that way, current thresholds and therefore the range of beam parameters
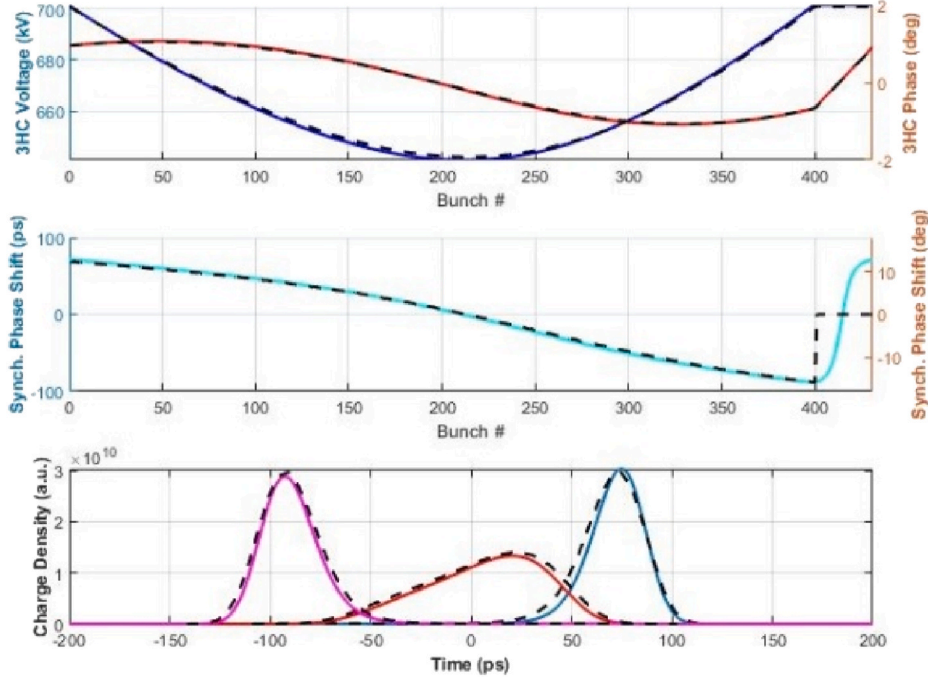
Fig. 40. Comparison of the Matlab simulator (solid lines) and *mbtrack2* (dashed lines) for Elettra 2.0: 3HC voltage/phase (top), synchronous phase shift along the bunch train (middle), and charge profile of the first/middle/last bunch (blue/red/magenta).

ensuring stable motion have been identified.

12.1. Broadband impedance

The main sources of broadband impedance include the resistive wall impedance and diffraction impedances, i.e., impedance due to discontinuity of the geometry of the vacuum chamber, such as transitions and tapers, bellows, BPMs, striplines, flanges, and ante-chambers.

A first-order approach to the broadband impedance budget for Elettra 2.0 was carried out using well-known analytical formulas. They had been successfully benchmarked in Elettra in the past [64], and will be subject of further treatment through CST simulations [65].

The Elettra 2.0 vacuum chamber is rhomboidal with an internal dimension of 27 × 17 mm, and made of copper (45 %), aluminium (20 %), and stainless steel (35 %). Also, most parts of the chamber have NEG coating, as discussed in the previous Section. By approximating the rhomboidal geometry by a smooth transverse profile, the longitudinal and transverse resistive wall impedance can be estimated as follows [66]:

$$\frac{Z_l^{RW}}{n} = Z_0 \frac{(1+i)}{2} \frac{\delta}{b} \frac{L}{2\pi R} \tag{6}$$

$$Z_t^{RW} = Z_0(1+i) \frac{\delta}{b^3} \frac{L}{2\pi}$$

where b is the chamber radius, δ the skin depth characteristic of the material, Z_0 is the free space impedance, and L is the length of the chamber.

The geometric impedance of transitions results in:

$$\frac{Z_l}{n} = iZ_0 \frac{\omega_0 \, tan \, \theta}{4\pi c}(d - b) \tag{7}$$

$$Z_t = \frac{-iZ_0}{2\pi b^2}\theta^2 L$$

where ω0 is the revolution frequency, b and d are the vertical full sizes at the transition edges and θ is the angle of the slope. The most contributing

transitions are those close to the four RF cavities and those of three of the insertion devices.

All bellows of Elettra 2.0 will be shielded. So, for any given length l and half-aperture w, the bellows contribute to the broadband impedance only through the openings between the "RF fingers". The following formula can estimate openings of pumping elements or radiation extraction ports:

$$\frac{Z_l}{n} = -i \frac{Z_0 \omega_0}{4\pi^2 cb^2}w^2 \left(0.1814 - 0.0344\frac{w}{l}\right) \tag{8}$$

$$Z_t = -i\frac{Z_0}{\pi^2 b^4}w^2 \left(0.1814 - 0.0344\frac{w}{l}\right)$$

The longitudinal impedance of the BPM button can be calculated according to:

$$\frac{Z_l}{n} = i\frac{2Z_c r_b}{R}\left(\frac{\theta}{\pi}\right) \tag{9}$$

where Zc = 11 Ω, rb = 3.5 mm is the button radius, and θ = rb/b the effective semi-angular aperture, with b the chamber radius.

The geometric impedance of gaskets should also be carefully considered because of their large number (288). For one gasket, the longitudinal impedance is:

$$\frac{Z_l}{n} = \frac{Z_0 g d}{\pi b^3} \tag{10}$$

where g is the gap length in the flange and d is the difference between the chamber and the gasket radius. Clearly, the flange gap should be as small as possible. A design is in progress for Elettra 2.0 that ensures g < 0.1 mm.

As for HOMs in the main RF cavities, we can write:

$$\frac{Z_l}{n} = i\omega_0 \sum R_s^k \Big/ \left(Q_k \omega_R^k\right) \tag{11}$$

A full characterization of HOMs in the Elettra RF cavities has been available for many years [67]. It will be used to estimate the HOMs contribution to the broadband impedance. Table 17 lists the broadband
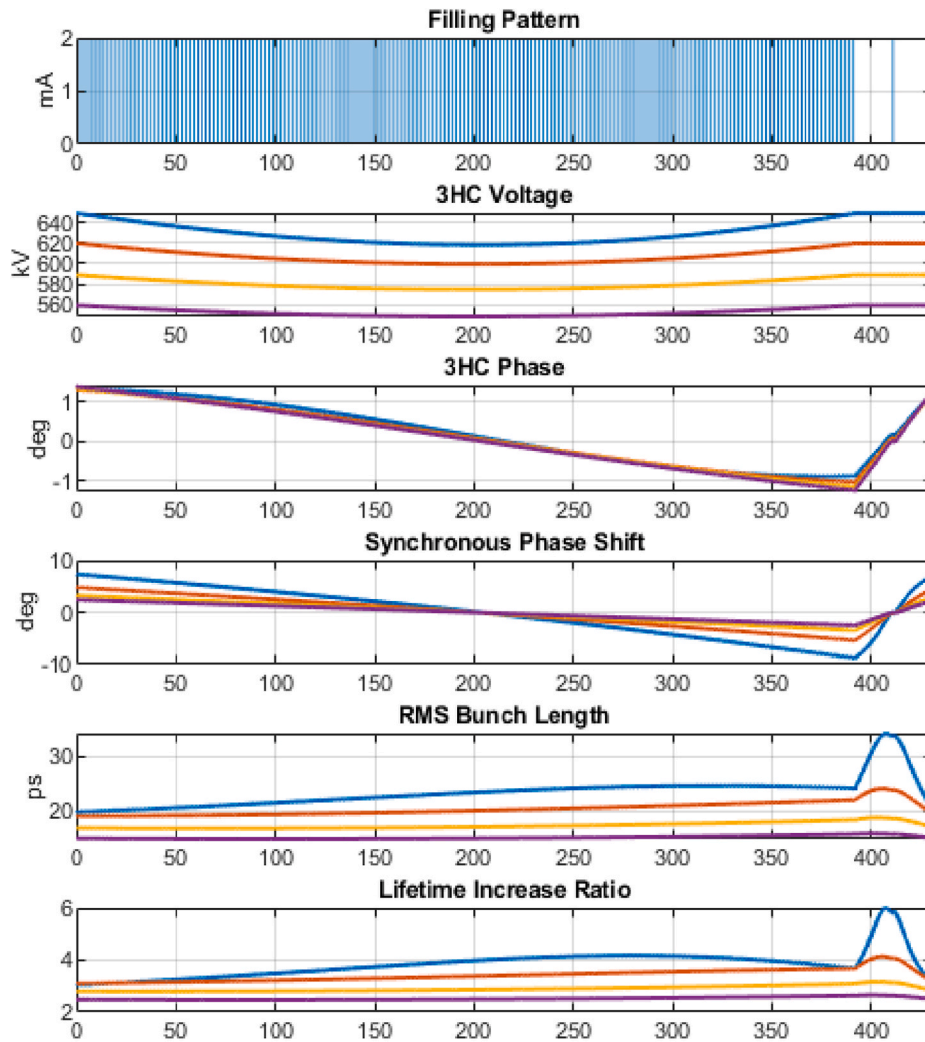
Fig. 41. Results of the Matlab simulator with a hybrid filling pattern in Elettra 2.0: 3HC voltage/phase and bunch characteristics with detuning of 80/85/90/95 kHz (blue/orange/yellow/purple).

Table 17
Impedance budget of Elettra 2.0

	Re($\frac{Z_l}{n}$) [Ω]	Im($\frac{Z_l}{n}$) [Ω]	Re(Z_t) [kΩ/m]	Im(Z_t) [kΩ/m]
Resistive wall	0.29	0.24	98	98
Transitions		0.087		90
Bellows, slots, openings		0.07		88
BPM gaskets		0.09		79
RF HOMs		0.25		159
Total	0.29	0.74	98	514

impedance budget of Elettra 2.0 based on the aforementioned analytical estimations and available HOMs data. The loss factor including the effect of the 3rd harmonic cavity at 400 mA is 20.2 V/pC, corresponding to a power loss of 7 kW that additionally must be provided by the RF system. The kick factor is 4.4 kV/pC/m, about 40 % higher than that of the present machine.

12.2. Geometric impedance of flanges

The problem of the impedance associated to the joints between different sections of the vacuum chamber has been addressed in the literature, such as for the CERN SPS, in which RF contacts have been adopted [68], and for SLS 2.0 at PSI, where zero-gap flanges were chosen [69].

Two types of flanges have been considered for Elettra 2.0, the Spigot Flange Lip (SFL) and the Spigot Flange Planar (SFP), see Fig. 42. The two mainly differ in the uniformity of the gap between the opposite sides of
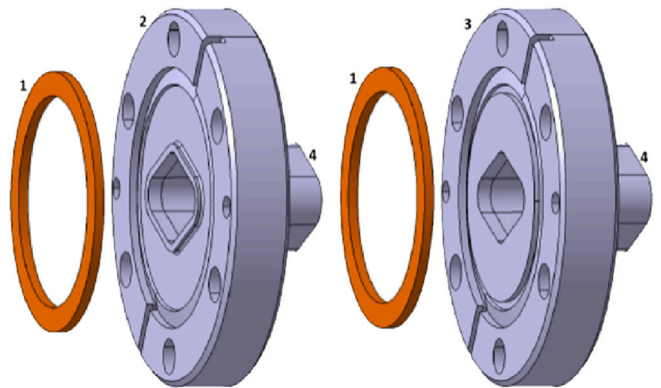

Fig. 42. Mechanical drawing of the Spigot Flange Lip (2) and of the Spigot Flange Planar (3). The gasket (1) and the rhomboidal vacuum chamber of Elettra 2.0 (4) are also shown.

the vacuum joint: in the SFP, this gap is nominally uniform up to the gasket housing. A comparative numerical analysis which takes in to account different aperture gaps between the flanges [70] has been conducted to point out any criticality of small impedance contributions which, added together in large number, shall be lower than any specified impedance threshold, or correspond to any equivalent threshold in stored beam current.

A simplified electromagnetic model was extracted from the mechanical drawing. Table 18 lists the geometric parameters of the flanges. The model includes surfaces, volumes and materials interacting with the electromagnetic field induced by the accelerated charges. Two sets of electromagnetic simulations were performed with CST Particle Studio: the first one to evaluate and compare the longitudinal impedance assuming the nominal geometry of the flanges, the second one to evaluate the effect of construction tolerances and variation of parameters.

A numerical analysis of the output of the simulation tool allows evaluation of both the broadband and the narrowband impedance. The main resonant mode of the latter impedance is listed in Table 19 for the two flanges. Then, the normalized longitudinal impedance is calculated (see Fig. 43) and, from that, the loss factor. In conclusion, the real part of the SFL is ~100 times larger than that of the SFP, while the loss factor is approximately 4 times larger.

12.3. Microwave instability

The well-known Boussard-Keil-Schnell criterion sets the current threshold for the bunched beam microwave instability [71]:

$$\left|\frac{Z_l}{n}\right| < 2\pi \frac{E/e}{I_b} \alpha_c \sigma_\delta^2 \qquad (12)$$

or equivalently

$$\left|\frac{Z_l^{eff}}{n}\right| \leq \frac{8\,ln\,2}{2\pi} \frac{hV_{rf}\,cos(\varphi_s)}{\sqrt{2\pi}I_b}\left(\frac{\sigma_z}{R}\right)^3 \qquad (13)$$

in which Ib is the single bunch peak current, σ_z the bunch length, R the dipole curvature radius, h the harmonic number, and φ_s the synchronous phase. The analytical estimate of the broadband impedance budget in Table 17 was integrated to obtain the total impedance of the SFP flanges, as given in Table 19. Then, Eq. (12) provides the single bunch current threshold of ~3 mA, assuming bunch lengthening by a factor >2 from 3HC, i.e., $\sigma_z > 3$ mm.

This result was benchmarked with particle tracking, in the simplified picture of a rhomboidal vacuum chamber everywhere along the ring, and investigating different materials. First, the resistive wall impedance in the presence of NEG coating was calculated by means of IW2D [72]. In this case, the chamber is assumed to be composed of different materials as specified in the previous section. Second, an effective geometric broadband impedance according to the estimate in Table 17 was defined. Both impedances were imported in elegant and particle tracked for approximately 3 damping times. The instability onset is identified by the change of slope of the beam energy spread with increasing single bunch average current; see Fig. 44. That procedure yields a threshold of approximately 3 mA, in agreement with the analytic estimate.

For a chamber made entirely of copper, copper without NEG, or aluminium, the current threshold becomes, respectively, 4 mA, 4.5 mA and 2.5 mA, respectively (not shown). elegant simulations were benchmarked with *mbtrack2*. In the case of nominal chamber

Table 18
SFL and SFP geometric parameters.

Parameter	Value	Unit
Gap (G)	0.1	mm
Cavity depth (C)	2.4	mm
Length	20	mm
Gasket inner radius	19.6	mm

Table 19
SFL and SFP narrowband impedance and loss factor.

Flange	SFL	SFP	Unit
Frequency	2.9388	4.8793	GHz
Shunt impedance	1247.7	22.64	Ω
Quality factor	287	56	
Re(Z_l/n)	0.4914	0.0054	Ω
Loss factor	0.0483	0.0131	V/pC

composition but without NEG, *mbtrack2* predicted a current threshold around 4.5 mA, in agreement with the aforementioned results.

12.4. Transverse mode coupling instability

The effect of the resistive wall impedance in terms of so-called multibunch transverse mode coupling instability was investigated versus linear chromaticity. Vertical chromaticity, ξ_y, determines a frequency shift of the bunch's spectrum with respect to real part of the longitudinal impedance by $\omega_\xi = \frac{\xi_y \omega_{riv}}{\alpha_c}$. Hence, a far smaller effective impedance is sampled by the stored beam.

We anticipate that, as a result of particle tracking, above a certain chromaticity, the instability threshold current is determined by the radial head-tail modes. In view of mitigating such modes, adopting a transverse bunch-by-bunch feedback system, as well as bunch-lengthening from 3HC, is essential. Only the vertical component of the resistive wall impedance was considered, given the 2.5 aspect ratio of the horizontal-to-vertical diameter of the rhomboidal vacuum chamber. In the frequency domain, the RW-MBI code implementing Laclare's eigenvalues [73] for finding the threshold current was used. This study was complemented by time-domain particle racking runs with elegant.

The complex impedance-driven tune shift for each head-tail mode is retrieved from the RWMBI code according to:

$$\Delta\omega_m\sigma_m\left(\omega_{mq}\right) = \frac{\beta_\perp I_b}{2T_0\frac{E}{e}}\sum_p jZ_\perp\left(\omega_{mp}\right)A_{pq}^m\sigma_m\left(\omega_{mp}\right) \qquad (14)$$

where T$_0$ is the revolution time, $Z_\perp$ is the transverse impedance, $\beta_\perp$ is the average transverse beta function, σ_m is the bunch spectrum and $\Delta\omega_m$ is the complex betatron frequency shift for mode *m*. This shift is calculated as the eigenvalue with the largest positive imaginary component, while σ_m is the eigenvector.

The first study was carried out for weak bunch lengthening induced only by the longitudinal resistive wall impedance (see Fig. 4). The result for mode m = 0 shows that beam current threshold has a local maximum versus chromaticity. In particular, the threshold starts decreasing (stability is for lower currents) for vertical chromaticity larger than 3, as shown in Fig. 45-left plot. This behaviour is explained by the beam spectrum in Fig. 45-right plot. ξ_y= 3 shifts the beam spectrum with respect to the peak of the impedance (this corresponds to the 0-frequency in the plot). However, a larger chromaticity generates multiple peaks in the spectrum, one of which again samples the maximum of the impedance.

A qualitatively similar, but quantitative different, condition is found for 3-fold bunch lengthening, as expected at full current and properly tuned 3HC. Also in this case, the current threshold of different modes converges to the same value for $\xi_y > 5$, see Fig. 46.

As a benchmarking study, the resistive wall transverse wakefield was analytically evaluated for a copper vacuum chamber in the approximation of a round section, and imported into elegant for particle tracking. The effective resistivity of the material is 1.7×10^{-8} Ωm; the radius is set to 7.5 mm. The wakefield can be calculated by means of the Panofsky–Wenzel theorem:
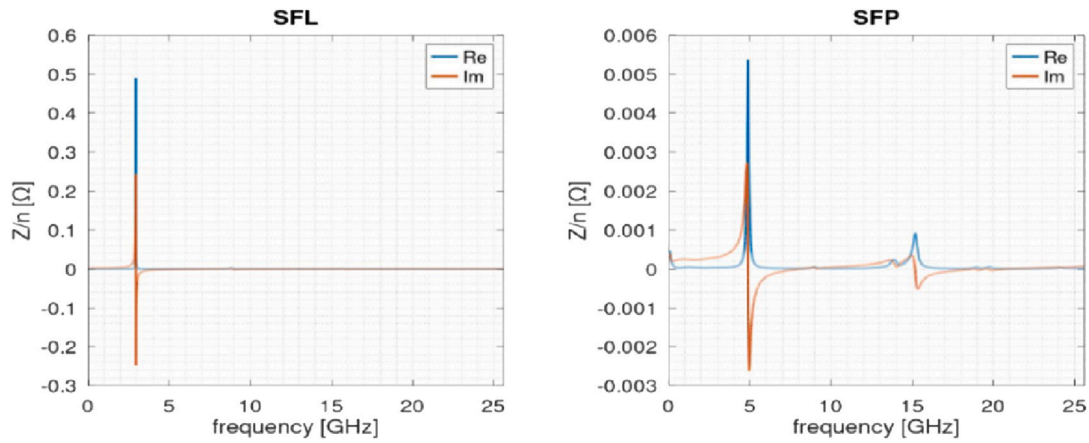
Fig. 43. Normalized longitudinal impedance of SFL and SFP flange.
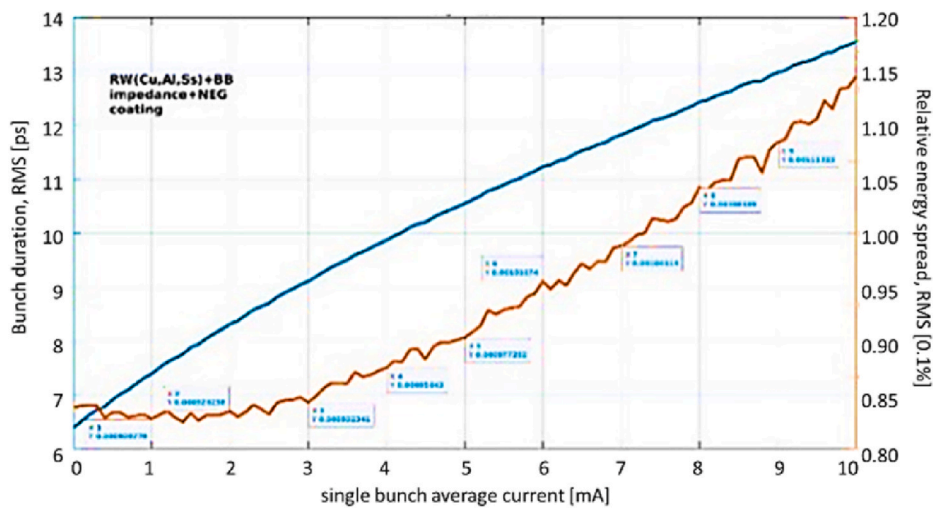

Fig. 44. RMS bunch length (blue) and relative energy spread (orange) vs. single bunch average current, in the presence of resistive wall and geometric broadband impedance. The current threshold is approximately 3 mA.
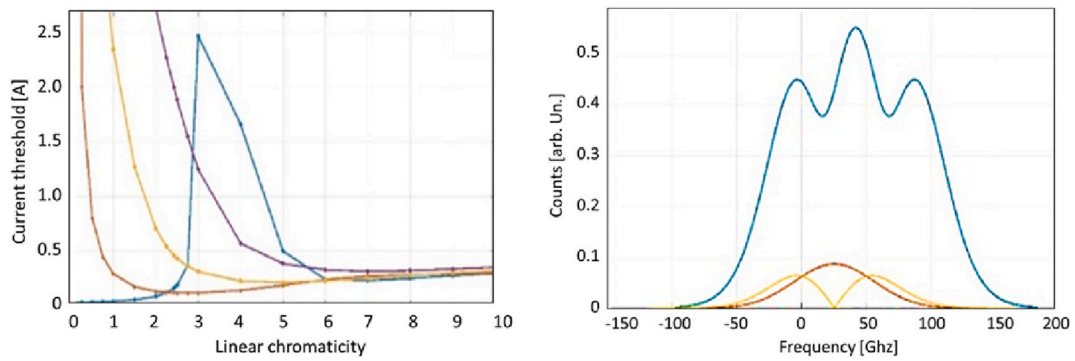

Fig. 45. Left, TMCI-threshold current for different modes (0 = light blue, 1 = orange, 2 = yellow, 3 = violet) versus linear vertical chromaticity, in the presence of vertical resistive wall impedance. Right, bunch spectrum for mode 0 at $\xi_y = 3$ (orange) and $\xi_y = 5$ (light blue), and for mode 1 (yellow).
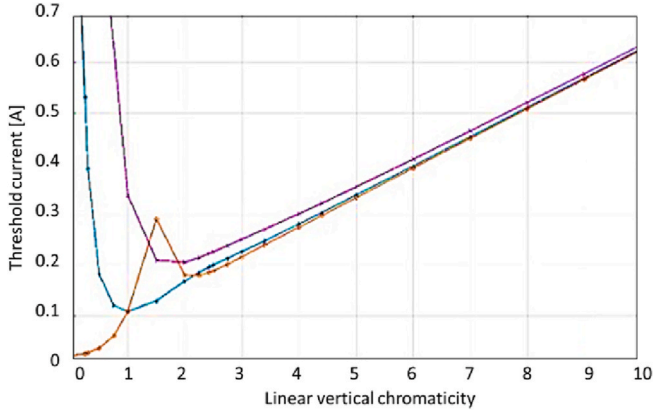
Fig. 46. TMCI-threshold current for different modes (0 = orange, 1 = light blue, 2 = violet) *vs.* linear vertical chromaticity, in the presence of vertical resistive wall impedance and Gaussian 3-fold lengthened bunches.

$$W_{RW}^{Trans}(\tau) = \frac{8Z_0 c}{\pi a^4}\left(\frac{1}{12}\left[-e^{-\tau/\tau_0}\cos\left(\frac{\sqrt{3}\tau}{\tau_0}\right)+\sqrt{3}\,e^{\frac{-\tau}{\tau_0}}\sin\left(\frac{\sqrt{3}\tau}{\tau_0}\right)\right]\right)$$
$$+\frac{8Z_0 c}{\pi a^4}\left(\frac{-\sqrt{2}}{\pi}\int dx\frac{-e^{\frac{-x^2\tau}{\tau_0}}}{x^6+8}\right) \tag{15}$$

and for $\tau \gg \tau_0 = s_0/c$ it can be approximated to:

$$W_{RW}^{Trans}(\tau) \approx \frac{1}{\pi a^3}\sqrt{\frac{Z_0 c}{\sigma\pi\tau^{1/2}}} \tag{16}$$

s_0 is the characteristic distance:

$$s_0 = \left(\frac{2a^2}{Z_0\sigma}\right)^{1/3} \tag{17}$$

with a being the pipe radius and σ the conductivity.

The current threshold is retrieved by observing the motion of the centre of mass of the bunches. The instability growth rate is determined by applying an exponential fit to the amplitude of the centroid versus the number of turns. For any growth rate k, the current threshold in correspondence of each chromaticity is estimated as:

$$I_{th} = \frac{I_b}{k\tau_y} \tag{18}$$

where τ_y is the vertical damping time.

The centroid's vertical amplitude and the linear fit in semi-log scale for 0-corrected chromaticity is in Fig. 47. The resulting threshold is 24 mA. The threshold for higher chromaticity is in Fig. 48, where an optimum value ξ_y= 2.5 guarantees stable motion at 400 mA.
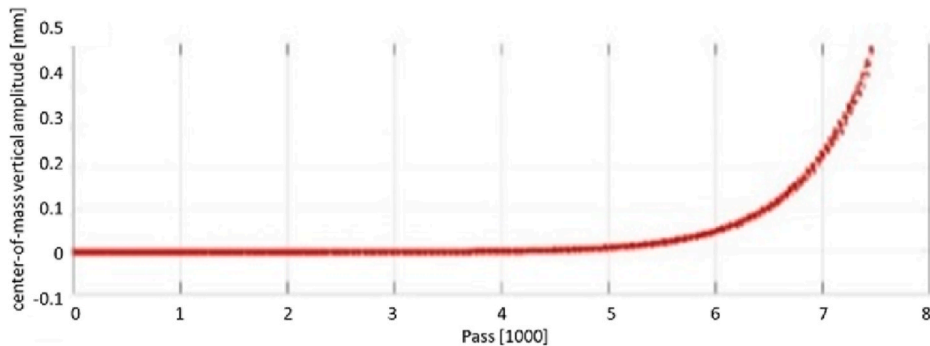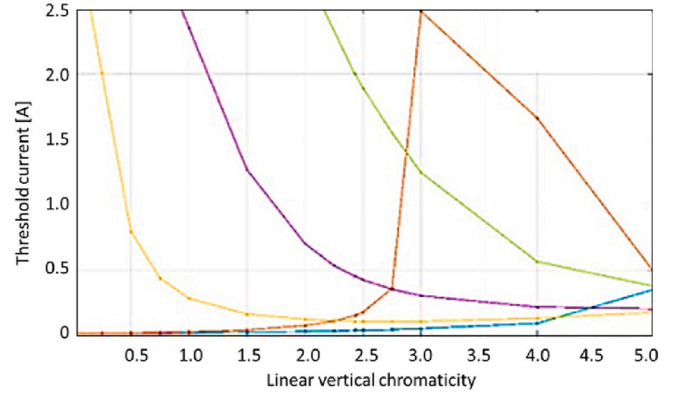

Fig. 48. TMCI current threshold *vs.* vertical chromaticity.

13. Short pulses

The installation of RF transverse deflecting cavities (TDCs) at Elettra 2.0 aims to provide extreme ultra-violet and X-ray pulses of 1–5 ps FWHM pulse duration from IDs, with maximum repetition rate of 1.15 MHz and relative flux at the sample in the range 1–10 % of the standard single bunch emission. Two superconducting RF cavities resonant at a 6-fold (3 GHz) and 6.5-fold frequency (3.25 GHz) of the main RF determine a steady-state configuration of vertically tilted bunches, with varying inclination along the ring circumference. The photon beam emitted by tilted bunches exhibits a vertical-to-longitudinal correlation (t,y). A vertical slit at some distance from the ID samples the central portion of the stretched photon pulse, thus selecting a short portion in time although at a reduced flux [15,74,75].

The choice of RF frequencies of the TDCs in the S-band is motivated by beam dynamics considerations, as a compromise between maximum deflecting voltage and minimum iris radius of the cavities. The use of the S-band range takes advantage of RF power supplies available commercially. The two frequencies satisfy the prescription

$$f_1 = h f_{RF}, f_2 = \frac{hm \pm 1}{m}f_{RF} \tag{19}$$

where f_{RF} is the main RF frequency of approximately 500 MHz, and we have chosen the integers, $h = 6$ and $m = 2$. The latter one implies that the RF buckets containing tilted bunches are alternated with respect to unperturbed buckets: short and long photon pulses can therefore be provided to the beamlines.

In the baseline configuration of Elettra 2.0 with TDCs, the electron beam fill pattern is made of a long train of bunches separated by 4 ns, and a 64 ns-long, dark gap, into which a single ("camshaft") bunch is injected. All bunches have 2 mA average current, to satisfy the specification of 400 mA total current but also to avoid single bunch instabilities. The duration at equilibrium of the tilted bunch in the dark
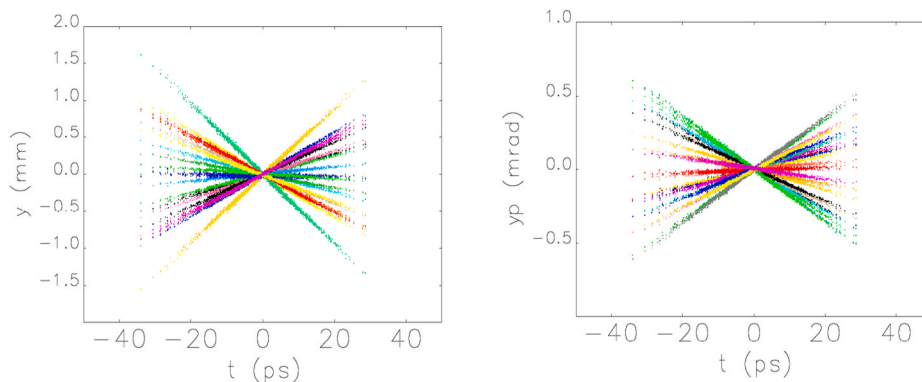

Fig. 47. Vertical TMCI in the from *elegant* runs, for zero chromaticity. The current threshold is 24 mA.

Fig. 49. Tilted electrons' vertical spatial (left) and angular distribution at ID locations along Elettra 2.0, here superimposed for illustration.

gap, as well as the duration of all bunches in the train, is calculated with the semi-analytical tool described in Section 11. The availability of several tuning knobs, such as the 3HC detuning and the position of the camshaft bunch in the gap, on top of a different duration of the gap, allow us to ensure a bunch lengthening factor in the range 2.5–3 for all bunches.

The vertical position of particles and the angular divergence at distance s from the TDCs is proportional to the ratio of peak deflecting voltage and beam energy ($eV_{1,2}/E$), times the coefficient for the angle-to-position and angle-to-angle linear transfer map along the closed orbit. These coefficients are proportional to betatron functions at the TDCs and at the light source point, to the betatron phase advance and the vertical tune. Fig. 49 shows the electron bunch spatial and angular distribution in the (t,y) plane, at several ID locations, as a result of particle tracking with the elegant code [25]. The maximum peak-to-peak vertical extension of bunches is approximately 3 mm, where the minimum gap in Elettra 2.0 will be 5 mm in short in-vacuum IDs.

13.1. Photon beamlines

According to the original proposal [15], the vertically stretched photon pulse can be transported from the ID to a vertical slit either in the front-end area or along the beamline, for production of short durations either with ("imaging") or without ("drift") intermediate vertical focusing elements. In the former case, the slit is applied to correspond to a vertical waist of the light pulse.

From the point of view of the beamline operation, drift optics might be preferred because beamlines commonly foresee double slits or a circular pinhole in the front-end area ("front-end slit"). A front-end slit is primarily used to clean up the incoming radiation, thereby matching the angular divergence of the photon beam to the angular acceptance of the beamline. This is typically in the range 50–200 μrad, in both planes. In Elettra 2.0, the vertical gap of the slit/pinhole will be in the range 0.5–2 mm, whereas the front-end geometry and the existing infrastructure determine a minimum distance of 11 m between ID and front-end slit.

Since imaging cannot be implemented in the tight space of the Elettra 2.0 front-end, an intermediate vertical focusing mirror between the front-end and the sample shall be arranged. Some soft x-ray beamlines include optics vertically focusing on a vertical slit ("entrance slit") followed by a vertically-dispersive monochromator. The spatial (angular) magnification factor of the source is typically around 0.2 (5). With such arrangement, short light pulses can be selected while preserving the energy-resolving power of the monochromator, since the effective source size after slit will be made again small enough in the vertical plane.

If pre-focusing optics and the entrance slit are not available, such as at hard x-ray beamlines, then the monochromator, on which the entire vertically-dispersed light pulse would impinge, should be a horizontally-dispersive one in order to preserve the energy-resolving power. It should

then be followed by vertically-focusing elements and a vertical slit ("exit slit") for selection of the short pulse.

13.2. Short pulse production

The photon distribution is generated with elegant at the ID, and it is geometrically propagated to the vertical slit. For the imaging mode, a vertical focusing mirror with 0.2 magnification is assumed, for the drift/hybrid mode the front-end slit is assumed at 11 m from the ID center. The range of pulse durations after the slit is calculated by scanning the slit half-aperture in the range 5–400 μm for drift optics, and 2–150 μm for imaging optics.

The shortest duration and the corresponding *single pulse relative flux* as function of the pulse duration right at the exit of the slit, for the highest and lowest photon energy of each of the beamlines under consideration, are summarized in Table 20. Such extreme values are obtained for slit half-apertures smaller than 40 μm in drift mode, and smaller than 20 μm in imaging.

The photon pulse duration – reported here and in the following discussion – is the duration of the intensity distribution containing 70 % of the single-pulse photon flux after the slit. Since such a percentage corresponds approximately to the FWHM duration of a Gaussian, we will adopt that nomenclature for the sake of brevity. The relative flux is the number of photons per pulse relative to the total *single* bunch emission, at the same bunch average current. Table 20 points out that the obtainable pulse duration is largely dominated by the intrinsic radiation divergence or, equivalently, the photon energy. In general, imaging optics produces shorter pulses compared to the drift mode, but at the expense of a lower flux.

Table 20

Shortest photon pulse duration and *single pulse* relative flux, at minimum and maximum photon energy of each beamline. Bold values are pulse durations ≤ 4ps FWHM.

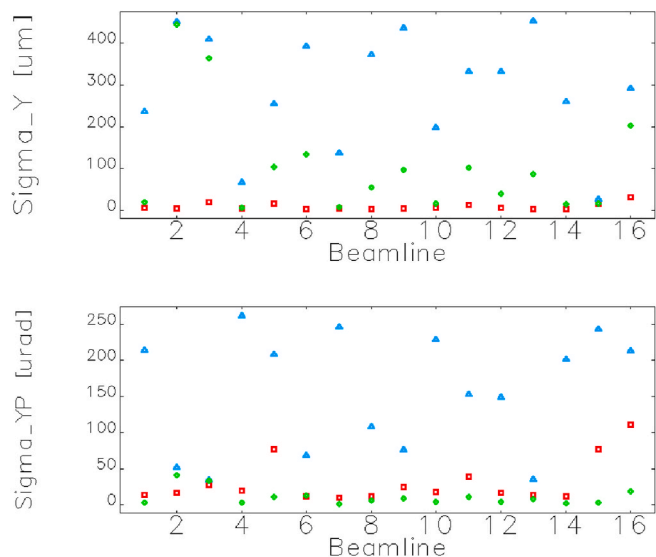| Nr.	Section	Lowest photon energy				Highest photon energy			
		Δt_{FWHM} (ps)		$\Delta F/F$ (%)		Δt_{FWHM} (ps)		$\Delta F/F$ (%)	
		DR	HY	*DR*	*HY*	DR	HY	*DR*	*HY*
1	1.4	4	9	5	*3*	2	3	6	3
2	2.1	15	2	5	3	5	1	8	*2*
3	2.4	6	4	4	5	3	2	2	*2*
4	3.4	13	5	5	8	9	3	20	*2*
5	4.4	6	7	5	10	1	2	2	2
6	5.4	4	1	5	2	5	1	5	1
7	6.4	3	5	5	5	1	2	*1*	*3*
8	7.1	4	8	1	7	2	5	*1*	6
9	7.4	3	1	7	2	3	1	5	*2*
10	8.4	5	5	5	5	2	2	4	2
11	9.4	7	4	20	6	3	2	3	*3*
12	10.4	2	16	3	*13*	2	16	2	15
13	11.1	2	13	3	9	1	5	1	8

Fig. 50. Vertical photon beam size (top) and angular divergence (bottom), evaluated at the ID with TDCs turned off (red) and on (blue). In green, the effective source dimension imaged 1:1 in the presence of a vertical slit for drift mode.

13.3. Effective source

The effective source of the short light pulse is calculated as a 1:1 imaging of the emission at the ID in the presence of the angular selection carried out by the slit. The large reduction of the size and divergence of the *effective light source* as seen by the beamline in the drift mode, for the shortest pulse duration obtained with this scheme, is shown in Fig. 50. It suggests the recovery of vertical coherence for the short pulse in most cases.

An exhaustive treatment of the electron beam jitters and short pulse transport through the beamlines will be subject of a dedicated work.

13.4. Non-tilted bunches

Non-exact cancellation of the TDCs transverse kicks, intrinsically due to RF voltage and phase jitter on top of the non-zero distance between the two cavities, leads to growth of the turn-averaged transverse emittances of non-tilted bunches [75], see Fig. 51. The RMS vertical beam size at the IDs grows from ~2 μm for the beam with TDCs turned off, up to 5 μm. The horizontal size remains substantially unperturbed (not shown). These analytical results are in agreement with particle tracking and are consistent with preliminary specifications for the RF stability of the TDCs equal to relative peak voltage jitter <0.1 %, phase stability <0.04 deg S-band.

14. Injection chain

The full-energy injection chain of Elettra 2.0 shall guarantee injection efficiency in multi-bunch and fill-up mode larger than 95 %. This lower limit is basically set by radioprotection considerations, while a value approaching 98 % is targeted in user operation mode. Injection will happen at the repetition rate of 2 Hz, at the full energy of 2.4 GeV, with maximum average injected current of 2 mA in multi-bunch and fill-up mode, and 0.4 mA in top-up mode.

Tight constraints imposed by, e.g., the 5-fold smaller dynamic aperture of Elettra 2.0 compared to that of the present Elettra, impose a series of on-field measurements for the characterization of the extracted beam in the present system, and upgrade of existing hardware. In particular, the strategy is to replace some obsolete or underperforming parts of the linac, transfer lines and booster ring.

14.1. Injection into the main ring

The robustness of the present 4-kicker, off-axis injection scheme of Elettra, together with the relatively large dynamic aperture of Elettra 2.0 compared to other facilities in the same energy range, justifies the adoption of the same geometry for the new light source, at least in its first phase of commissioning and operation.

The injection into the storage ring will take place in a single straight section using a 4-kicker bump, in conjunction with a 3-septum system. The adoption of 4 identical kickers with same ceramic vacuum chamber ensures the same action on the stored beam and, at the same time, minimizes the risk of unbalanced kicks. The operating parameters of S1, S2 and K4 in off-axis injection mode are listed in Table 21.

The lattice of Elettra 2.0 and its dynamic aperture call for a horizontal separation of the stored and injected beam of 4 mm at the exit point of the septum system. A mere adjustment of strengths and position of the existing septa is not a satisfactory solution, since the magnets would be driven to stressing currents. A system of three septum magnets

Table 21
Operational parameters of septa and kicker magnets for Elettra 2.0 at 2.4 GeV.

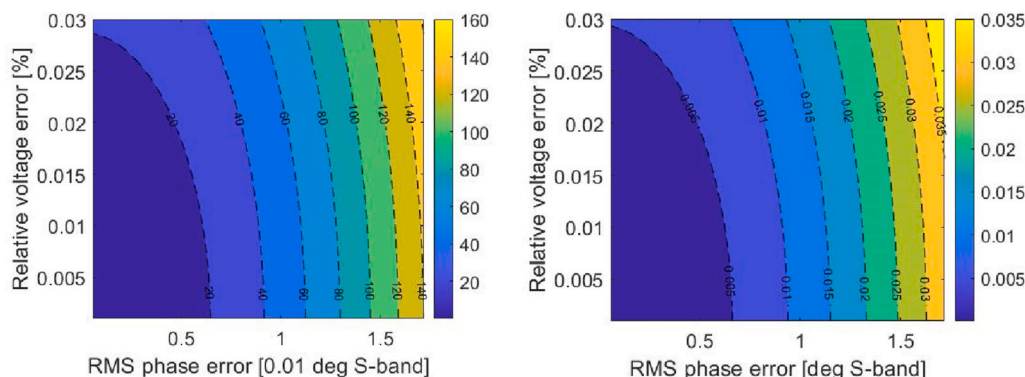|	S1, S2	S3	K1–K4	Unit
Core length	510	350	350	mm
Hor./vert. aperture	25 x 10	25 x 10	54 x 40	mm
Total deflection	8.03	0.57	0.5	deg
Peak magn. field	1.0	0.19	0.20	T
Peak current	8.74	1.5	6.24	kA
Total inductance	2.6	2.1	1.6	μH
Circuit capacitance	120	1.2	1.25	μF
Current pulse duration	57	5	5	μs
Charging voltage	1.29	2.0	7.1	kV
Pulse rep. rate	3.33	3.33		Hz
Total power losses	142			W

Fig. 51. Analytical estimate of the vertical geometric emittance growth in pm-rad as function of the TDCs RMS relative voltage in % and phase jitter in deg S-band.

was eventually devised: two thick septa, named S1 and S2, will deflect the incoming beam by about 8 deg; one thin septum, named S3, will deflect the beam of the remaining 0.6 deg. The offset of the beam at the S3 exit point is 10 mm. Hence, a kicker bump of 6 mm and a copper shield thickness of 1 mm in S3 will ensure the specified separation. The magnetic core of the septa will be made of silicon-iron laminations with a thickness of 0.1 mm. The surrounding box will be made of copper; the copper conductor will be isolated from the magnet core by means of suitable spacers made of alumina (Al_2O_3), a ceramic material which exhibits very good dielectric properties as well as good mechanical properties in terms of hardness.

A suitable vessel, shown in Fig. 52, will be designed to house the magnets. The chamber will be a large cylinder with an inner diameter of 400 mm and a length of 1730 mm overall. Lateral flanges will allow the assembly of the magnets, access to the adjusting tools of the internal plate, to power connections and cooling system. Suitable vacuum pumps will assure ultra-high vacuum conditions.

The kicker magnets will be conventional window-frame magnets with a transverse free aperture of 54 mm × 40 mm. The magnetic cores will be fabricated with either Permalloy-C or silicon-iron laminations, with a thickness of 0.1 mm; the laminations will be glued and surrounded by a stainless-steel box. The insulation between the conductor and the magnetic core will be done through a suitable thickness of fiberglass impregnated with Araldite resin.

A magnetic pulse duration of 5 µs requires a ceramic chamber installed in the gap of the kickers, to avoid field attenuation. The cross section of the vacuum chamber is elliptical, with internal dimensions of 32 mm × 24 mm. The internal surface will be coated with a 3 µm layer of titanium deposited by a sputtering process. Suitable flanges with bellows will be brazed at both ends, allowing the mechanical connection with the storage ring chamber. The electrical continuity between the storage ring chamber and the titanium layer will be assured by suitable RF fingers installed in the interface flanges.

The proposed layout for the Elettra 2.0 injection system will also allow on-axis injection but, of course, no accumulation. By adjusting the position of the S2 exit point and switching off S3, it will be possible to send the incoming beam directly to the centre of K4; this will then deflect the beam onto the storage ring axis. The on-axis injection is
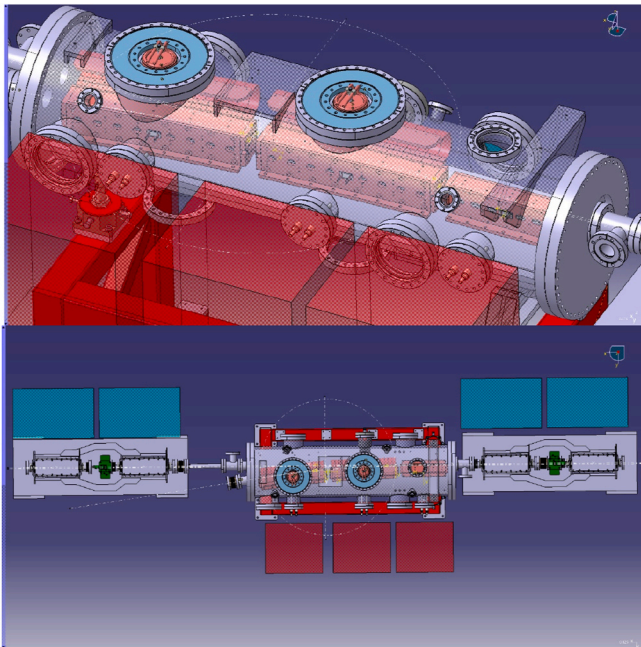
intended for diagnostic purposes and optics studies during the very first turn.

14.2. Booster upgrade: alignment, diagnostics and power supplies

The booster for Elettra has been in operation for the last 15 years, bringing the electron beam energy from 100 MeV to 2 and 2.4 GeV. The energy of the extracted beam is selected by changing the extraction time along the energy ramp of the magnets [2]. The nominal optics provides a natural horizontal emittance of the extracted beam of 226 nm rad at 2.4 GeV. The maximum average current to be stored in the booster is approximately 3 mA.

In 2022, a realignment of the booster dipole and quadrupole magnets was carried out. Eventually, the magnets were moved ±200 µm in their lateral positions with respect to the reference orbit. This adjustment allowed storing the beam without corrector magnets along an orbit with absolute RMS deviation <3 mm vertically and <4 mm horizontally.

The old VME-based BPM system, dating back to Elettra, has been refurbished with new Libea Spark BPMs. The system provides up to 32 orbits during the energy ramp, one every 5 ms. A dedicated high-level software has been developed for orbit correction during the ramp. The BPM resolution at 1 mA stored average current is ±100 µm. By 2025, the electronics of the booster BPMs will be replaced with the same BPM system of Elettra 2.0. This system will provide a resolution as low as 5–10 µm, more efficient noise rejection, and single-turn measurements.

A digitizer card was recently adopted for measuring the beam current accumulated during the energy ramp with a time resolution of 200 µs. This card will allow the detection of any small current leakage during the ramp, and thus will improve the injection efficiency during top-up.

Tune measurement is done using in-house developed, custom electronics, based on a PC-104 interfaced to an electronic board that includes an FPGA, memories, 4 input 14-bit ADC channels, and 2 output 12-bit DAC channels, see Fig. 53. An RF divider allows data sampling every synchronous turn (Booster Ring Clock). Two input ADC channels are used to sample the x- and y-position signal from the Bergoz BPM analogic front end. A tune excitation pattern can be generated through one output channel linked to a 600W-amplifier, connected in turn to an excitation plane selector of a stripline kicker. The other output channel is used to modulate the output power according to the energy of the beam during the ramp. The tune measurement system allows a maximum frequency resolution of 1 kHz with a sampling rate of 2 ms.

The tune measurement system communicates with the Tango control system via a TCP socket. The Tango device server provides the excitation (gain and excitation pattern) and readout channels for the measurement, as well as the commands for selecting the measurement plane. A Python3-based graphical interface is used to control the instrument in
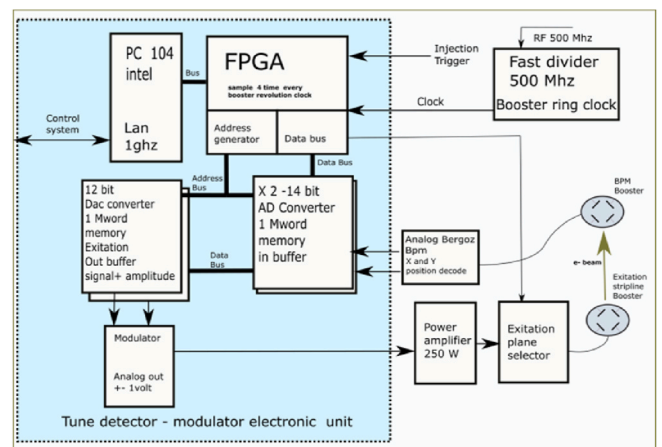

Fig. 52. Top, 3-D rendering of the septum system vessel. Bottom, view of the 4-kicker and 3rd septa injection system.

Fig. 53. Block schematic of the Booster tune measurement system.
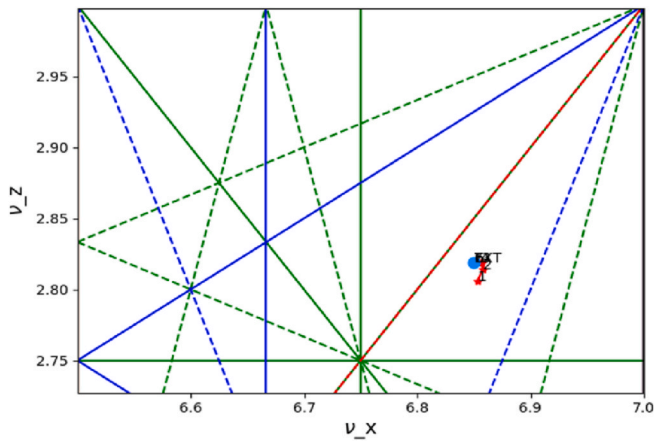
Fig. 54. Betatron tunes measured in the Booster ring during energy ramp.

the control room and to analyze the recorded data. In particular, the reading of the fast oscillation data is processed with SciPy's spectrogram functions, which eventually allows plotting the variation of betatron tunes during the energy ramp in the booster, as shown in Fig. 54. These data can be used by the other tools recently developed for fine-tuning the current ramps of the power supplies, and to correct the tunes during the energy ramp.

Recently, a non-repeatability of the output current of the power supplies between consecutive ramp cycles was detected, up to 300 mA peak-to-peak for the dipoles and up to 200 mA for the quadrupoles. This variability leads to tune variations shot-to-shot, corresponding to 40 kHz in the horizontal plane and to 10 kHz in the vertical, as shown in Fig. 55. For this reason, the present power supplies will be replaced with new ones, which shall guarantee a maximum shot-to-shot variation of the supplying current < 50 mA.

14.3. Booster upgrade: emittance reduction

The booster ring magnetic lattice is composed of one family of 28 dipoles, one family of 18 focusing quadrupoles, and one family of 18 defocusing quadrupoles. The dipoles' magnetic field is 1 T at the maximum energy 2.5 GeV, corresponding to a bending radius of 8.289 m. The circumference of 118.8 m provides 8 long straight sections of about 3 m each. The booster harmonic number is 198, i.e., the ratio 11/24 of the main ring RF frequency of 499.654 MHz.

Until now, the booster has been ramping the magnet currents (from 30 A to 700 A for the dipoles, from 10 A to 300 A for the quadrupoles) up

to an equivalent beam energy of 2.5 GeV. The energy of the extracted beam, either 2.0 or 2.4 GeV, is selected by choosing in time the instant of extraction.

The design horizontal emittance of the booster is 160 nm rad at 2 GeV and 226 nm rad at 2.4 GeV. Simulations of beam injection into Elettra 2.0 showed that a horizontal emittance of 160 nm rad at 2.4 GeV is small enough to reach an injection efficiency of 95 %. To reduce the booster equilibrium emittance at 2.4 GeV, different strategies have been considered, some already in use.

- improve the alignment of magnets
- correct the orbit during energy ramping
- optimize the tune working point
- correct the tunes during energy ramping
- allow off-energy accumulation
- allow emittance swap

From a tune scan performed with AT [46,76], a new working point was found, which allows the reduction of the equilibrium horizontal emittance to 160 nm rad at 2.4 GeV, and at the same time guarantees the required dynamic aperture for injection into the booster ring [77].

Thus, the working point was changed from the present $(\nu_x, \nu_y) = (5.39, 3.42)$ to $(6.80, 2.85)$. The new point increases the average horizontal dispersion in the long straight section of the injection and extraction lines (see Fig. 56), in contrast to the previous setting with zero dispersion. As a consequence of the new optics, a different (dispersive) orbit along the booster-to-ring transfer line implies a higher voltage of the extraction kicker for injection into Elettra 2.0, close to the upper limit of the present hardware.

To minimize the risks of faults of the kicker by keeping the voltage sufficiently low, 4 existing dipole magnets, denominated "bumpers", have been put in operation. The bumpers can be supplied with a maximum current of 12 A 5 ms immediately before the extraction time. Doing so, they horizontally shift the orbit by 5 mm, with consequent injection into Elettra 2.0 without an additional stress of the kicker. A schematic of the kicker and bumper system is shown in Fig. 57. In addition to the low emittance booster optics, off-energy operation is expected to produce further reduction of the horizontal emittance, down to 130 nm rad at 2.4 GeV.

Simulation results, shown in Fig. 58, indicate that the injection efficiency into Elettra 2.0 can largely gain from a reduction of the booster horizontal emittance below 100 nm rad, though at the expense of a larger vertical emittance. The emittance swap, carried out, for example, through crossing of the difference linear resonance, would then allow the horizontal emittance to reach 30 nm rad, for which an injection efficiency higher than 95 % is expected.
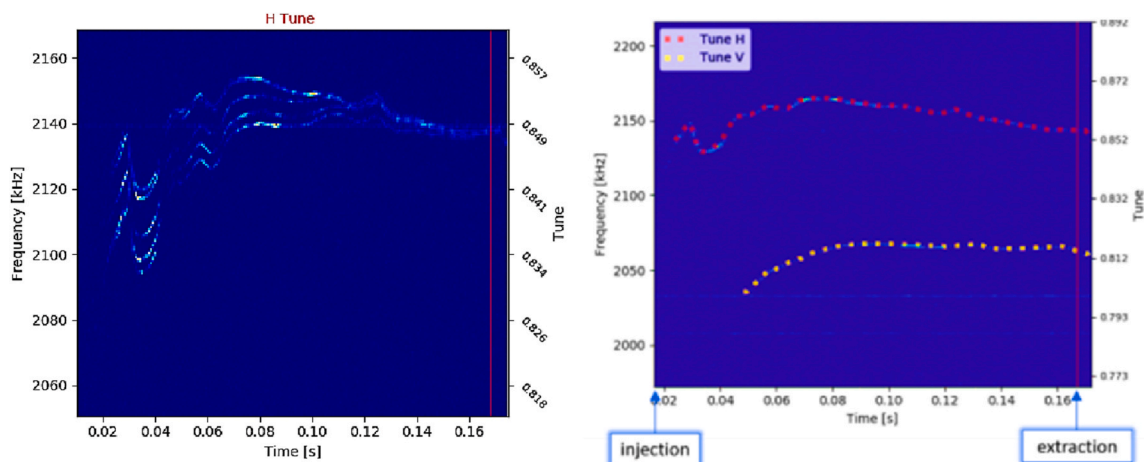

Fig. 55. Consecutive measurement of horizontal (left) and vertical tune (right) in the Booster ring during energy ramping.
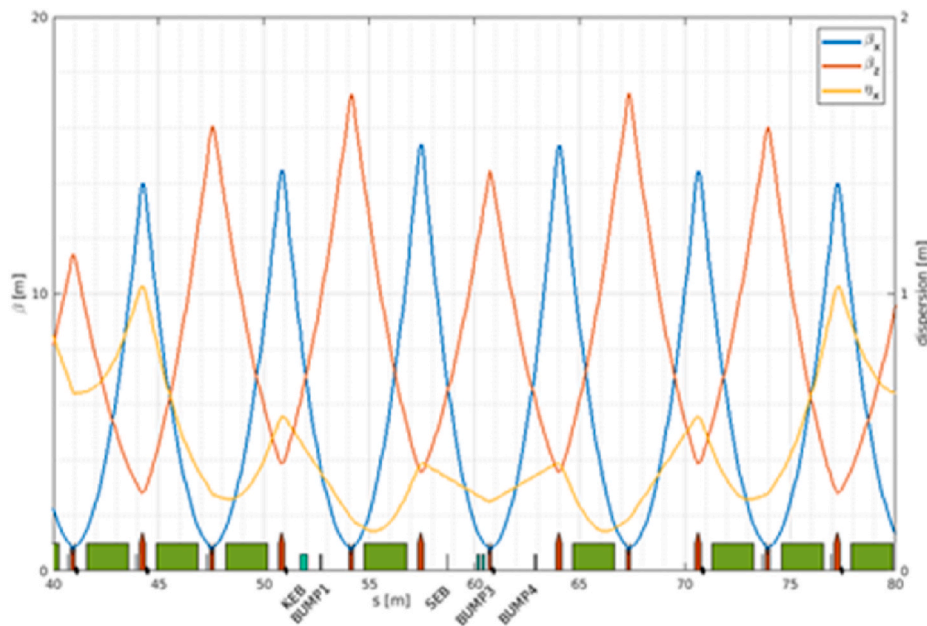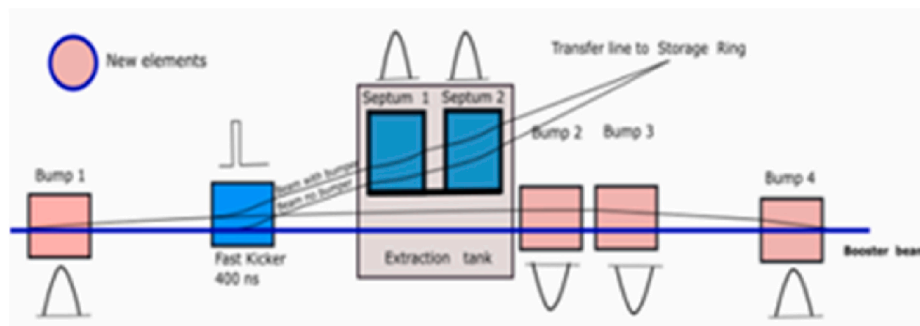
Fig. 56. Booster low emittance optics.
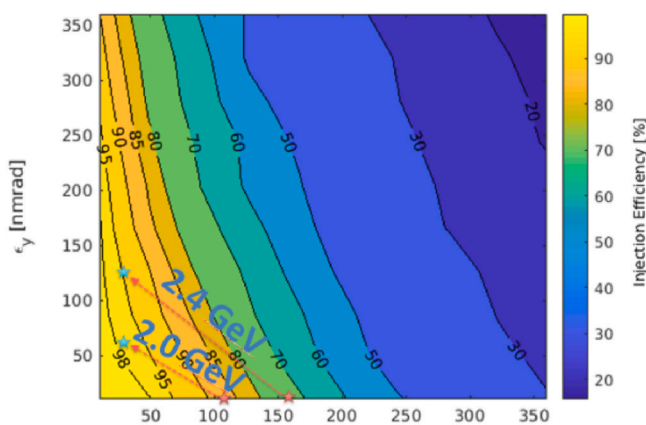

Fig. 57. Bumper system of the Booster ring.

Fig. 58. AT simulation of injection efficiency into Elettra 2.0 as function of horizontal and vertical emittance of the injected beam.
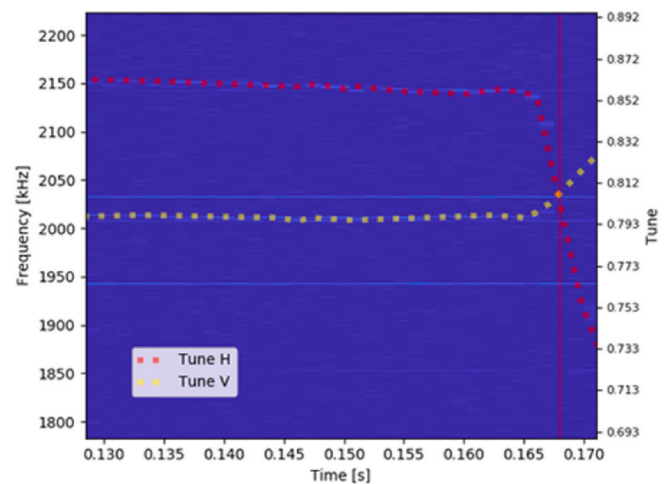

Fig. 59. Horizontal (dotted yellow) and vertical (dotted red) betatron tune during emittance swap. The swap happens in approximately 3 ms or 7600 turns in the Booster. Beam extraction is at time coordinate 168 ms.

The measurement of tunes during the emittance swap is shown in Fig. 59. The beam extraction time is determined by a temporal shift of the extraction kicker signal. Fig. 60 shows the measured beam transverse profile at the extraction point, before and after emittance swap. The emittances were evaluated with two independent methods. First, linear optics functions, including dispersion, were evaluated on the basis
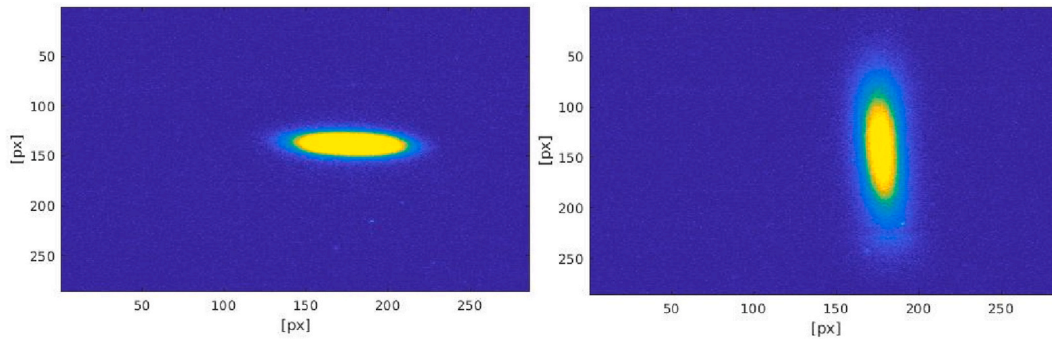
Fig. 60. Beam profile 3 ms before extraction (left), and at extraction time (right).

of the transfer line model, and assuming an RMS energy spread of 0.07 %. The geometric emittance was then retrieved from the beam sizes and found to be 105 nm rad 3 ms before extraction and 30 nm rad at extraction time. Second, the emittance was measured through a quadrupole scan at the end of the booster-to-ring transfer line, confirming the aforementioned reduction.

14.4. Linac upgrade

The electronics controlling the RF Gun modulator will be replaced by new and better performing ones, mainly to improve beam stability at the 100 MeV extraction energy. The thermionic gun will also see an increase of the high voltage from 57 kV to 90 kV and a replacement of the obsolete TH306 oxide electron source with a new CPI Y-646 oxide. Doing so, the gun will be able to operate in three different modes: single bunch, multi-bunch, and crab cavity mode, as sketched in Fig. 61.

The linac modulators will require the fabrication and installation of two positive-polarity, high-voltage power supplies. This choice will allow the switch from a high repetition rate (10 Hz) mode but at a voltage half that of the nominal value, to a low repetition rate (3 Hz) at nominal voltage. The former mode will be used for RF conditioning and, whenever needed, to control of the charge voltage of the Pulse Forming Network (PFN). This scheme will result in turn in a higher shot-to-shot stability of the accelerating RF pulse. The latter mode will guarantee maximum extraction energy.

15. Removal and installations

The Elettra 2.0 project is structured into five work-breakdown areas: accelerator, photon beamlines, infrastructures, executive management, and removal and installations. The latter is a relevant area because the new machine and new or modified beamlines will replace the old ones. Although logistics is not "rocket science" [78,79], a poor coordination and planning of procurement, transportation, and storage can cause congestion in the supply and movement of components and systems, increasing the risk of delays and damage of equipment and infrastructure. Upgrading an existing machine doubles the difficulties, handling both old parts and the new ones, almost at the same time. Different approaches also must be adopted for what is contained in the Storage Ring (SR) tunnel – subject to radio protection verification – and what is external to the tunnel and can be handled and, in case, discharged more easily. Additionally, parts to re-use and those that must be temporary removed, protected and stored, require different procedures from the parts to be discarded and disposed.

15.1. Storage ring, service area and beamlines

Due to radioprotection rules – according to national authorities – a "red zone" centred on the beam trajectory is mandatory subject to the extensive characterization of existing radionuclides before materials may exit the facility premises, in particular for discarding or disposal. Adequate space for temporary storage – the time scale is months or years
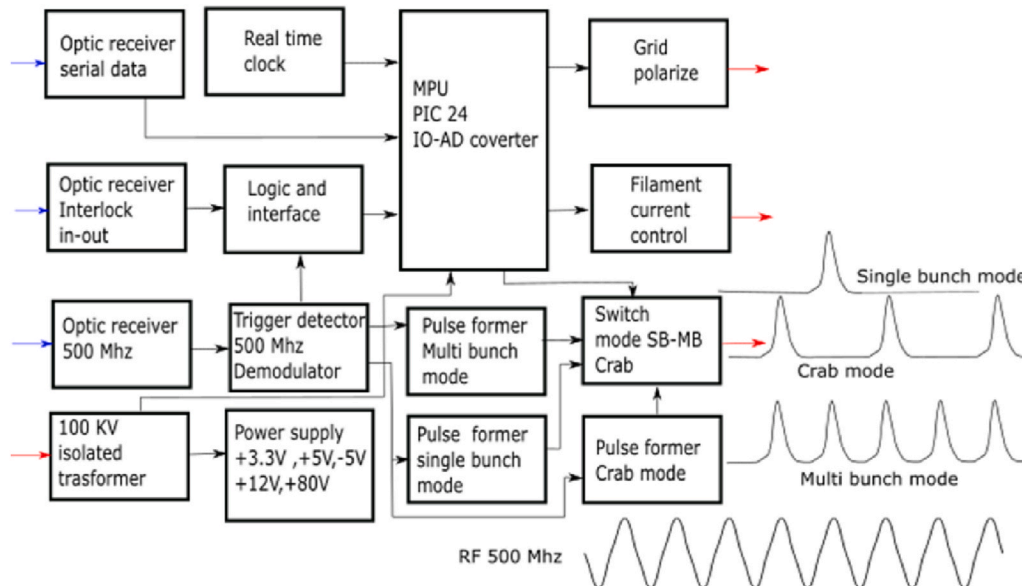

Fig. 61. Schematic of the 90 kV electronic board of the Gun modulator, and modes of operation for Elettra 2.0.
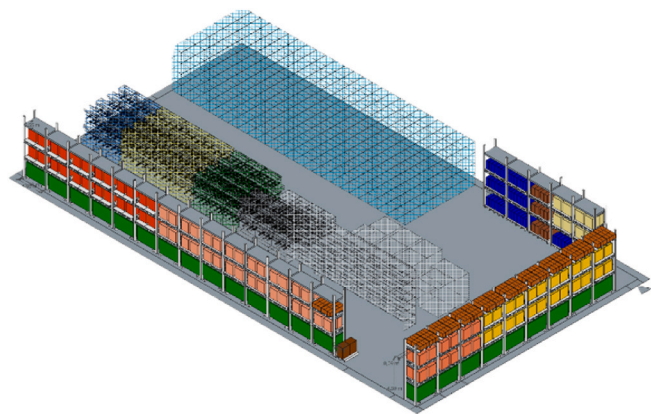
Fig. 62. Proposed arrangement of SR components and parts in-side the RP building.

– must be found and provided on-site prior to the "Dark Period" when Elettra will be turned off for the last time. A new 700 m^2, 4.5-m high building (Fig. 62), equipped with heavy-duty shelves, will be built within the facility premises for this purpose. Magnets will be placed on standard pallets and stored on the shelves, while the space in the middle is reserved for the girders and boxes with the cabling and piping cut into small pieces for ease of handling.

Fig. 63-left shows the storage ring: all that is present – including the concrete girders and the cooling water piping on the wall – have been taken into consideration. The Service Area (SA) contains the magnet power supply cabinets (they are show in Fig. 64-right, the colour is keyed to the magnet that they energize) and more instrumentation – vacuum, beam diagnostics, etc. – in standard 19" racks. All power supply cabinets and the majority of racks will be removed and replaced. Most of the cables that run under the false floor from the cabinets and racks to the storage ring will be removed and disposed of as well.

Elettra operates 28 beamlines. In order to have a real overview of the actual installations, in January 2022 we made a "crane-photogram-metry" of the Experimental Hall (EH) mounting a camera on one of the two bridge cranes. The resulting Hi-Res mosaic is particularly valuable for the identification of potential storage areas and the actual shape/size of hutches and other installations, including the not-updated changes to the original drawings.

Fig. 64 shows one quadrant of the EH, reporting the number of the building pillars and the names of the beamlines. Some beamlines will remain in the current position, other will be moved, other will be updated and some new ones will be added. A total of 32 beamlines is foreseen at the end of the three upgrade phases. The first phase is currently running and comprises all predispositions and installations that do not impact the normal operation of the beamlines before the start of the "Dark Period". The second and third phases will occur during and,
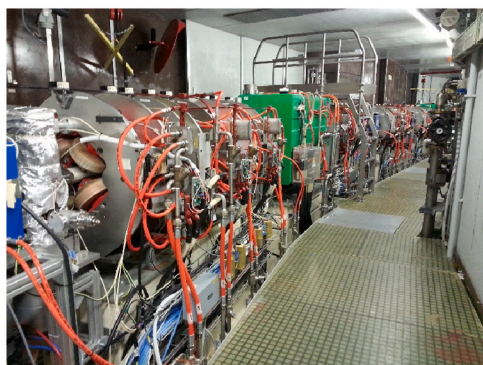
respectively, after the Dark Period, involving the beamlines to re-allocate or install.

15.2. Shielding wall

As mentioned in the previous paragraph, the Elettra 2.0 project comprises new beamlines and the re-allocation of some of the currently operational ones. Consequently, the Experimental Hall (EH) of Elettra, i. e. where the beamlines are installed, is another working area with activities that have started well before the scheduled Dark Period. The installation of the beamlines implies, among many more activities, the partial reconfiguration of the shielding wall of the storage ring tunnel.

The Elettra tunnel is composed of an inner permanent wall that is 0.5 m thick while the outer shielding is completely formed by columns of normal or baritic concrete blocks. This arrangement allows flexibility in the configuration of the shielding, according to the front-end/beamline design. About 400 concrete tiles covering the SR tunnel in a double layer and weighting up to 6 tons constitute the roof.

To extract the SR magnets and other equipment and to install the new machine, as well as reconfigure the outer shielding wall for the new beamlines, we will remove all roof tiles and define a temporary 1300 m^2 depot – organized in three areas – to store them during the Dark Period.

Even limited interventions on the outer shielding wall require the movement of several tiles. In October 2022 we operated a significant preparatory intervention on the shielding blocks in Section 12.1 to
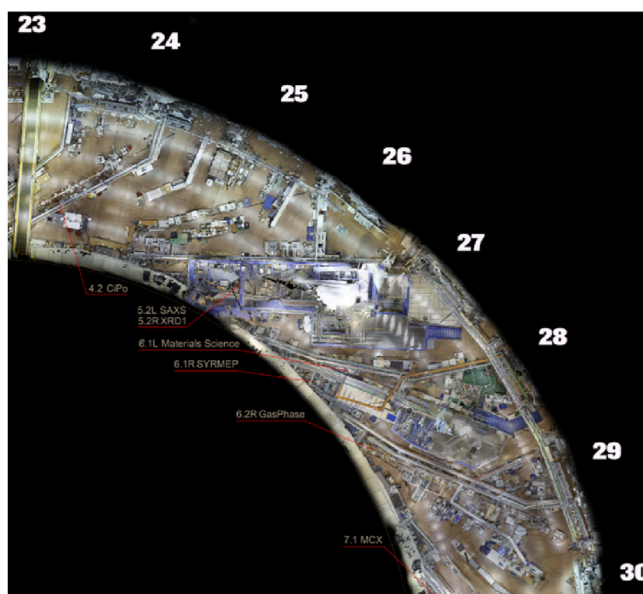

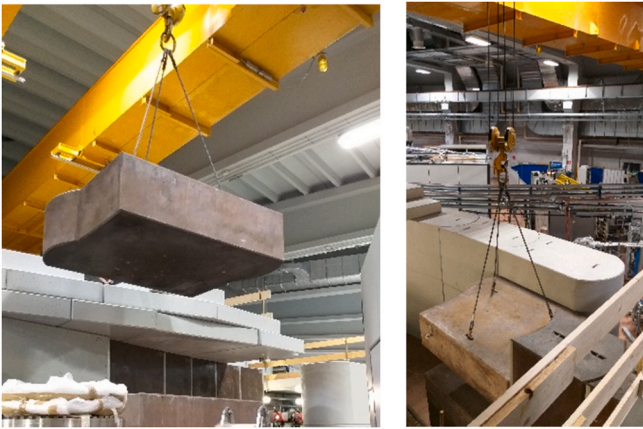**Fig. 64.** One quadrant of the Elettra Experimental Hall.

Fig. 63. Photo of the Elettra Storage Ring (left) and Service Area.

Fig. 65. Lifting and placing of a "beam-exit" block.
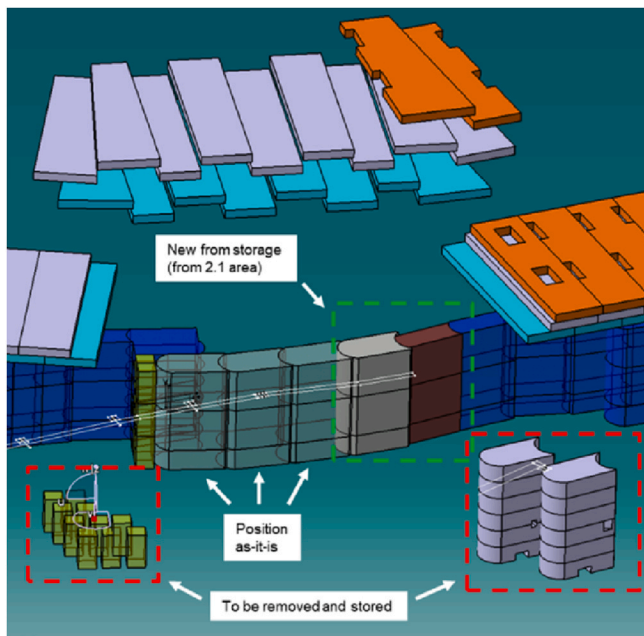

Fig. 66. Preliminary activity for the installation of the new beam-exit 12.1.

allow, from the radioprotection point of view, the demolition of a no longer used hutch. Fig. 65 shows the lifting and placing of blocks in correspondence of the beamline exit port. Fig. 66 summarizes the intervention: two columns with slots for the passage of the previously dismantled back-end vacuum vessel must be replaced by two columns without slots.

Fig. 67 shows section 12.1 with the installation of the "beam-exit": the current configuration is shown in blue (while the new one is in red) comprising the insertion of the "beam-exit blocks" (indicated by the red arrow) and the old hutch to demolish (blue arrows).

Two more reconfigurations of the shielding wall are in course. Fig. 68 shows the required changes in the configuration of the wall to prepare for the future beam-exits in section 3.1 and 4.1. In blue, the current configuration is shown, while in red the new one comprises the insertion of the "beam-exit blocks" (indicated by the red arrow).

15.3. Logistics

The objects identified to remove/re-allocate/install require adequate lifting and moving devices and routes. Two 7.5-ton bridge cranes cover the entire EH and SR, but only partially cover the SA. All the objects

Fig. 67. Outer wall reconfiguration for beam-exit 12.1.

from/to the storage ring or the beamlines will exit/enter the Elettra building though two truck gates (named "D" and "E" in Fig. 69).

The equipment in the service area (mostly items to discard) will exit the building using a sort of "backdoor". We will reinforce the false floor in the inner side of the SA to bring the loads under the crane mounted on the roof of the Elettra building (yellow oval in Fig. 69), and lift them from the courtyard inside the building itself.

Either using the bridge cranes of the EH or the crane on the roof, the removed material, as well as the equipment to install, can reach the Elettra building following a single two-way path (indicated by the orange dashed arrow) close to the FERMI Klystron Gallery.

The portals "B" and "ES3" are pedestrian entrances that allow only hand-moved loads on manual forklifts; entrances "D" and "E" are large and high enough for trucks and large carts.

16. Conclusions

The Elettra 2.0 project is financed by the Italian government. The very first implementation phase is presently ongoing, in parallel with the operation of Elettra. The specificity of the implementation in the present infrastructure and the ambition to satisfy a wide variety of innovative scientific cases, led to several original ideas, such as magnets with no protruding coils, multipole super-bends, programmable coils for multipole normal and skew field components, standardization of power converters, and capability of transverse coherence simultaneous to picosecond long pulses. Neither physical show-stoppers nor technical problems have emerged on the main path of the project. The feasibility of such versatile light source is therefore confirmed.

Data availability

No data was used for the research described in the article.

CRediT authorship contribution statement

E. Karantzoulis: Conceptualization, Investigation, Methodology, Project administration, Supervision. **S. Di Mitri:** Formal analysis, Investigation, Validation, Writing – original draft, Writing – review & editing. **F. Barbo:** Investigation. **W. Barletta:** Conceptualization, Writing – original draft, Writing – review & editing. **S. Bassanese:** Investigation. **R. Bracco:** Investigation. **G. Brajnik:** Investigation. **A. Buonanno:** Conceptualization, Investigation, Resources, Visualization. **D. Caiazza:** Data curation, Investigation, Methodology, Software. **A. Carniel:** Conceptualization, Investigation, Resources, Software. **D.**
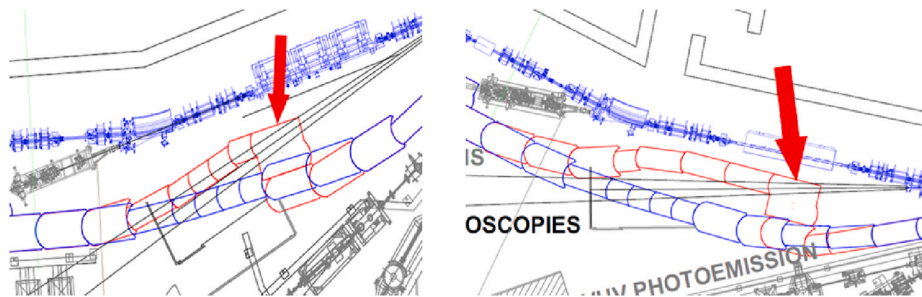
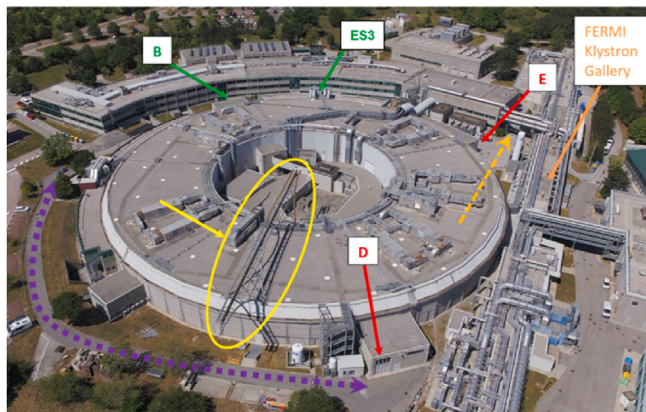**Fig. 68.** Outer wall reconfiguration for beam-exit 3.1 (left) and 4.1.

Fig. 69. View of the Elettra Building, roof crane, entrances and constraints to transportation.

Castronovo: Conceptualization, Investigation, Methodology, Project administration, Resources, Validation, Visualization. **M. Cautero:** Investigation, Methodology, Project administration, Resources, Validation. **S. Cleva:** Formal analysis, Investigation, Methodology, Software, Visualization. **M. Comisso:** Investigation. **I. Cudin:** Conceptualization, Investigation, Methodology, Project administration, Software, Supervision, Visualization. **S. Dastan:** Investigation. **R. De Monte:** Investigation. **B. Diviacco:** Conceptualization, Investigation, Methodology, Project administration, Resources. **A. Fabris:** Conceptualization, Funding acquisition, Methodology, Project administration, Resources, Supervision. **R. Fabris:** Conceptualization, Formal analysis, Investigation, Visualization. **G. Gaio:** Investigation, Resources, Software. **S. Grulja:** Investigation. **L. Gregoratti:** Conceptualization, Investigation, Project administration, Supervision. **A. Gubertini:** Investigation. **S. Krecic:** Conceptualization, Data curation, Investigation, Software, Validation. **S. Lizzit:** Investigation, Project administration, Resources, Supervision. **G. Loda:** Methodology, Visualization. **M. Lonza:** Conceptualization, Formal analysis, Investigation, Software. **K. Manukyan:** Conceptualization, Data curation, Investigation, Methodology, Software, Validation. **B. Mazzucco:** Methodology, Resources. **M. Milani:** Methodology, Visualization. **D. Millo:** Investigation. **M. Modica:** Conceptualization, Investigation. **L. Novinec:** Investigation, Visualization. **G. Pangon:** Software, Visualization. **C. Pasotti:** Investigation, Methodology, Project administration, Supervision. **A. Passarelli:** Formal analysis, Investigation, Visualization. **L. Rumiz:** Investigation, Methodology, Project administration, Supervision. **S. Sbarra:** Methodology. **G. Scrimali:** Methodology, Software, Visualization. **N. Shafqat:** Conceptualization, Formal analysis, Investigation. **G. Simonetti:** Methodology, Resources, Software, Visualization. **M. Svandrlik:** Funding acquisition, Project administration, Supervision. **F. Tripaldi:** Investigation, Resources, Software. **M. Veronese:** Conceptualization, Investigation. **R. Visintini:** Methodology, Project administration, Supervision, Visualization. **E. Yousefi:** Investigation. **M. Zaccaria:** Resources.

Declaration of competing interest

The authors declare that they have no known competing financial interests or personal relationships that could have appeared to influence the work reported in this paper.

Data availability

Data will be made available on request.

Acknowledgements

References

[1] E. Karantzoulis, et al., Top-up implementation and operation at Elettra, in: Proc. IPAC'10, paper WEPEA028, Kyoto, Japan, May 2010, pp. 2543–2545.

[2] E. Karantzoulis, A. Carniel, S. Krecic, Top-up operational experience at Elettra, in: Proc. IPAC'11, paper THPC027, San Sebastian, Spain, Sep. 2011, pp. 2966–2968.

[3] E. Karantzoulis, et al., Elettra 2.0 Conceptual Design Report, ST/M-17/01, Elettra – Sincrotrone Trieste, internal document, 2017.

[4] E. Karantzoulis, Elettra 2.0 - the diffraction limited successor of Elettra, Nucl. Instrum. Methods Phys. Res. A 880 (2018) 158–165, https://doi.org/10.1016/j.nima.2017.09.057.

[5] E. Karantzoulis, W. Barletta, Aspects of Elettra 2.0 design, Nucl. Instrum. Methods Phys. Res. A 927 (2019) 70–80, https://doi.org/10.1016/j.nima.2019.01.044.

[6] E. Karantzoulis, et al., Elettra 2.0 Technical Design Report, ST/M-21/01, Elettra – Sincrotrone Trieste, internal document, 2021.

[7] G. Penco, M. Svandrlik, Experimental studies on transient beam loading effects in the presence of a superconducting third harmonic cavity, Phys. Rev. ST Accel. Beams 9 (2006), 044401.

[8] S. Hadrich, J. Rothhardt, M. Krebs, S. Demmler, A. Klenke, A. Tunnermann, J. J. Limpert, Journ. Phys. B Atom. Mol. Opt.Phys. 49 (2016), 172002.

[9] R. Costantini, et al., J. Electron. Spectrosc. Relat. Phenom. 254 (2022).

[10] M. Borland, Synchrotron Radiat. News 27 (6) (2014) 2–3.

[11] R. Hettel, Proc. Of the 5th Intern. Part. Accel. Conf., MOXBA01, June 2014, p. 7. Dresden, Germany.

[12] A. Streun, et al., SLS-2 – the upgrade of the Swiss light source, J. Synchrotron Radiat. 25 (2018) 631–641.

[13] R.W. Schoenlein, S. Chattopadhyay, H.H. Chong, T.E. Glover, P.A. Heimann, C. V. Shank, A.A. Zholents, M.S. Zolotorev, Science 287 (2000) 2237–2240.

[14] S. Di Mitri, et al., Laser-slicing at a low-emittance storage ring, J. Synchrotron Radiat. 26 (2019) 1523–1538.

[15] A. Zholents, A new possibility for production of sub-picosecond x-ray pulses using a time dependent radio frequency orbit deflection, Nucl. Instrum. Methods Phys. Res. 798 (2015) 111–116.

[16] D. Castronovo, et al., The new Elettra 2.0 magnets, in: Proc. of the 14th Int. Particle Accelerator Conf. (IPAC'23), MOPA140, Venice, Italy, May 2023.

[17] D. Caiazza, et al., Magnetic measurement systems for Elettra 2.0, in: Proc. of the 14th Int. Particle Accelerator Conf. (IPAC'23), WEPM034, Venice, Italy, May 2023.

[18] G. Simonetti, et al., Elettra 2.0 girder support design, in: Proc. of the 14th Int. Particle Accelerator Conf. (IPAC'23), MOPM052, Venice, Italy, May 2023.

[19] L. Novinec, et al., Elettra 2.0: the vacuum system design for a new generation storage ring, in: Proc. of the 14th Int. Particle Accelerator Conf. (IPAC'23), THPA136, Venice, Italy, May 2023.

[20] C. Pasotti, et al., RF system design for Elettra 2.0, in: Proc. IPAC'22, June 2022, pp. 1570–1572, https://doi.org/10.18429/JACoW-IPAC2022-TUPOMS061. Bangkok, Thailand.

[21] K. Manukyan, et al., The effect of insertion devices on beam dynamics for Elettra 2.0, in: Proc. of the 14th Int. Particle Accelerator Conf. (IPAC'23), WEPL094, Venice, Italy, May 2023.

[22] A. Gamelin, et al., mbtrack2, a collective effect library in Python, in: Proc. IPAC'21, May 2021, pp. 282–285, https://doi.org/10.18429/JACoW-IPAC2021-MOPAB070. Campinas, Brazil.

[23] S. Dastan, et al., Broad Band Impedance Effects on Elettra 2.0, presented at the 14th Int. Particle Accelerator Conf. (IPAC'23), Venice, Italy, May 2023 paper MOPM051, this conference.

[24] S. Dastan et al., "Study on transverse multi-bunch instability in Elettra 2.0", in Proc. of the 14th Int. Particle Accelerator Conf. (IPAC'23), MOPM050, Venice, Italy. .

[25] [Borland2000] M. Borland, Elegant: a flexible SDDS-compliant code for accelerator simulation, Adv. Photon Sour. LS 287 (2000).

[26] M. Lonza, et al., Transient beam loading studies in view of the Elettra 2.0 upgrade project, in: Proc. of the 14th Int. Particle Accelerator Conf. (IPAC'23), WEPA009, Venice, Italy, May 2023.

[27] A. Carniel, et al., Operation improvements of the actual booster for Elettra 2.0, in: Proc. of the 14th Int. Particle Accelerator Conf. (IPAC'23), THPL076, Venice, Italy, May 2023.

[28] S. Krecic, et al., Emittance reduction of the actual booster for Elettra 2.0, in: Proc. of the 14th Int. Particle Accelerator Conf. (IPAC'23), WEPL022, Venice, Italy, May 2023.

[29] B. Diviacco, Insertion device developments for Elettra 2.0, in: Proc. of the 14th Int. Particle Accelerator Conf. (IPAC'23), MOPM097, Venice, Italy, May 2023.

[30] D. Castronovo, et al., Superbend magnet for Elettra 2.0, in: Proc. of the 14th Int. Particle Accelerator Conf. (IPAC'23), MOPM056, Venice, Italy, May 2023.

[31] C.E. Taylor, S. Caspi, A 6.3 T bend magnet for the advanced light source, IEEE Trans. Magn. 32 (No. 4) (1996) 2175–2178.

[32] J. Zbasnik, et al., ALS superbend magnet system, IEEE Trans. Appl. Supercond. 11 (No. 1) (March, 2001) 2531–2534.

[33] R. Conte, "Éléments de Cryogénie", published by Masson & Cie, 1970.

[34] M. Cautero, et al., Elettra 2.0: magnet power converters strategy, in: Proc. of the 14th Int. Particle Accelerator Conf. (IPAC'23), WEPM076, Venice, Italy, May 2023.

[35] R. Visintini, M. Cautero, A 20-Ampere, 4-quadrant power supply for magnets, in: 2nd IEEE Southern Power Electronics Conference (SPEC'16), paper 115, Auckland, NZ, December 2016, https://doi.org/10.1109/SPEC.2016.7846023.

[36] R. Visintini, M. Cautero, G. Göransson, C.A. Martins, P.J. Torri, Power converters for the ESS warm magnets, in: Proc. of IPAC'17, May 2017, pp. 3372–3374, https://doi.org/10.18429/JACoW-IPAC2017-WEPVA051. Copenhagen, Denmark.

[37] S.K. Sharma, et al., Optimization of magnet stability and alignment for NSLS-II, in: Proc. PAC'11, paper THOBS2, New York, NY, USA, Mar.-Apr. 2011, pp. 2082–2086.

[38] S. Zelenika, et al., The SLS storage ring support and alignment systems, Nucl. Instrum. Methods Phys. Res. 467–468 (2001), https://doi.org/10.1016/s0168-9002(01)00246-7.

[39] Philippe Marion, Loys Goirand, Jean-Claude Biasci, "The ESRF new storage ring project main features and mechani-cal design aspects", in: Proc. MEDSI2014, Oct. 2014. Melbourne, Australia.

[40] L. Zhang, Beam stability consideration for low emittance storage ring, in: Proc. Workshop on Ambient Ground Motion and Vibration Suppression for Low Emittance Storage Rings 2017, Dec. 2017, pp. 11–13. Beijing, China.

[41] F. Cianciosi, et al., The girders system for the new ESRF storage ring, in: Proc. MEDSI'16, Barcelona, Spain, Sep. 2016, pp. 147–151.

[42] H. Wang, et al., Overall design of magnet girder system for heps-tf, in: Proc. IPAC'16, May 2016, pp. 2383–2385. Busan, Korea.

[43] M. Calvi, et al., Transverse gradient in Apple-type undulators, J. Synchrotron Radiat. 24 (3) (May 2017) 600–608.

[44] R.P. Walker, Depth-of-field effects in wiggler radiation sources: geometrical versus wave optics, Phys. Rev. Accel. Beams 20 (2017), 020703.

[45] P. Ellaume, "A new approach to the electron beam dynamics in undulators and wigglers", in: Proc. EPAC'92, 1992, pp. 661–664. Berlin, Germany.

[46] A. Terebilo, "Accelerator Toolbox for MATLAB", No, SLAC-PUB-8732, Stanford Linear Accelerator Centre, Menlo Park, CA, USA, 2001.

[47] P. Ellaume, O. Chubar, J. Chavanne, "Computing 3D magnetic fields from insertion devices", in: Proc. PAC'97, 1997, 9P027. Vancouver, Canada.

[48] F. Thomas, et al., X-ray absorber design and calculations for the EBS storage ring, in: Proc. MEDSI2016, 2016. Barcelona, Spain.

[49] H. Braun, et al., "SLS 2.0 Storage Ring, Technical Design Report", Report N. 21-02, PSI, PSI Bericht, Switzerland, 2021.

[50] R. M. Seraphin et al., "Vacuum system design for the SIRIUS storage ring", in Proc. EPAC'15.

[51] E. Al-Dmour, et al., Diffraction-limited storage ring vacuum technology, J. Synchrotron Radiat. (2014).

[52] R. Kersevan, M. Ady, Recent developments of monte-carlo codes Molflow+ and Synrad+, Proc. IPAC (2019).

[53] K. Deb, A. Pratap, S. Agarwal, T. Meyarivan, A fast and elitist multiobjective genetic algorithm: NSGA-II, IEEE Trans. Evol. Comput. 6 (2) (2002) 182–197.

[54] K. Ho, S. Newman, S. Rahimifard, R. Allen, State of the art in wire electrical discharge maching (wedm), INtern. J. Mach. Tools Manufact. 44 (12) (2004) 1247–1259.

[[5][5]] ANSYS, Ansys academic research fluent r2020.1 – cfd software ansys. http://www.ansys.com/products/fluids/ansys-fluent.

[56] ANSYS, Ansys academic research mechanical r2020.1 – f ea software ansys. http://www.ansys.com/products/structures/ansys-mechanic.

[57] C. Pasotti, et al., RF system upgrade for Elettra 2.0, in: Proc. IPAC'19, May 2019, pp. 2849–2851, https://doi.org/10.18429/JACoW-IPAC2019-WEPRB022. Melbourne, Australia.

[58] J.M. Byrd, S. De Santis, J. Jacob, V. Serriere, Transient beam loading effects in harmonic rf systems for light sources, Phys. Rev. ST Accel. Beams 5 (2002), 092001, https://doi.org/10.1103/PhysRevSTAB.5.092001.

[59] S. De Santis, R. Bartolini, J.M. Byrd, "Transient Beam Loading in the DIAMOND Storage Ring", Proc. EPAC'06, Edinburgh, UK, Jun. 2006 paper THPCH066.

[60] P.F. Tavares, Å. Andersson, A. Hansson, J. Breunlin, Equilibrium bunch density distribution with passive harmonic cavities in a storage ring, Phys. Rev. ST Accel. Beams 17 (2014), 064401, https://doi.org/10.1103/PhysRevSTAB.17.064401.

[61] A. Gamelin, N. Yamamoto, Equilibrium bunch density distribution with multiple active and passive RF cavities, in: Proc. IPAC'21, May 2021, pp. 278–281, https://doi.org/10.18429/JACoW-IPAC2021-MOPAB069. Campinas, Brazil.

[62] M. Patrick, "Possible upgrading of the SLS RF system for improving the beam lifetime", in: Proc. PAC'99, paper MOP138, New York, NY, USA, Mar. 1999.

[64] E. Karantzoulis, "An Overview on Impedances and Impedance Measuring Methods for Accelerators", Sincrotrone, Trieste, Italy, Jan. 1991. Rep. ST-M-91-1.

[65] CST Home Page. www.cst.com.

[66] W. Zotter, S. Kheifets, "Impedances and Wakes in High-Energy Particle Accelerators", World Scientific, Feb. 1998 https://doi.org/10.1142/3068.

[67] A. Fabris, C. Pasotti, P. Pittana, M. Svandrlik, P. Craievich, Proc. Of the 6th European Part. Accel. Conf., Field measurement of the ELETTRA cavity high order modes, Stockholm, Sweden, 1998, 1802-1804.

[68] T. Kaltenbacher, C. Vollinger, Characterization of shielding for the CERN SPS vacuum flanges with respect to beam coupling impedance, in: Proc. of IPAC, WEPIK090, 2017, pp. 3143–3146.

[69] SLS 2.0 Storage Ring Technical Design Report, PSI, 2021.

[70] S. Cleva, et al., Beam coupling impedance contribution of flange aperture gaps: a numerical study for Elettra 2.0, in: Proc. of the 14th Int. Particle Accelerator Conf. (IPAC'23), WEPL146, Venice, Italy, May 2023.

[71] E. Keil, et al., Concerning Longitudinal Stability in the ISR, CERN, Geneva, Switzerland, Jul. 1969. Rep. CERN-ISR-TH-RF-69-48.

[72] https://gitlab.cern.ch/IRIS/IW2D.git.

[73] J.L. Laclare, Transverse instabilities, in: Proc. CAS'85 vol. 2, CERN, Geneva, 1987, p. 306.

[74] X. Huang, B. Hettel, T. Rabedeau, J. Safranek, J. Sebek, K. Tian, K.P. Wootton, A. A. Zholents, Beam dynamics issues for the two-frequency crab cavity short pulse scheme, Phys. Rev. Accel. Beams 22 (2019), 090703.

[75] X. Huang, Coupled beam motion in a storage ring with crab cavities, Phys. Rev. Accel. Beams 19 (2016), 024001.

[76] B. Nash, et al., New Functionality for Beam Dynamics in Accelerator Toolbox (AT), Proceedings of IPAC 2015, Richmond, VA, USA, 2015.

[77] S. Krecic, A. Carniel, F. Tripaldi, "Emittance Reduction of the Actual Booster for Elettra 2.0", Presented at the 14th Int. Particle Accelerator Conf. (IPAC'23), paper WEPL022, this conference, Venice, Italy, May 2023.

[78] R. Visintini, A. Buonanno, B. Mazzucco, M. Milani, "Logistics Strategies for Elettra 2.0", Presented at the 14th Int. Particle Accelerator Conf. (IPAC'23), paper WEPM121, Venice, Italy, May 2023.

[79] R. Visintini, F. Barbo, A. Buonanno, M. Milani, G. Simonetti, "Elettra 2.0: Activities in the Experimental Hall", Presented at the 14th Int. Particle Accelerator Conf. (IPAC'23), paper MOPA162, Venice, Italy, May 2023.